Fabrication and characterisation of low-noise monolithic mode-locked lasers

Ph.D Thesis

David Larsson
COM•DTU
Technical University of Denmark

Supervisors:
Professor Jørn M. Hvam
Associate Professor Kresten Yvind

November 2006

Acknowledgements

Firstly I would like to thank my supervisors Professor Jørn Hvam and Associate Professor Kresten Yvind. Especially Kresten is thanked for teaching me almost everything that I know about mode-locked lasers. He is also thanked for sharing his knowledge about cleanroom laser processing. Most of all he his appreciated for his guidance concerning the progress of this PhD-project.

Lotte Christiansen did the processing of some of the lasers that have been investigated in this thesis and she also introduced me to the practical processing work on the standard ridge waveguide lasers. She is much appreciated for this and also for introducing me to the wonderful music of Hôtel Costes.

The discussions with Professor Ole Hansen concerning reactive ion etching have been invaluable while more practical help with the processing have been given by the personnel at the Danish National cleanroom facility (Danchip): Peixiong Shi helped me with developing a suitable e-beam process, Jonas Michael Lindhard thought me how to take good SEM-graphs and Roy Cork and Thoger Eskildsen are also recognized for their practical help.

I would also like to thank all my colleagues in the Nanophotonics (and former Optoelectronics) group, Mike van der Poel for his enthusiasm and for sharing common interests outside the field of work, Jens for being silly and Tine for being so full of fun energy, to mention a few. I thank Filip for good companionship on some of our long journeys to Sweden and also for proof-reading parts of the thesis.

A great number of people from the Systems group are thanked for their good companionship in Optolab, especially Beata and Christophe. I would also like to thank Christophe Peucheret for always being so generous with the equipment of the System group. Prof. Palle Jeppesen is thanked for valuable discussion on RF-oscillators. Leif Oxenløwe is thanked for the time he has taken to explain OTDM-systems and for his proof-reading. Rasmus who was a former member of my group (now in Systems) is thanked for introducing me to the document preparation system LyX and for sharing my interest of photography.

I thank the guys in COM's mechanical workshop, Frank Persson, Jan Mortensen and Martin Nielsen, who helped me not only with realising some of the equipment used but also improved the design of them.

Lone Bjørnstjerne is recognised for her perfect services concerning all administrative work, ranging from travels to paternity leaves. She is also recognised for her cheerful appearance and humor.

Last but not least I would like to thank Malena for putting up with me working on week-ends, being away from home for very long days, and for preparing the dinner, taking care of our son and doing most of the household work during the last six months of this project.

Abstract

This thesis deals with the fabrication and characterisation of monolithic semiconductor mode-locked lasers for use in optical communication systems. Other foreseeable applications may be as sources in microwave photonics and optical sampling. The thesis also deals with the design and fabrication of intracavity monolithically integrated filters. The common denominator among the different parts of the thesis is how to achieve and measure the lowest possible noise. Achieving low noise has been pinpointed as one of the most important and difficult challenges for semiconductor mode-locked lasers.

The main results of this thesis are a fabrication process of a monolithic and deeply etched distributed Bragg reflector and a characterisation system for measurement of quantum limited timing noise at high repetition rates. The Bragg reflector is a key component in achieving transform-limited pulses with low noise. The novel fabrication process enables the realisation of Bragg reflectors without regrowth, by post-growth processing (etching), thereby enabling low-cost foundry growth of the semiconductor wafer. The characterisation system, which is the first of its kind operating at such high speeds as 40 GHz, is important when distinguishing the noise between different low-noise designs (e.g. number of quantum wells or with or without intracavity filter), each having noise below the noise floor of more common characterisation systems. It has measured record low timing noise (54fs in 10kHz-20 GHz) from all-active 40-GHz lasers with 1 ps-pulses. Overviews are given of selected parts of the existing noise theories for mode-locked lasers, semiconductor intracavity filters and timing noise characterisation systems.

Resumé

Denne PhD-afhandling omhandler fabrikation og karakterisering af mode-låste monolitiske halvlederlasere til brug i optiske kommunikationssystemer. Andre mulige anvendelser kunne være som pulsede lyskilder i mikrobølgefotonik og til brug ved optisk sampling ved høje samplingsrater. Da det er nødvendigt at anvende optiske båndpasfiltre på mode-låste monolitiske lasere ved brug i reelle kommunikationssystemer, omfatter afhandlingen også design og fabrikation af disse. For alle dele af afhandlingen er den genemgående fællesnævner hvorledes der opnås det lavest mulige støjniveau og hvordan det måles. Dette skyldes at et lavt støjniveau er udset til at være en af de største og vigtigste udfordringer for mode-låste diode lasere.

De primære resultater af afhandlingen er en fabrikationsproces for fremstillingen af en monolitisk og dybt-ætset distribueret Bragg-reflektor samt et karakteriseringssystem til måling af kvantebegrænset timing-støj ved høje repetitionsrater (40 GHz). Bragg-reflektoren er en af nøglekomponenterne når det drejer sig om at opnå pulser gode nok til optiske kommunikationssystemer: transformbegrænsede pulser med lavt støjniveau, designbar optisk bølgelængde og justerbar repetitionsfrekvens. Den nye fabrikationsproces, som framlægges her, muliggør fremstillingen af Bragg-reflektorer uden brug af overdyrkning. I stedet anvendes udelukkende efterprocessering (ætsning) og på den måde bliver en industriel fremstilling med store volumerer og lave omkostninger mulig eftersom selve grundmaterialet til laserne kan købes fra store og omkostningseffektive fabrikker. Det opbyggede karakteriseringssystem, der er den første af sin art der virker ved 40 GHz, er en nødvændighed for at kunne skeldne støjen fra forskellige typer af støjsvage lasere (disse typer adskiller sig bl. a. ved antallet af kvantebrønde eller antallet af kvanteprikke lag, samt ved om der er implementeret intrakavitetsfilter eller ej), da de alle har et støjniveau under støjgulvet for normale karakteriseringssystemer. I afhandlingen gennemgås endvidere utvalde deler af existerende teori for støj i modlåste lasere, halvlederintrakavitetesfiltre og målesystemer for tidstøj.

Ph.D. publications

1. "Low jitter and high power all-active mode-locked lasers," Yvind, Kresten ; Larsson, David ; Christiansen, Lotte Jin ; Angelo, Casper Stein ; Oxenløwe, Leif Katsuo ; Mørk, Jesper ; Birkedal, Dan ; Hvam, Jørn Märcher ; Hanberg, Jesper part of: ECOC-IOOC 2003 Proceedingspages: 320-321, 2003.

2. "Low-jitter and high-power 40 GHz all-active mode-locked lasers," Yvind, Kresten ; Larsson, David ; Christiansen, Lotte Jin ; Angelo, Casper Stein ; Oxenløwe, Leif Katsuo ; Mørk, Jesper ; Birkedal, Dan ; Hvam, Jørn Märcher ; Hanberg, J. in journal: IEEE Photonics Technology Letters (ISSN: 1041-1135) vol: 16, issue: 4, pages: 975-977, 2004.

3. "High-performance 10 GHz all-active monolithic mode-locked semiconductor lasers," Yvind, Kresten ; Larsson, David ; Christiansen, Lotte Jin ; Mørk, Jesper ; Hvam, Jørn Märcher ; Hanberg, Jesper in journal: Electronics Letters (ISSN: 0013-5194) vol: 40, issue: 12, pages: 735-736, 2004.

4. "Novel design of low-jitter 10 GHz all-active monolithic mode-locked lasers," Larsson, David ; Yvind, Kresten ; Christiansen, Lotte Jin ; Mørk, Jesper ; Hvam, Jørn Märcher ; Hanberg, Jesper part of: 2004 CLEO/IQEC Technical Digest CD-Rom (ISBN: 15-57-52770-9), 2004.

5. "Low-jitter prescaled clock recovery with compact semiconductor components for ultra high-speed OTDM systems," Oxenløwe, Leif Katsuo ; Christiansen, Lotte Jin ; Larsson, David ; Yvind, Kresten ; Clausen, Anders ; Seoane, Jorge ; Siahlo, Andrei ; Sørensen, Brian Michael ; Jeppesen, Palle, part of: OECC 2004, pages: 888-889, 2004, Japan.

6. "Pre-Scaled clock recovery with compact semiconductor devices for ultra high-speed OTDM systems," Oxenløwe, Leif Katsuo ; Christiansen, Lotte Jin ; Larsson, David ; Yvind, Kresten ; Clausen, Anders ; Seoane, Jorge ; Siahlo, Andrei ; Sørensen, Brian Michael ; Jeppesen, Palle, part of: Proc. of ECOC 20042004, Sweden.

7. "Measurements of record-low residual jitter in 40-GHz monolithic mode-locked lasers," Larsson, David ; Yvind, Kresten ; Hvam, Jørn Märcher part of: CLEO/QELS 2005 Technical Digest CD-Rom (ISBN: 15-57-52770-9) pages: 3 pages, 2005.

8. "Mode-Locked Semiconductor Lasers for Optical Communication Systems," Yvind, Kresten ; Larsson, David ; Oxenløwe, Leif Katsuo ; Hvam, Jørn

Märcher part of: Proceedings of 2005 7th International Conference on Transparent Optical Networks (ISBN: 07-80-39236-1) pages: 209-212, 2005, IEEE.

9. "Design and evaluation of modelocked semiconductor lasers for low noise and high stability" Yvind, Kresten ; Larsson, David ; Christiansen, Lotte Jin ; Oxenløwe, Leif Katsuo ; Mørk, Jesper ; Hvam, Jørn Märcher ; Hanberg, Jesper part of: Proceedings of SPIE (ISBN: 08 19-45810-4) pages: 37-48, 2005, SPIE.

10. "Wide-band residual phase-noise measurements on 40-GHz monolithic modelocked lasers," Larsson, David ; Yvind, Kresten ; Hvam, Jørn Märcher in journal: IEEE Photonics Technology Letters (ISSN: 1041-1135) vol: 17, issue: 11, pages: 2388-2390, 2005.

11. "An in-situ monitoring technique for optimizing antireflection coatings using a monolithic integrated photodetector," Saini, Vikram ; Yvind, Kresten ; Larsson, David, in journal: Semiconductor Science and Technology (ISSN: 0268-1242) (DOI: 10.1088/0268-1242/21/8/008) vol: 21, issue: 8, pages: 1030-1033, 2006.

12. "Monolithic Hybrid and Passive Mode-Locked 40GHz Quantum Dot Laser Diodes," Thompson, M. G. ; Larsson, David ; Rae, A. R. ; Yvind, Kresten ; Penty, R. V. ; White, I. H. ; Hvam, Jørn Märcher ; Kovsh, A. R. ; Mikhrin, S.S. ; Livshits, D.A. ; Krestnikov, I.L. part of: Proceedings European Conference on Optical Communication (paperid: We4.6.3) 2006, ECOC.

List of frequently used acronyms

BER	Bit Error Rate
DBR	Distributed Bragg Reflector
EBL	Electron-Beam Lithography
EC	External Cavity
ECMLL	External Cavity Mode-Locked Laser
ESA	Electrical Spectrum Analyzer
FP	Fabry-Pérot
LO	Local Oscillator
MLL	Mode-Locked Laser
MLLD	Mode-Locked Laser Diode
MMLL	Monolithic Mode-Locked Laser
MORIE	Metal-Organic Reactive Ion Etching
MOVPE	Metal-Organic Vapour Phase Epitaxy
NF	Noise Figure
OTDM	Optical Time Division Multiplexing
RIE	Reactive Ion Etching
RIN	Relative Intensity Noise
RMS	Root Mean Square
SEM	Scanning Electron Microscopy
SSB	Single-SideBand
TFL	Transform Limited
TBP	Time-Bandwidth Product
WDM	Wavelength Division Multiplexing

Contents

Chapter 1

Introduction and background

1.1 Mode-locked lasers

1.1.1 What is a mode-locked laser?

The first thing that the curious reader of mode-locked literature will ask is probably what the name mode-locked refers to. We shall start in another end for the moment. The most characteristic feature of a mode-locked laser is the way it emits its light: in a (continuous) stream of pulses with a fixed repetition rate given by the round-trip time of the laser cavity, $f_{rep} = c/2n_gL$, where c is the speed of light, n_g is the group index and L is the length of the cavity. When the first mode-locked laser (MLL) was reported (it was a solid-state laser in the 1960s [1]), there were already other types of lasers that also could emit pulses, such as gain switched and Q-switched lasers. However, even though mode-locked lasers might be slightly more complex than the other types, they are today by far the most common sources of short light pulses because of the superior performances. The main disadvantage of the other two methods is the much longer pulses. In Q-switching, laser action is hindered by a saturable absorber or by a manual Q-switch. When the gain has increased enough to bleach the absorber a giant pulse is formed which builds up until the gain medium is depleted, usually after many roundtrips [2]. In gain switching the laser current is modulated, and the optical pulse width is limited by the charge in the electrical pulse and the electrical pulse width [3]. The repetition rate is also limited to the modulation bandwidth of the laser. Another problem with gain switching is that the shape, width and frequency of the pulses have large variations [3].

Mode-locked means that the phases of adjacent longitudinal modes are locked to each other, i.e. there is a constant phase relation between the modes. Mode-locking is a phenomenon where a pulse is formed by enforcing coherence between the longitudinal modes. The pulse can be seen as a coherent superposition, a "supermode", of the locked longitudinal modes [4, 5].

Common for the output light of in principle all mode-locked lasers are certain characteristics like short pulses (5 fs - 50 ps), high peak intensity (W-MW), and a fixed repetition rate (kHz-THz) with a low timing jitter (variation of repetition rate). How we can exploit these characteristics of mode-locked lasers will be discussed in section 1.1.2.

Semiconductor mode-locked lasers Mode-locked lasers come in many different varieties today. This PhD-project is concerned with semiconductor MLLs or MLLDs where D stands for diode. In fact, it's only concerned with monolithic MLLDs (or MMLLs). In a monolithic MLLD the entire cavity is formed by the semiconductor chip alone, in contrast to semiconductor mode-locked lasers with an external-cavity. A schematic drawing of a MMLL is shown in figure 1.1. Semiconductor lasers offer several advantages over other types; they have extremely good long and short term stability, i.e. low fluctuation of the output, and they have a long lifetime. They are very small and thus take up a small space. Their short cavities enable very high repetition rates, e.g. 350 GHz have been demonstrated [6]. The manufacturing method is borrowed from the IC-industry, meaning that large scale parallel manufacturing is possible with small variations of the performance. This also allows for integration of the lasers with other passive or active optoelectronic components, such as filters, modulators and multiplexers. Semiconductor laser generally also have a low power consumption compared to other laser types.

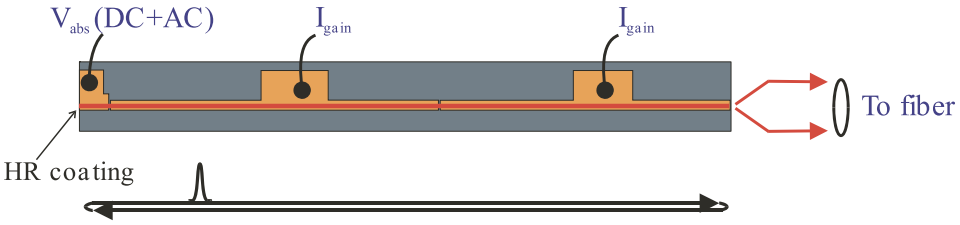

Figure 1.1: Drawing of a monolithic diode mode-locked laser.

There are of course some limitations with semiconductor lasers compared with other materials (e.g. solid-state and dye). The most severe is the limitation on the pulse width. Gain and absorber recovery times are usually in the picosecond range (limited by the movement of carriers in real space). Partial recovery can be ten times faster, limited by the intraband relaxation time of carriers, ~100 fs (carrier-carrier scattering time). Even with the use of the ultrafast effects, it will be difficult to achieve pulse widths from semiconductor lasers below 100 fs, which is 20 times longer than the shortest pulses made.

Table 1.1 presents some of the advantages and drawbacks of different types of semiconductor mode-locked lasers.

1.1.2 Applications of mode-locked lasers

Applications of mode-locked lasers fall into four major categories that rely on the four most prominent characteristics of mode-locked lasers: short events in time, high intensity, high repetition rates and high timing stability.

Short events "In order to measure an event in time, you need a shorter one.", says Rick Trebino (the Guru of short pulse measurements) [33]. Pulses from mode-locked lasers are the shortest man-made events that we know of (~5 fs). Thus if one can control the emission and reception of them, they should be well suited for sampling of other almost as short events, may they be electrical, optical, chemical or biological. Concrete examples of ultrafast sampling are: Analogue to Digital

Table 1.1: Advantages and drawbacks of different types of diode mode-locked lasers. FP: Fabry-Pérot, DBR: Distributed Bragg Reflector, BW: Bandwidth. Repetition rates are typical.

Type	Advantages	Drawbacks	f_{rep} (GHz)	Application
External Cavity	Low noise, tuneable	Difficult fabrication, complex to get low noise	≤ 10	Laboratory
Monolithic-FP	Easy fabrication, high rep. rates, short pulses	No spectral control, difficult to achieve low rep. rates	10-350	Telecom
Monolithic-DBR	Designed wavelength and BW	Complex fabrication, difficult to achieve low rep. rates	10-160	Telecom Optical sampling Microwave photonics

Converters (ADCs) for probing of ultrafast electrical signals and pump-probe measurements for probing a medium's response to another more powerful light signal.

High intensity The high peak intensity can be advantageous when exploiting non-linear physical effects that are proportional to the electromagnetic field magnitude to third (or higher) order. These effects, like Second Harmonic Generation (SHG) and Two Photon Absorption (TPA) are very sensitive to the intensity. SHG has applications in autocorrelation and frequency doubling, and TPA has applications in biological probing.

High repetition rates The high repetition rates of MLLs means that mode-locked lasers can be used for sending large quantities of information between people, i.e. high speed optical communication. Compared with the current commercial systems there could be several advantages of using mode-locked lasers when looking ahead for future very high speed communication systems. In these pulsed communication systems (see section 1.2), MLLs can be used as the sources of the pulses but they can also be used for optical clock-recovery (needed for demultiplexing, and for retiming data) and demultiplexing. The many functionalities means that MLLs will probably be essential for these Return-to-Zero (RZ) communication systems. Monolithic diode lasers are well suited for all applications in pulsed optical communication systems. The requirements on the lasers for these applications will also be discussed in section 1.2. Other applications that rely on high repetition rates are microwave photonics (up to subTeraHertz) and ultrafast optical sampling of electrical signals in analogue to digital converters, and they will be briefly presented in section 1.3.

Timing stability The timing stability of MLLs make them suitable as optical clocks. Future applications could be as clocks in computers and between integrated circuits. Monolithic diode lasers are preferred for this because of their compact size, robustness and temperature insensibility. MLLs with extremely broad spectral emission could be used as frequency standards. Pulsed communication systems also need high timing stability.

Applications for edge emitting diode mode-locked lasers Semiconductor mode-locked lasers do not produce the shortest pulses, nor the most intense. Applications are of course adapted after the diode lasers unique qualities, such as high repetition rates, high timing stability and the combination of both. Their small size and low power consumption is of course favourable when integrating the lasers in larger systems in the real world, outside the laboratory. The next two sections describe the most probable applications for the fabricated and characterised lasers in this thesis.

1.2 High-speed optical communication systems

The mode-locked lasers described in this PhD-thesis have been developed to be deployed in fibre optic communication systems. The main advantage of using short pulse lasers in optical communication systems is an increase in bandwidth (capacity: data/s*km), see section 1.2.1. Other advantages might be new functionalities in the communication system through optical signal processing with the MLLs. The new functionalities could offer less complexity or lower cost. With optical signal processing instead of electrical signal processing, a large amount of optical to electrical and electrical to optical transitions would be omitted, thereby reducing the cost for huge amounts of power consumption. This section presents a background to the communication systems that deploy mode-locked lasers, and to some of the possible functionalities that these lasers may have.

Communicating with optical signals is maybe the oldest form of long distance communication. Old fashioned fire signals is one example. Today's optical communication was born in the nineteen seventies (the first field trial with a fibre optic link was performed in Chicago 1977 [7, ch. 5]) after an over 100-year era of electrical communication over copper wires. The birth was triggered by two major breakthroughs in physics: the semiconductor laser and the optical fibre.

Commercial fibre optic communication systems today Today's communication systems are based on the low loss transmission of light in optical fibres made of silica. Signals can travel several tens of kilometers before needing amplification. Many of the functionalities in these fibre based networks are performed by optoelectronic chips, such as lasers, modulators and photodetectors. The laser is the most central part of an optical transmitter (which converts electrical signals into optical and launches them into a fibre). In future communication systems however, special kinds of lasers, such as MLLs might have other functionalities also. More about this in section 1.2.1.

The research in optical communications today focuses on how to efficiently use the large bandwidth of the fibre medium and the lasers' gain media. Information can be transmitted at much higher rates than it currently can be created

or detected. The low loss region around 1550 nm now extends to about 120 nm (∼16THz) [7]. However in practice the use of erbium doped fibre amplifiers (EDFA) limits the usable bandwidth. Equation 1.1 is a calculation of the ratio of the bandwidth of a commercial EDFA covering the so-called C-band (central band, ∼1530-1560 nm), BW_{EDFA} to the bandwidth of a single channel (40 GHz is not deployed yet in commercial systems but can be found at research institutes) BW_{ch} .

$$R_{BW} = \frac{BW_{EDFA}}{BW_{ch}} = \frac{4THz}{4 \cdot 40GHz} = 25 \tag{1.1}$$

This large ratio means that it's possible to multiplex several laser channels (up to 25 in this case, with a channel spacing 4 times the bitrate [7]) as long as they do not overlap in wavelength.

Since the electrical modulation of optoelectronic devices currently is limited to around 40 GHz commercially and is expected to increase marginally in the future to less than 100 GHz, researchers are currently exploring optical methods of combining (multiplexing) and parting (demultiplexing) the GHz-signals into THz-signals. Currently the two most successful multplexing schemes are Wavelength Division Multiplexing (WDM) and Optical Time Division Multiplexing (OTDM). In WDM, lasers operating at different wavelengths are used to transmit data at different wavelengths, thereby increasing the bandwidth to the number of wavelength channels times the bandwidth of one channel. WDM has been successfully installed in commercial optical networks during the 90's. In laboratories the record aggregate bandwidth achieved by WDM exceeds 10 Tb/s over transmission distances of over hundreds of kilometers. The next subsection will treat OTDM systems and why MLLs are important to them.

1.2.1 Optical Time-Division Multiplexing

Instead of trying to maximise the number of wavelength channels over the bandwidth of the fibre, where each channel has a bitrate limited by the modulating electronics, we could try to maximise the optical single channel bitrate to far above the electronic limit by using optical techniques. This is possible since special kinds of lasers (e.g. mode-locked lasers) can produce light pulses much shorter than the duration of the fastest electrical signals, and with a stable repetition rate of e.g. 10, 40 or 160 GHz. The combination of the signals is relatively easy achieved by delaying different signals with different amounts of passive delay lines. Small, stable and accurate delay lengths can be obtained with lithographically defined planar lightwave circuits on e.g. silica-on-silicon or more preferably InP. With the latter material system one could also integrate the modulators [8], the MLL and an amplifier. Figure 1.2 describes a simplified OTDM system. Starting at the transmitter side, a pulse train with a low base rate, B_b is divided with a splitter and N replicas are formed (in this case 4). Data (at the base rate) is then added to each replica through Non-Return-to-Zero modulation with an external modulator and the modulated Return-to-Zero (A Return-to-Zero signal means that the intensity between two consecutive ones drops to zero) pulse trains are combined (multiplexed, MUX) in the optical domain to achieve a high aggregate line rate, $B_l = N \cdot B_b$ (e.g. 160 Gb/s = 4*40 Gb/s). The pulse width, T_p must be shorter than the bit slot of the line rate, B_l^{-1}. After the transmitter the time multiplexed signals are transmitted over some lengths of fibre, where dispersion compensation

will be required. Before demultiplexing (DEMUX) the signal in the receiver end we should consider functionalities such as add-drop nodes and regeneration. All these functionalities require recovery of the clock rate from the data signal.

OTDM transmission has been studied in laboratories since the early 90's but has yet to reach the commercial arena. Although WDM systems seems to be preferred over OTDM systems today, research on OTDM systems are still interesting. A combination of WDM and OTDM might be a way of achieving future ultra high-speed systems as in [9], with an aggregate line rate of 3 Tb/s. OTDM systems are also interesting in order to investigate the effects of transmission at ultra-high bit-rates. Numerical simulations suggests that during transmission the RZ-format is superior to the NRZ-format, with respect to dispersion and non-linearities, if one wants to upgrade the existing SMF network to higher bitrates than the existing 10 Gb/s (e.g. 40 Gb/s) [10].

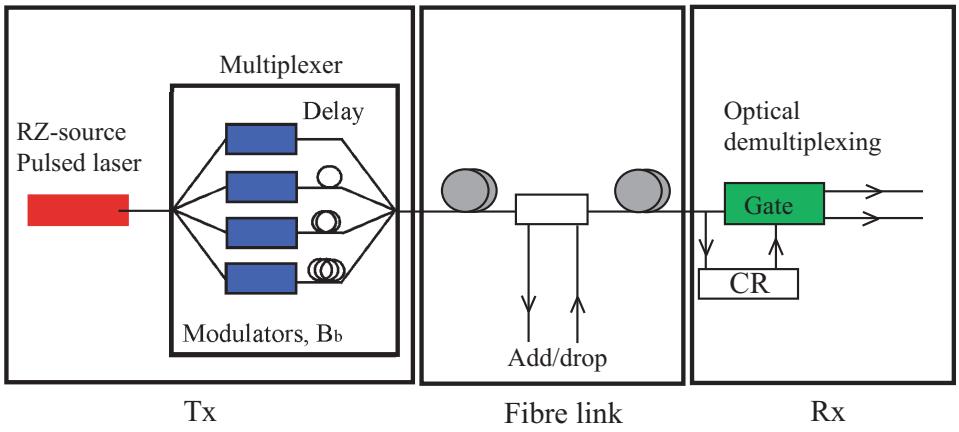

Figure 1.2: Point-to-point OTDM link with add-drop node. RZ, Return-to-Zero, Tx, transceiver, Rx, receiver, CR, clock-recovery.

MLLs in OTDM systems The first need for semiconductor mode-locked lasers in OTDM-systems were as pulse sources for the transmitter. The requirements for such pulse sources are listed below.

Short pulses The width of a pulse is usually characterised by it's full-width half-max (FWHM) value, but when packing many pulses closely together the shape and background of the pulse becomes important too. The maximum allowable pulse width will therefore vary with pulse shape and background level. For ideal pulses with no background a width of half the bit slot is sufficient for less than 1 dB power penalty in the receiver [11]. For pulses with background, the pulse to tail extinction ratio (PTER) and the number of multiplexed channels determine the required pulse width. A PTER of 27 dB and a FWHM of 0.4 times the timeslot is enough for transmission of 4x40 Gb/s with less than 1 dB penalty [11]. The bit slot of a 160 Gb/s system is 6.25 ps.

Repetition rate High base rates, such as 10 or 40 GHz, are desired in order to obtain a high line rate without having to multiplex too much, which in-

creases the complexity. The laser must also be able to meet the standardised pre-defined frequencies such as the STM64 (Standard Transmission Module) frequency 9.95328 GHz. The only way of meeting such a frequency over long periods of time is to synchronise the pulse source to an electrical oscillator (which is needed anyway to synchronise the repetition rate of the pulses with the data modulator).

Noise High timing stability is required since clock-extraction is needed when demultiplexing or re-timing the signals. In [12] a maximum timing jitter of 1/12 the bit slot was required to successfully demultiplex the base rate signal with a bit-error-rate$<10^{-9}$, see also chapter 2 for more information. A maximum amplitude noise of 7 % of the average optical power is allowed in the receiver.

Power The average power of the laser is seldom an issue since amplifiers exists, but for practical reasons a minimum output power of 5 to 10 dBm is desireable [13].

Wavelength The wavelength of the source must fit to the existing fibre amplifier windows, e.g the C-band and to one of the existing ITU-T wavelengths (today on a 100 GHz grid).

Semiconductor MLLs are good candidates as these pulse sources since they can meet all the requirements and also be cheap, small in size, robust and have a low power consumption.

As mentioned earlier clock-recovery is essential for OTDM-systems. MLLs may also be used for CR. Two different clocks are important: the base rate clock, or the so-called pre-scaled clock, and the line rate clock. Switching single channels from the aggregate bit train, as in DEMUX or add-drop, requires a pre-scaled clock, while retiming pulse trains for regeneration requires the line rate to be extracted. Different schemes for CR exist, such as using phase comparators together with phase-locked loops or using all-optical techniques. MLLs can been used in both these schemes. In [14] an optical phase-locked loop, with an semiconductor optical amplifier (SOA) as phase comparator and an MMLL as pulse source, were used for pre-scaled clock-extraction from 160 Gb/s data to a 10 GHz electrical clock. All-optical techniques of recovering the clock are very attractive, since they offer less complexity, less space and potentially higher speeds. Such an all-optical technique is injection-locking of monolithic mode-locked lasers. The data is injected into a free running (passive) MLL, which synchronises to the bitrate. For pre-scaled CR a laser with a subharmonic repetition rate is used, while retiming can be done with a laser operating at the line rate. All-optical clock-extraction to 10 [16] and 40 GHz [17] base rate has been performed at speeds up to 160 Gb/s. All-optical CR at the line rate by injection-locking MMLLs have been performed at line rates of e.g. 40 GHz [18]. The record of CR of a 160 GHz clock has been achieved for a colliding-pulse mode-locked laser structure [19], but also with a 260 μm short DBR-MMLL [20]. When using MMLLs for CR, the requirements on the pulsewidth might be relaxed, while the hardest requirements will be imposed on the timing jitter.

The combination of CR and gating will allow us to demultiplex signals to the base rate in a receiver or at an add-drop point. The clock signal derived from the data stream gates the data to be demuxed in for example a saturable absorber. In [21], Ogura et al. used the saturable absorber in a MLLD as a switching gate to demultiplex a 40 Gb/s signal to a 10 Gb/s signal. 10-GHz clock pulses where

injected from the semiconductor optical amplifier (SOA) side and gated the data pulses through saturation of the absorber during the clock pulse.

Optical 3R-regeneration (reamplification, reshaping, and retiming) will be important at high speeds and long fibre spans. All Rs can be performed with MMLLs. Clock-recovery at the line rate is performed in a first MMLL as described above. The SOA-section of a second MMLL is used to amplify the data stream and the absorber section is used to gate the derived clock pulses with the degenerated data. Such regeneration has been performed at 20 Gb/s data with no power penalty in BER [22]. These examples should be evidence of the potential of MMLLs in optical communication systems.

1.3 Other applications

1.3.1 Microwave photonics

The pulses from MLLs can be used as (sub)carriers for analogue modulation at microwave frequencies, so-called RF-photonics, feeding miniature antenna sites. The current system uses coaxial cables with a very limited bandwidth compared to optical fibres. Such networks are used in wireless local area networks (WLANs), vehicle routing and video on demand [23]. A sinusoidal signal is required meaning a narrow spectrum. For optical carriers this translates into having most of the power in 2 main longitudinal modes. This makes narrowband MMLLs with integrated filters, such as the Distributed Bragg Reflector (DBR), advantageous [24] for this application. Frequency tuneability is also desirable from an RF-generator [23], which again favour DBR-type lasers.

1.3.2 Optical sampling

As mentioned in section 1.1.2, the pulses from mode-locked lasers can be used as probes to measure other short events in time. This is a kind of sampling, where the optical pulse samples with a given repetition rate. The high repetition rate of monolithic semiconductor mode-locked lasers make them suitable for sampling at very high sampling rates. This can be used for sampling analog electrical signals and converting them into digital signals, so-called optically sampled analogue-to-digital converters. Many optical samplers make use of a Mach-Zender interferometer, where the electrical signal to be sampled modulates the voltage, and hence the intensity of the optical pulses passing through it. A good review over recent work (until 2001) is given in the invited paper by Juodawlkis et al. [25]. At high sampling rates the timing jitter of the system is a limiting factor [25, 26]. According to [27, Appendix D] the requirement on the timing jitter is given by equation 1.2, which is plotted for some different quantisation levels, N, in figure 1.3.

$$\Delta t < \frac{1}{\pi \nu_{sampling}} \frac{1}{2^N} \tag{1.2}$$

The timing jitter of present electronic samplers is in the ps-range, while jitter of MLLDs can be in the tens-of-fs-range, thus increasing the possible sampling speed with at least a decade. Amplitude noise on the other hand can be rejected with up to 60 dB [28]

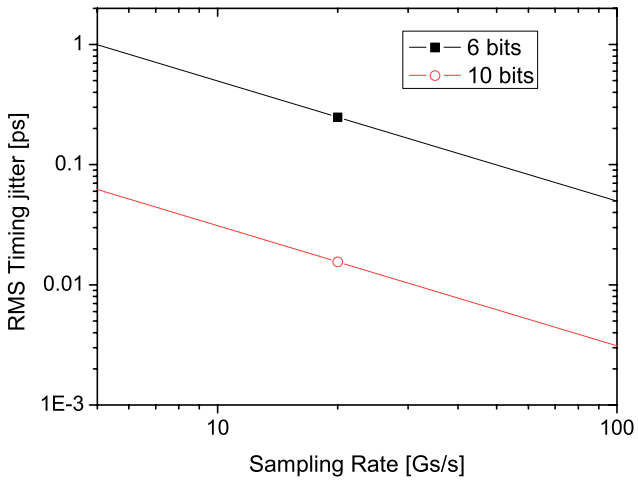

Figure 1.3: Requirement on timing jitter for ADCs as a function of sampling rate and quantisation levels.

1.4 Pulse formation in mode-locked lasers

Mode-locking is a method to produce pulses from a laser by means of locking the longitudinal modes of the laser in phase (i.e they have a constant relative phase). Mode-locking is a resonant phenomenon: a small modulation in each roundtrip will shape the pulse and make it shorter and shorter (and the spectrum wider and wider) until pulse widening mechanisms or spectral narrowing takes over [2]. Once the pulse has formed and we are in a steady state, there are a number of pulse shaping mechanisms within the laser cavity. The pulse is broadened from gain saturation (amplifying the leading part of the pulse more than the peak), bandwidth limiting elements, such as finite gain bandwidth or DBR-gratings and from dispersion (depending on the sign of the dispersion with respect to the chirp of the pulse, it can broaden it or narrow it). Saturable absorption and active modulation shortens the pulse.

There are two ways to obtain mode-locking, active and passive. They will both be shortly described in the following paragraphs. The mode-locked lasers that will be described, fabricated and characterised in this thesis are mainly passively mode-locked and thus passive mode-locking will be described in more detail.

Active Mode-locking Active mode-locking means that the non-linear modulation of gain or absorption is supplied from an external element. We imagine a resonator, e.g. an as cleaved semiconductor diode. The resonator contains a gain element, a positively biased section. By changing the current to the gain section non-linearly as a function of time, this modulation will produce a time-varying net gain in the cavity, forming a pulse, see figure 1.4 a). If the modulation frequency is chosen to coincide with the longitudinal mode spacing of the resonator (the round-trip time of the light in the cavity) then this time-varying gain will lock the relative

phase of the modes.

Passive Mode-locking A passive mode-locked laser does not need any external modulation to produce short pulses. In passive mode-locking non-linear gain or loss or a complex interplay between both will create a time window of net gain that favours a pulsed steady state regime, see figure 1.4 b) and c). In order to have a self-starting pulsation (without external pulse injection) there must be fluctuations in mode intensity [29, ch. 2]. The interplay of the fluctuations and the non-linear element will eventually form a pulse. For pulses to form, the non-linearity must create an amplitude instability so that a large fluctuation sees a larger gain compared to a weaker fluctuation. Such an amplitude instability could e.g. be a saturable absorption. In a semiconductor laser, both the gain and absorption can be made non-linear vs. the intensity.

When speaking about passive mode-locking one often talks about slow and fast saturable absorbers. A fast absorber is an absorber which can do all the pulse shaping on its own, i.e. has a saturation and relaxation time on the order of femtoseconds. Solid-state lasers usually have gain media with long relaxation times on the order of microseconds, and hence rely on having fast saturable absorbers. The semiconductor mode-locked laser relies on the combination of a gain with a fast relaxation-time (t_r $\sim$1 ns, relaxation of exited electrons) and an absorption with a slow saturation ($\sim$1 ps, sweep out time of carriers; although partial recovery can occur on a sub-ps level by carrier-carrier scattering). A basic requirement of the combination of gain and absorber materials is that the absorber must saturate stronger and have a faster recovery than the gain.

One of the challenges and design goals when making semiconductor mode-locked lasers is to design the gain and absorber material to have dynamic properties such that the window of net gain is made as short as possible, i.e. achieve short pulses. In chapter 3.1 I will give a short summary of the design ideas for the lasers studied during this project.

Hybrid Mode-locking If one synchronises the modulation of a passively mode-locked laser to an external modulation, this is called hybrid mode-locking. This can reduce the timing variations between pulses far apart (on a very long time scale), since the uncorrelated timing noise has a random walk dependence originating from the random nature of spontaneous emission and carrier shot noise [35]. If the pulses are not made substantially shorter by the active modulation the primary pulse shaping mechanism is still passive. In the case of a semiconductor saturable absorber this modulation can also increase the speed of the absorber by a faster carrier sweep out and the pulse shaping is then a combination of active and passive mode-locking [30, chapter 3].

1.5 Basic pulse characterisation methods

The interesting properties of a pulse train from a MLL depends on the application. But usually one is interested in knowing the pulse duration, the temporal shape and phase, the spectral width and shape, the repetition rate and the average power or the pulse energy. Noise properties are interesting for some applications, e.g.

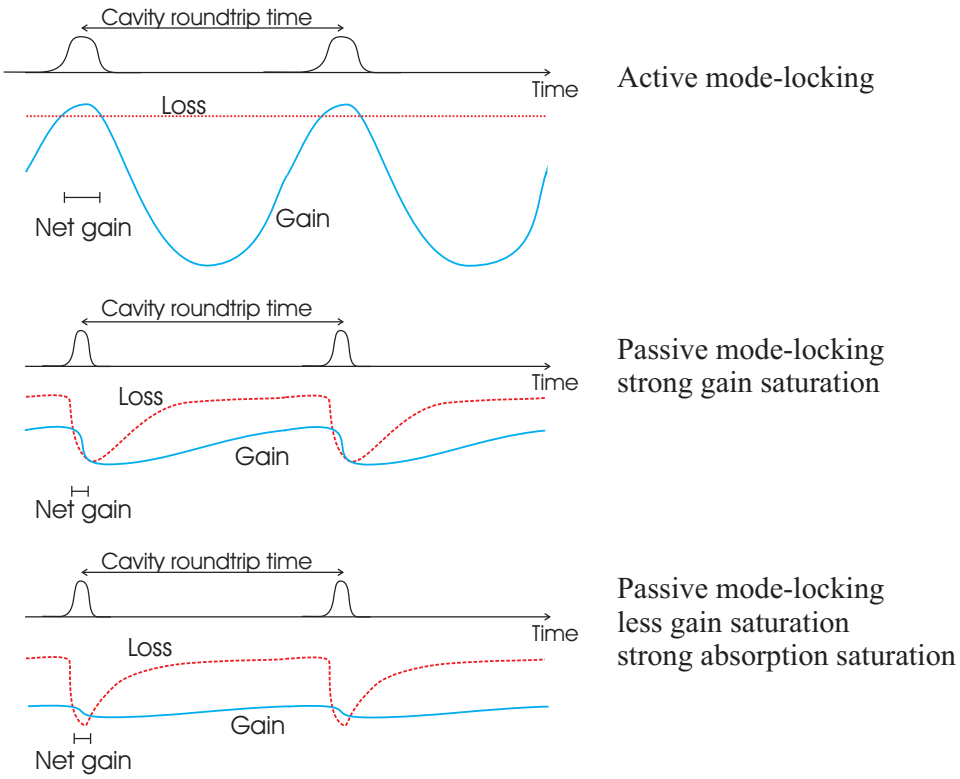

Figure 1.4: Schematic of pulse formation in the time domain, for a) active mode-locking and b) and c) passive mode-locking with a slow absorber.

fibre based communications, but a detailed description of the characterisation of noise in MLLDs will be given in chapter 5.

The autocorrelation Ideally we would like to measure the complete temporal pulse shape (intensity) and phase during the pulse. However, to sample a short event requires an even shorter event. Since mode-locked lasers are among the shortest man-made events this can be quite tricky. Picosecond laser pulses could of course be sampled by femtosecond pulses, but these are not just lying around everywhere.

The most widespread method of measuring picosecond pulse shapes is the intensity autocorrelation, see figure 1.5; a sampling of the pulse with a delayed replica of itself in a non-linear medium (for example a second-harmonic generating crystal). The measurement does not deliver the pulse shape, $I_p(t)$ itself but the shape of a function, $I_{ac}^{SHG}(\tau)$ that is dependent on the pulse intensity shape and its delayed replica, $I_p(t-\tau)$

$$I_{ac}^{SHG}(\tau) \propto \int_{-\infty}^{\infty} I_p(t) I_p(t-\tau) dt$$

Since the autocorrelation function is symmetric in it's nature, a lot of information on the actual pulse shape is lost in the measurement. However, if the pulse is

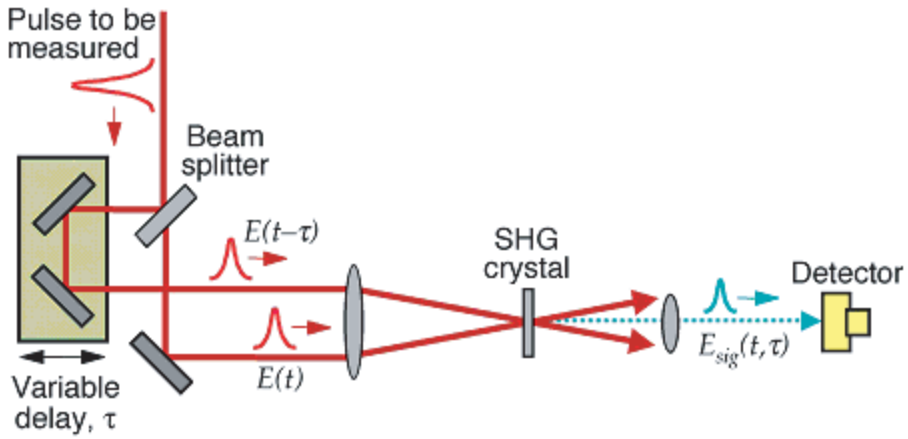

Figure 1.5: Schematic of a second-harmonic generation (SHG) autocorrelator.

somewhat well behaved we can fit the trace to the calculated autocorrelation function for an assumed pulse shape, such as a Gaussian or hyperbolic secant. Usually the result from such a measurement is quoted as a pulse width in the the form of a FWHM-value, which then can be compared with FWHM widths from any other laser in the world. Unfortunately pulses are not always perfect Gaussians or hyperbolic secants and thus the FWHM width is not always a good measure of the length of the pulse. As an example, in OTDM-systems the power in the next bit slot is of more importance than the FWHM width. The autocorrelations in chapter 5 are so-called background-free autocorrelations, characterised by an angle between the two beams, and by a thick crystal, see figure 1.5. One advantage of the background-free autocorrelation is that it's possible to measure the extinction ratio of the pulse train, i.e. the ratio of the peak intensity to the intensity halfway between two pulses. By combining with lock-in techniques, ratios over 35 dB can be obtained.

Frequency-Resolved Optical Gating (FROG) A characterisation method that does deliver complete pulse shape and phase is Frequency Resolved Optical Gating (FROG), invented by Rick Trebino and Daniel J. Kane in 1993 [31]. The special case of FROG using SHG as non-linear element was presented in [32]. Here we will only discuss SHG FROG since this is the only FROG measurement that can measure the relative weak pulses from monolithic MLLs. The SHG FROG also uses an autocorrelator, but resolves the gated signal spectrally for each delay point. The spectrally resolved signal is the so-called spectrogram of the signal, a plot of the intensity versus frequency and time. The spectrogram can yield the pulse field and phase by using a two-dimensional phase-retrieval algorithm. An excellent textbook on FROG is [33]. There are some difficulties with FROG though. Large pulse powers are needed to obtain a good trace since the FROG-signal is proportional to the intensity squared. For high repetition lasers the average power needs to be high, 25 dBm or higher, which in the case of monolithic semiconductor lasers only can be achieved by external amplification (e.g. with an EDFA). Other minor

problems when it comes to SHG FROG, is that the spectrogram is not as intuitive as in the case of third order FROG and that an ambiguity in the direction of time exist.

The spectral width and shape is of importance for optical communication systems, because of use of wavelength multiplexing and dispersion in fibers. The optical spectrum is the Fourier transform of the time-dependent electrical field, which can be retrieved with FROG. If FROG is not available the average optical spectrum can easily be obtained from an optical spectrum analyzer (OSA).

The figure-of-merit for mode-locked lasers is the time-bandwidth product (TBP). It is what it sounds to be, the product of the width of the pulse in time and frequency domain, $TBP = \Delta t \Delta \nu = \Delta t c \frac{\Delta \lambda}{\lambda^2}$. For a given pulse width and shape there is a minimum spectral width and thus a minimum value of the TBP, the transform-limit (TFL), which occurs for a flat temporal phase. Since the spectrum and temporal field are related through the Fourier transform, which is symmetrical, the shortest pulse width is obtained for a given spectrum when the spectral phase is constant. A constant phase is the same as an unchanged average frequency during the pulse (the pulse is said to be unchirped). When a pulse is not transform limited, then the average frequency changes over the pulse and it is said to be chirped. Increasing frequency with time means blue-chirp (or up-chirp) while decreasing frequency means red-chirp (down). If the chirp is linear with time (i.e. the phase changes quadratically), then the pulse can be compressed by the dispersion in single mode fibre (either standard SMF or dispersion compensating (DCF) depending on the sign of the chirp). Often the chirp is of higher order and only part of the excess bandwidth is compressible. However pulse compressors that compensate for higher order chirp have been reported [34, ch. 7].

1.6 Structure of thesis

Chapter one have introduced the mode-locked laser to the reader, in particular the semiconductor MLL. Applications of MLLs were presented in short, while a lengthier presentation of optical high-speed communication systems was given, since that is the main application for monolithic MLLs. No system experiments have been performed during this project, so the description serves as a mere background. The next section was devoted to a background on pulse formation and pulse shaping in MLLs. Finally, some of the measurement methods used in this project (and also generally) to characterise MLLs were presented.

Chapter 2 is an overview of different aspects of noise in MLLs; its origin, how to model and measure it, and finally its consequences for applications, such as fibre optic communication systems. It should be pointed out that no theoretical work on noise has been carried out within this project. Chapter two is however essential for understanding the design of low-noise MLLs and for understanding the noise measurements in chapter 5.

Chapter 3 starts with an overview of the design of the gain material in monolithic mode-locked lasers with extremely low noise, and how to translate this design into epitaxy and real laser structures. The largest part of chapter 3 deals with the design of filters, monolithically integrated with the MLL (for lower noise and spectral and repetition rate control). Different types of filters and fabrication methods are compared. The design of a narrowband deeply etched surface Bragg grating is

presented. The results of the grating calculations (the calculations are presented in appendix A) in terms of reflectivity, bandwidth, effective length and dispersion are presented.

Chapter 4 covers the technological aspects of manufacturing the designed low noise lasers. A special emphasis is put on the physics and technology of dry etching of InP and related compounds for the realisation of deeply etched nanostructures, such as gratings. The fabricated DBR-lasers are the first reported mode-locked lasers with surface gratings, to the extent of my knowledge.

A smaller part of chapter 5 is devoted to characterisation of the fabricated surface gratings, while most of the chapter treats the performance of several types of monolithic mode-locked lasers (including the fabricated lasers with surface gratings). Comparisons of the noise level, in particular the timing jitter, between the different types are presented and discussed. A measurement system for the measurement of quantum limited noise in 40-GHz mode-locked is presented. Record-low jitter is presented and the noise spectrum is compared to theory.

Concluding remarks and outlooks for the future will be given in Chapter 6.

Chapter 2

Noise in mode-locked lasers

This chapter will discuss the origin of noise in mode-locked lasers with an emphasis on semiconductor mode-locked lasers. The effects of noise on communication system performance will also be discussed. I will restrict the discussion to amplitude and timing noise. Lasers also exhibit fluctuations in optical frequency and optical phase, but these will thus not be treated here. Some caution should be taken when speaking of phase-noise in order not to get confused by terminology. One of the most used methods for measuring the timing noise of mode-locked lasers is the so-called phase-noise method (which will be treated in section 2.2). The method does not measure the optical carrier phase-noise of the laser. The name stems from microwave notation where timing fluctuations are referred to as phase-noise.

2.1 Physical origin

Generally, noise in lasers can be either inherent (caused by physical phenomena in the laser itself) or technical, i.e. transferred from the driving electronics (DC-current supply or high-frequency oscillator). Fluctuating ambient conditions such as the temperature or vibrating mirrors can also cause noise in lasers, but these have a minor impact on compact monolithic semiconductor lasers and will not be considered here. All lasers exhibit noise in the form of spontaneous emission. Diode lasers also exhibit significant noise due to carrier density fluctuations, which change both the gain and refractive index. These carrier fluctuations are driven by carrier shot-noise, but also by technical noise sources such as DC-power supplies. Noise in diode MLLs is different from the noise in e.g. solid-state mode-locked lasers, because of the fast gain (carrier) dynamics [35]. The carrier life-time is very short (nanoseconds compared with microseconds for solid-state) for MLLDs and the effects of gain fluctuations on the timing is important on the time scale of the pulse round-trip time. The effects of the fast gain (carrier) dynamics on the timing noise are

1. The pulse interacts with the gain material on a time-scale of a few ps, draining more and more carriers as the intensity is increased. In this way the pulse saturates the local gain leading to more amplification of the front of pulse, which effectively moves the pulse forward.

2. Slow variations of the total gain leads to variations in (group) index (through the α-factor) and hence timing variations (cavity length fluctuates).

The effects of spontaneous emission on the timing stability are

1. spontaneous emission is projected directly into timing fluctuations: spontaneously emitted photons add energy to the pulse randomly in time making the pulse go back and forth relative to it's mean repetition rate

2. spontaneously emitted photons have random frequency, and frequency fluctuations in combination with dispersion (index vs. frequency) couple the spontaneous emission into timing fluctuations

Amplitude noise is of course directly related to spontaneous emission and gain variations. Active or hybrid MLLs will have technical noise transferred from the electrical high-frequency oscillator on top of the inherent laser noise. The technical noise usually dominates at low frequencies (<1MHz, see section 5.2.2 or [36, 37]). For the basic understanding of the laser itself and also from the point of view of the application this part of the noise is less relevant. The latter argument stems from the fact that noise within the bandwidth of clock-recovery circuits, usually in the MHz-range for standardised electrical clock-recovery (see table 5.2 or reference [38]) can be tracked and neglected. The integration bandwidth of noise will be discussed further in sections 2.3 and 5.2.2.

Now that we have defined noise sources and their effects on our pulses, we would like to find ways to minimise the sources and the effects of them. The total spontaneous emission noise level is directly proportional to the gain ($R_{sp} \propto n_{sp}g$)[1], which in turn is set by the total losses in the laser. Thus minimising the total losses are important [39]: low waveguide loss in combination with low mirror losses. However, since mode-locking introduces extra loss in the absorber, we should not only optimise the static linear losses but also the dynamic non-linear losses during mode-locking. Thus, the pulse must not be broadened too much in the gain section, to allow for little pulse shaping in the absorber (this will be discussed further in chapter 3). Spontaneous emission is also proportional to the population inversion factor, n_{sp}, determined by the inversion of the carriers. A high inversion or low population inversion factor is desireable in order to reduce the noise. This is done by having a symmetrical separation of the quasi-Fermi-levels, and by operating the laser close to the limit of the maximum gain at the band edge. Optical filtering, such as DBR-gratings, will reduce the amplified spontaneous emission outside the bandwidth of the filter [35]. The carrier noise should be reduced by using quiet current sources and lowering threshold current, which lowers the carrier shot noise (the slow noise of the current source will probably not matter for communication purposes as discussed in section 2.3). Threshold current is reduced by reducing losses but also by reducing non-radiative recombination, such as surface and Auger recombination. Finally one can reduce the noise between pulses by increasing the modulation to the absorber, e.g. by increasing the injected RF-power.

[1] $n_{sp} = \frac{f_2(1-f_1)}{f_2-f_1} = \frac{1}{1-e^{(E_{21}-\Delta E_F)/kT}}$ where f_2 and f_1 are the electron probabilities of the conduction and valance band. E_{21} is the lasing energy and ΔE_F is the quasi-Fermi level separation.

2.2 Mathematical models and theory

In the preceding section the sources of noise in diode mode-locked lasers were discussed. But we would also like to know how to quantify the noise from a given real laser through some sort of measurement and how to relate the measured noise quantity (e.g. timing jitter) to the different noise sources (e.g. spontaneous emission or carrier noise). To do so we need mathematical models and theoretical investigations to link the measured quantity to the noise source. To narrow the discussion somewhat we are only interested in amplitude and timing noise and their sources. Furthermore, we are interested in diode lasers with short gain relaxation times and slow saturable absorbers. Figure 2.1 presents a pulse train with the two distortions that we are interested in.

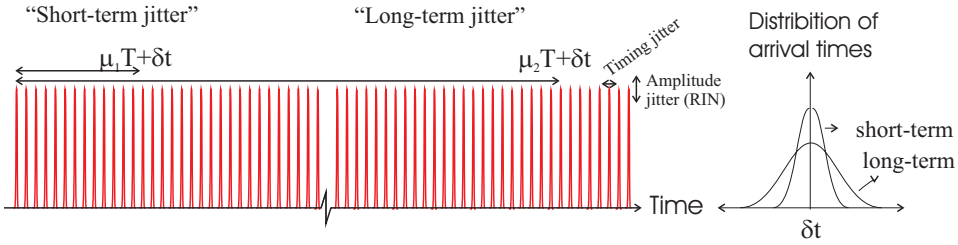

Figure 2.1: Pulse train with amplitude and timing jitter. The distribution of the timing noise is dependent on the measurement interval.

A phenomenological model of timing and amplitude noise was presented by von der Linde in 1986 for mode-locked lasers with active retiming [40]. By analysing the spectral content of the intensity power spectrum of the photocurrent he could calculate root-mean-square values of both amplitude and timing noise (assuming they were uncorrelated). By this method von der Linde could measure timing and amplitude noise quantitatively with great accuracy. However, with no coupling to physical noise sources, such as spontaneous emission. Since the "von der Linde method" is the base for a large part of the measurement load during this project, I will give a short summary of it below. A perfect pulse train can be described by

$$F_0(t) = \sum_{\mu} f(t + \mu T_R) \tag{2.1}$$

Where $f(t)$ is an unknown function describing the pulse shape, μ an integer running from minus to plus infinity and T_R is the repetition time of the pulse train. Adding random and uncorrelated amplitude and timing fluctuations, A and J, the noisy pulse train is given by

$$F(t) = (1 + A(t))F_0(t + T_R J(t)) \tag{2.2}$$

with A and J expressing small relative deviations from F_0 in amplitude and time. The fluctuations are assumed to be slowly varying compared to the pulse intensity $f(t)$, i.e. the pulse shape is constant. A and J have zero mean, and variances defined by the time-averaged square-mean

$$\sigma_A^2 = \left\langle |A|^2 \right\rangle E^2 \tag{2.3}$$

$$\sigma_J^2 = \left\langle |J|^2 \right\rangle T_R^2 \tag{2.4}$$

where E is the average energy of the pulse train. Taylor expanding F_0 around t gives (neglecting $A \cdot J \cdot T_R \cdot F_0$)

$$F(t) = F_0(t) + F_0(t)A(t) + \dot{F}(t)T_R J(t)) \tag{2.5}$$

The time-averaged noise and the noise power spectra (von der Linde used P to denote the power spectrum, I will use S here, which seems to be more the more popular alternative) are related according to Parseval's theorem

$$\left\langle |X|^2 \right\rangle \equiv \lim_{T\to\infty} \frac{1}{T} \int_{-\infty}^{\infty} |X(t)|^2 \, dt = \int_{-\infty}^{\infty} S_X(\omega) d\omega \tag{2.6}$$

What we can measure is the power spectrum of the noisy pulse train, $F(t)$, and hope to be able to sort out S_{X}. The power spectrum is given by the Fourier transform of the autocorrelation of $F(t)$. The details of the mathematics can be obtained from [40], while the result is given here (assuming that the fluctuations in amplitude and timing are slow compared with the pulse intensity, f(t), and are random)

$$S_F = \left(\frac{2\pi}{T_R}\right)^2 \left|\tilde{f}(\omega)\right|^2 \sum_{\mu=-\infty}^{\infty} [\delta(\omega_\mu) + S_A(\omega_\mu) + (2\pi\mu)^2 S(\omega_\mu)] \tag{2.7}$$

where the summation is taken over the integer μ from minus to plus infinity, and $\omega_\mu = \omega - 2\pi\mu/T_R$. This means that the power spectrum of the laser intensity can be decomposed into the contributions from the perfect pulse train (delta functions around the repetition frequency and its harmonics), the power spectrum of the relative amplitude noise and the power spectrum of the relative timing noise. The envelope of the total spectrum is given by the Fourier transform of the perfect pulse train, i.e. the pulse width determines the envelope (which is slowly varying compared to the functions inside the summation). At $\mu = 0$ the spectrum is composed of only amplitude noise, while the timing noise has a square dependence on μ. The μ-dependence allow us to separate the two contributions. At baseband the area of the noise spectrum is directly related to the RMS amplitude noise by

$$\sigma_A^2 = \int_{-\infty}^{\infty} S_A(\omega) d\omega \tag{2.8}$$

while the RMS timing jitter is related to the area of the higher harmonics

$$\sigma_J^2 = T_R^2 \int_{-\infty}^{\infty} S_J(\omega) d\omega \tag{2.9}$$

The "von der Linde method" is popular since it's relatively simple to perform and can measure low noise fluctuations. In chapter 5 we will use it to evaluate the timing jitter in a number of different lasers. However, as stated earlier, the method in itself does not explain any particular shape of the noise distribution or how the level of the noise depends on the noise sources.

Analytical theories An analytical model of timing jitter in actively mode-locked lasers was presented by Hjelme and Mickelson in 1992 [36], including spontaneous emission, RF-modulator noise and the effect of cavity detuning (mismatch of the modulation frequency and the round-trip frequency) as noise sources. Considering that we are interested in semiconductor MLLs with mostly passive mode-locking, this model has a few limitations: saturable absorption and fast gain variations were not included in the model, and Gausssian pulses was assumed. However, qualitatively the analysis had some important points: 1) the importance of spontaneous emission, 2) all noise sources were filtered by a Lorentzian with a characteristic cut-off frequency given by γ/N^2, where γ is the modulation strength and N the number of locked modes, 3) the importance of cavity detuning and 4) the influence of the RF-generator phase noise which is uncorrelated with the other noise sources. Expressions for the total timing jitter spectral density, S_J, and RMS timing jitter, σ_J (not given here), as a function of the Shawlow-Townes linewidth ($\Delta\omega_{ST} = \frac{R}{2P}$, spontaneous emission/number of stimulated photons), the modulation frequency (ω_m), the cavity detuning ($\Delta\omega$), the number of locked modes (N), the modulation strength (γ) and the RF phase noise ($S_\phi(\omega)$), was given as main results

$$S_J(\omega) = \frac{2\sqrt{2}\Delta\omega_{ST}}{\omega_m^2 N(\gamma/N^2)} \frac{(\gamma/N^2)^2}{\omega^2 + (\gamma/N^2)^2} \cdot$$

$$\left\{ 1 + \frac{N^2}{2} \left(\frac{\Delta\omega}{\gamma/N^2} \right)^2 \frac{2(\gamma/N^2)^2}{\omega^2 + (\gamma/N^2)^2} + \frac{\gamma/N^2 S_\phi(\omega)}{2\sqrt{2}\Delta\omega_{ST}} \right\} \tag{2.10}$$

A good approximation of the phase noise of a typical RF-oscillator is given by [36]

$$S_\phi(\Omega) = S_0 \left[\left(\frac{\Omega_{c0}}{\Omega} \right)^\beta + 1 \right] \frac{\Omega_{c1}^2}{\Omega^2 + \Omega_{c1}^2} \tag{2.11}$$

Typical values of S_0, Ω_{c0}, Ω_{c1}^2 *and* β are (-60-100 dBc/Hz, 100-1000 Hz, 2-100 kHz, and 1-3) for synthesizers, and the contribution from the synthesizer can be neglected after 10-100 kHz, since it falls off as Ω^4. However integrating for very long times, i.e. to low frequencies, means that the mode-locker will add significantly, because of the $\Omega^{-\beta}$-variation of the phase noise. If detuning exists the white noise plateau (see figure 2.2), will be increased and the initial roll-off higher than 20 dB/decade, see figure2.2. The detuning will have an effect on the total noise spectrum if $\Delta\omega > \frac{\sqrt{2}}{N}(\gamma/N^2)$. For a cut-off frequency of 100 MHz (typical of the lasers characterises in this project, the detuning needs only to be 3 MHz if we assume 50 locked modes. Such increased roll-off slopes have been measured experimentally [99] and section 5.2.2.3.

In 1993 Haus and Mecozzi presented an analytical theory of the noise in passive MLLs with soliton shaped pulses (and with slow gain variations), thus taking into account saturable absorption [41]. Both classical and quantum mechanical noise sources were considered (gain, refractive index and spontaneous emission). They derived the power spectra for amplitude and timing fluctuations. The mean square timing jitter (variance) of a passively mode-locked laser was found to undergo a random walk vs. time (linear divergence). It is unbounded in the absence of a restoring modulation. This translates into a spectral density, $S_J(f) = \frac{2D^2}{f^2}$ for long times, where D is a diffusion constant proportional to group velocity dispersion,

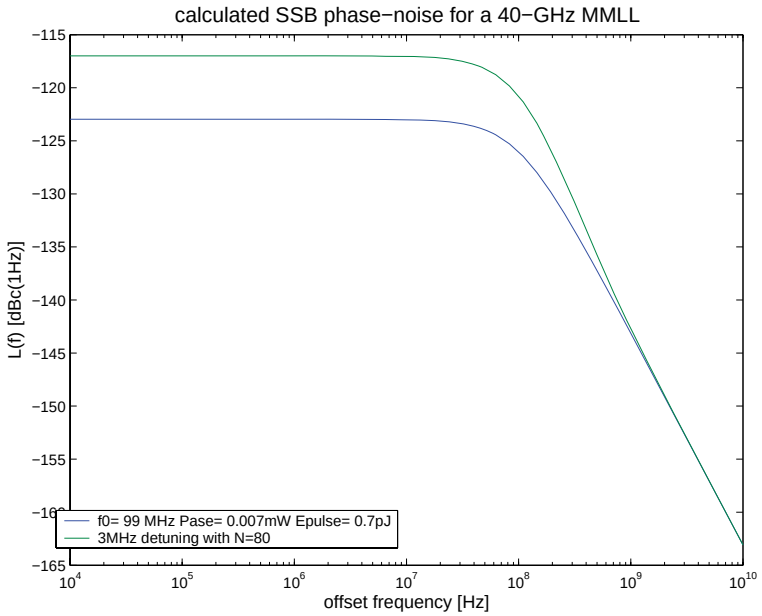

Figure 2.2: Normalised timing jitter spectral density calculated from equation 2.10. $S_J(f) = \frac{1}{\omega_m^2}\mathcal{L}(f)$ where $\mathcal{L}(f)$ is the single-sided phase-noise spectrum defined in section 5.2.2.

the inversion factor and the gain, and inversely proportional to the pulse energy squared, the roundtrip-time of the cavity and the pulse width. The second order roll-off corresponds well to the measured passive phase-noise spectra in chapter 5 (and also to other experimental spectra). Once again the importance of the inversion and gain is pinpointed.

Furthermore they compared the results to the method of von der Linde. A good agreement was found under the assumption of a restoring force (active modulation on top of the saturable absorption). However, it was shown that Lindes formula was inaccurate for pure passive mode-locking at low frequencies, because of the first-order expansion in time that he had made. The absence of delta functions at the fundamental and harmonics of the repetition frequency limits the frequency range for accurate measurements of passive mode-locking. The von der Linde method is valid for passive mode-locked lasers down to a frequency when $\sigma_J^2\mu^2(2\pi/T_R)^2 \approx 1$. If $T_R = 100$ (25) ps, then the RMS timing jitter must not be larger than 16 (4) ps when integrated from infinity (zero time) over the first harmonic of the photocurrent spectrum. We should keep this in mind when evaluating the timing jitter for passive mode-locked lasers in chapter 5.

Finally we shall look at the what is special for semiconductor mode-locked lasers. The most extensive noise theory for semiconductor mode-locked lasers can most probably be found in [35] and [27]: analytical expressions are given for all fluctuations concerning the output field of a semiconductor mode-locked laser (energy, carrier phase, frequency and timing) with a coupling to physical noise sources. Saturable absorption and active modulation are considered (inclusive the phase noise of the RF-synthesizer) as well as gain with a fast saturation and relaxation time.

This was the first time a noise theory for MLLs included fast gain. The analysis is based on the same master equation and perturbation theory as the paper by Haus and Mecozzi. In appendix B in [27] expressions for the amplitude and timing noise spectra of a MLL are given, considering the above mentioned physical effects. The expression for the single-sideband phase noise, $L(\omega)$ (L is defined in section 5.2.2, and is related to the timing noise through $S_J = L/(\omega_m)^2$, with ω_m being the modulation frequency), from a mode-locked laser with saturable absorption and modulation, but with only slow gain relaxation, is given by [27, p. 204]

$$L(\omega) = \left(\frac{2\pi}{T_M}\right)^2 \frac{\tau^2 P_{ASE}}{2\pi A_0^2} \frac{1}{\omega^2 + (2\gamma_0^{\Re})^2} \tag{2.12}$$

In principle the same result as equation 2.10. Where $\mathrm{T_M}$ is the modulation time, τ is the pulse width, $\mathrm{P_{ASE}}$ is the amplified spontaneous emission power, A_0^2 is the pulse energy and the cut-off frequency $\gamma_0^{\Re} = M_{AM}\omega_M^2\tau^2/4T_R$ is affected by the strength of the modulation, M_{AM}, the pulse width, τ, the modulation frequency, ω_M, and the round-trip time of the cavity, T_R. The influence of the modulation strength on the white noise level and the cut-off frequency has been measured by Jiang with perfect agreement to the theory. The influence of the modulation frequency relative to the round-trip frequency has been experimentally verified by Yilmaz et al. [42].

Adding fast gain saturation to the model, it is concluded that fast gain saturation converts amplitude fluctuations into timing fluctuations which add a significant term. The final SSB noise is given by [27, p. 213]

$$L_{fgs}(\omega) = \left(\frac{2\pi}{T_M}\right)^2 \frac{2\tau^2}{A_0^2} \frac{1}{\omega^2 + (2\gamma_0^{\Re})^2} \left[\frac{P_{ASE}}{4\pi} + 0.16(\omega_R)^2\tau^2 T_R^2 \frac{1}{A_0^2} S_A(\omega)\right] \tag{2.13}$$

where $\mathrm{S_A}$ is the amplitude noise power spectrum and ω_R is the relaxation resonance frequency of the carrier-photon system. The amplitude noise power spectrum is also a Lorentzian with a pole at the relaxation oscillation frequency. The amplitude noise spectrum or relative intensity noise (RIN) spectrum can be approximated by [69, ch. 5]

$$S_A(\omega) = \frac{2h\nu}{P_{ave}} + 8(\Delta\omega)_{ST} \frac{1/\tau_{\Delta N}^2 + \omega^2}{\omega_R^4} |H(\omega)|^2 \tag{2.14}$$

for moderate average output powers $\mathrm{P_{ave}}$. $H(\omega) = \omega_R^2/(\omega_R^2 - \omega^2 + j\omega\gamma)$ is the modulation transfer function, γ the damping factor, and $\tau_{\Delta N}$ is the differential carrier lifetime. Thus the contribution from the fast gain relaxation will roll off as $1/\omega^4$ after the relaxation oscillation frequency. For laser media with a slow gain the relaxation oscillation frequency will be low leading to a smaller prefactor and an earlier roll-off. However for diode lasers the amplitude noise contribution to the timing noise can be significant around the natural frequency of the laser, which typically is several GHz. The phase noise of the mode-locker (RF-synthesizer), S_ϕ, also adds to the final phase noise of the power spectrum of the laser, but this was treated earlier (see equation 2.10).

2.3 Consequences of noise for optical fibre communications

This section will discuss the consequences of amplitude and timing noise. Lasers also have noise in frequency and phase (the phase of the electric field inside the pulse envelope) but these quantities will not be discussed, since 1) the frequency and phase information is lost when detecting the pulse train with a photodiode and 2) although such fluctuations can couple to amplitude and timing fluctuations they are believed to be of less significance when it comes to degrading performance in long-haul high-speed communication systems (timing jitter transfered from frequency jitter by the dispersion of fibres will for example be reduced by dispersion compensation).

Amplitude noise Amplitude noise directly degrades the Signal-to-Noise Ratio (SNR) of a bit stream which converts to bit errors at the detection (receiver) if the noise is high enough. The SNR is one of the parameters that limits the transmission distance. The electrical SNR for a RZ-pulse train is

$$SNR = \frac{P_{ave}^2}{\langle \sigma_A^2 \rangle} \tag{2.15}$$

where P_{ave} is the optical average power and σ_A is the time averaged root-mean-square fluctuation of the amplitude. However, since the SNR depends on the integration range (measurement time) of the noise, laser engineers usually use a bandwidth independent figure-of-merit, Relative Intensity Noise (RIN), to compare the performance of their lasers. RIN is defined as the ratio of the amplitude noise power per Hz and the squared average optical power (how to measure RIN in practice will be presented in chapter 5).

$$RIN = \frac{\langle \sigma_A^2 \rangle |1Hz}{P_{ave}^2} = \frac{S_{\Delta P} \Delta f (= 1Hz)}{P_{ave}^2} \tag{2.16}$$

As can be seen from equation 2.16, the RIN is related to the spectral density of the amplitude fluctuations, $S_{\Delta P}$, which can be derived from the baseband power spectrum of the laser intensity as described by the "von der Linde-method" in the preceding section. Although RIN in dB/Hz is a nice comparing tool for lasers, real receivers in optical communication systems average the noise over their finite bandwidth. So for such an application it's probably more interesting to know the RMS amplitude noise, integrated over a certain receiver's effective noise bandwidth, in percent of the average power. The best way to find the requirements for the amplitude noise for a certain system with a certain laser, is to perform Bit-Error-Rate (BER) measurements at the same time as the amplitude noise for the output of the laser is varied by some means. The difficulty in calculating a theoretical level lies in the fact that the effects of the laser noise in the receiver are affected by the transmission. However to make life a little easier we can make an approximate calculation of the required amplitude noise for a given BER.

Receiver degradation due to amplitude noise can be described by the so-called power penalty: the required increase in received power, compared to a noiseless input, to maintain a certain (low) BER. The required value of the maximum al-

lowable RIN for a certain allowable power penalty can be calculated from [7, p. 179]

$$\delta_I = -10log_{10}(1 - r_I^2 Q^2) \tag{2.17}$$

assuming Gaussian noise distribution and a decision level at half the 1-level. δ_I is the power penalty in decibels, and Q the Q-value (Q = 5.98 for a BER = 10^{-9} for Gaussian noise). $r_I^2 = RIN(dB/Hz) \cdot B_e$ where B_e is the effective noise bandwidth of the receiver. With a power penalty of 1 dB the allowable RMS amplitude fluctuation from our laser should should be less than 7.7 % of the average power, to achieve BER<10^{-9}. This is the allowable amplitude noise in the detector. To find the allowable noise in the laser, we must know the effects of the system (but we can be sure that the RIN of the laser must be lower). Table 2.1 lists required maximum RIN in dB/Hz vs. B_e, calculated with equation 2.17.

Table 2.1: Requirements on maximum RIN to achieve BER < 10^{-9} (assuming Gaussian noise distribution) with a maximum penalty of 1 dB (i.e. 7.7 % total RMS noise), for different receiver bandwidths according to equation 2.17. The receiver bandwidth is taken to be 0.5*Base rate [12].

Base rate (GHz)	Receiver bandwidth (GHz)	RIN (dB/Hz)
10	5	-119.4
40	20	-125.4
80	40	-128.4
160	80	-131.4

Timing noise Timing noise affects all signal processing where a decision of time has to be taken, i.e. whenever clock-recovery (CR) is necessary. In OTDM-systems that's basically every operation except generation and amplification, e.g. switching, detection or retiming. Ideally the switching or detection should be done at the time of maximum pulse intensity. Timing noise degrades receiver sensitivity, giving rise to bit-errors. In the worst case, timing jitter is so large that neighbouring bits begin to overlap.

Timing noise is relative! When using CR (e.g for demultiplexing) it's the jitter of the pulses relative to the recovered clock that is important. The decision instant for sampling or switching of the pulse is determined by the CR-circuit. The recovered clock is determined from the average of a certain length of the noisy data train. The best case is when all bits are ones. As mentioned in section 1.2 the clock-recovery can be accomplished by several techniques (e.g. with a phase-locked-loop or all-optically). Common to all the techniques is that they act as low pass filters, where slow variations are followed but fast variations are not. In case of the PLL-technique the low-pass filter after the phase comparator, determines the number of pulses over which the clock is defined. If the low-pass filter has a bandwidth B, then slower variations in timing will be followed by the CR-circuit, and we can neglect these. The bandwidth B depends on the type of circuit used. ITU-T standardised bandwidths for electrical CR are 1 MHz and 4 MHz for 10 GHz and 40 GHz bit rate

respectively [38]. All-optical fibre based CR, usually use long lengths of fibre for the phase comparator (e.g. in a Non-linear Loop-Mirror, NOLM) and thus have low B, down to 100 Hz (which isn't desireable). Using optoelectronic semiconductors as phase comparators in so-called optical PLLs (OPLLs), one can reduce the loop length and increase the bandwidth. Ideally the whole circuit should be integrated on a single semiconductor chip, but a hybrid optoelectronic phase-locked loop consisting of separate semiconductor components and fibre has produced a locking bandwidth of 300 kHz [14]. The influence of fibre delay and loop-bandwidth on the performance of the demultiplexed jitter has been investigated in [44]. Using injection-locked MMLLs as clock-recovery devices (both optical clock and electrical clock can be retrieved), they should be able to follow the timing noise up to the cut-off frequency of the timing noise spectrum as defined in equation 2.12. Measured values of semiconductor cut-off frequencies varies between 1 MHz [37] and several hundred MHz (see figure 5.28). It should be noted that it's not a good idea to increase this bandwidth indefinitely. Increasing the bandwidth to the GHz-range would mean that the CR would start to follow the individual bits in the data pulse train.

The tolerance toward timing jitter between the recovered clock and the data (integrated for frequency offsets greater than B) has been studied theoretically and experimentally for all-optical demultiplexing using a nonlinear fibre Sagnac interferometer switch in [12] and using a NOLM in [45]. Assuming a square switching window equal to the width of the time slot, it was found that the jitter should not exceed 8 % of the time slot at the specific line rate of the OTDM-system in order to achieve a BER$<10^{-9}$.

Table 2.2: Allowable timing jitter vs. aggregate bit rate for error-free (10^{-9}) all-optical demultiplexing. Pulse width is assumed to be 1/5 the time slot and switching window equals the time slot. After reference [12].

Line bit rate (GHz)	Time slot (ps)	Switch window (ps)	Pulse width (ps)	Timing jitter (ps)
40	25	25	5	2.1
80	12.5	12.5	2.5	1.04
160	6.25	6.25	1.25	0.52
320	3.13	3.13	0.62	0.26
640	1.56	1.56	0.31	0.13

Chapter 3

Design of low-noise monolithic MLLs with intracavity filter

3.1 Active material design

In chapter 2 it was discussed how to lower the noise in mode-locked lasers in terms of lowering the noise sources. When growing a laser structure however one does not specify noise sources but material composition and thickness. This section will discuss the used laser structures and how low noise is achieved. The design goal is to achieve at the same time pulses a few picoseconds long, with high power and low noise. In order not to get lost in too many special cases, I will limit the discussion to absorption modulated all-active lasers with long cavities (1-4 mm, or 10-40 GHz rate). Quantum wells (QWs) or quantum dots (QDs) are assumed for the gain material since they invert more easily and allow a larger design freedom, such as incorporating strain. The two most important factors in this context is the saturation energy of the active material and the waveguide loss. It is desireable with a high saturation energy in the gain section because it lowers the pulse broadening, leading to less pulse carving in the absorber. The pulse saturation energy is defined as [46]

$$E_{sat} = \frac{h\nu A}{\Gamma \frac{dg}{dN}} \tag{3.1}$$

where $h\nu$ is the photon energy, A the area of the quantum wells, and $\Gamma \frac{dg}{dN}$ the modal differential gain. The gain for a pulse above this energy will be significantly reduced. To increase the saturation energy we should decrease the modal differential gain. The most popular way to achieve both a high saturation energy and a low loss has been to make an external [47] or extended cavity laser [48], in which part of the laser is made passive by regrowth or some quantum well intermixing technique. With an extended cavity more gain per length is needed in the short gain section and since the differential gain is reduced as the gain increases, this results in a higher saturation energy. The passive waveguide also provides lower loss than the active waveguide. However, it is possible to achieve a high saturation energy and low loss at the same time in all-active lasers too. By decreasing the number of QWs the confinement factor, the differential gain and the loss will fall. Using QDs would

have the same effect. Using thick undoped waveguide material is also paramount for achieving low loss. The idea to lower the saturation energy by using fewer wells was first proposed by Yvind in [39]. Since then these ideas have been corroborated by a number of recent papers on 10- and 40-GHz lasers [49, 50, 51].

3.2 Intracavity filter design

3.2.1 The needs

The advantages of an intracavity filter in a mode-locked laser are many. Such a filter will cut away amplified spontaneous emission noise outside its bandwidth. This was pinpointed in chapter 2 as important for achieving ultra-low noise performance (also see references: [30, 35, 39]). It also prevents fluctuations from frequency-pulling [41].

Well defined optical spectrum With a filter, the wavelength of the laser can be controlled to a high degree by controlling design parameters of the filter instead of being dependent of the calibration of the growth vs. PL-emission, and the laser driving conditions, such as gain current and absorber bias. This is very important for optical communication systems: firstly the bandwidth of today's systems are limited to the 30 nm window of EDFAs (~1530-1560 nm) and secondly the channel spacing in a pulsed WDM system would also put restrictions to the tolerable wavelength deviations.

A badly shaped spectrum, like the spectrum in figure 3.1 (obtained from a Fabry-Pérot laser), will be difficult to use as a source for long distance communication. If a combination of OTDM and WDM is used the wings of the spectra of different wavelength channels might overlap. With an intracavity filter the shape of the spectrum can be made to be close to a Gaussian, see figure 3.2. This means that the spectrum falls off quickly, which reduces the risk of channel cross-talk. Moreover, it's difficult to calculate a FWHM width of a badly behaved spectrum. Or even worse the FWHM width might not be relevant because of all the optical power far from the centre wavelength [33].

Well defined repetition frequency OTDM-systems operate at predefined fixed repetition rates and MLLs must be able to meet these fixed rates. However, the cleaving accuracy of a semiconductor laser is not better than $\pm 5\mu m$ at best (this is an estimation of our own cleaving accuracy; other sources have reported similar accuracies, like [52]). A cleaving error of $10\mu m$, corresponds to 25 MHz at 10 GHz (400 MHz at 40 GHz). The tuning possibilities of a Fabry Pérot laser, schematically drawn in figure 3.3a), are very limited. About 30 MHz for a 10 GHz laser by tuning by both temperature and current injection can be achieved with the laser material used in this project. A MMLL with both mirrors defined by lithography could be made by making a high-reflectivity DBR at the absorber end. Such reflectors have been made by etching through the entire waveguide structure of a ridge laser with very good results [53, 54]. This would require an extra masking and an extra etching step in the processing of the laser, but should be feasible.

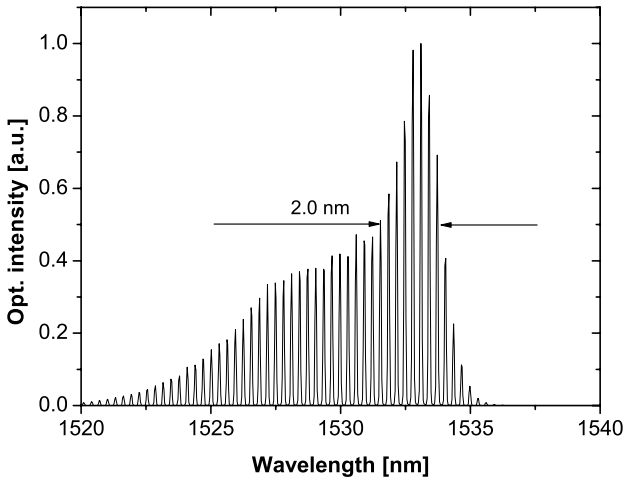

Figure 3.1: Mode-locked spectrum of a 40 GHz FP-laser with epitaxial structure SCOOP6 (see section 4.1). The FWHM spectral width is 2.0 nm.

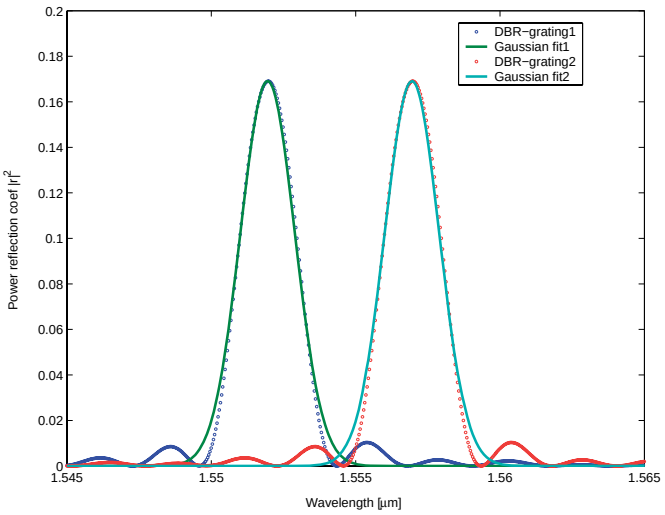

Figure 3.2: Reflectivity (optical spectrum) of 2 DBR-gratings with Bragg wavelengths at 1552 and 1557 nm, together with Gaussian fits. The FWHM spectral widths are 2.3 nm for both.

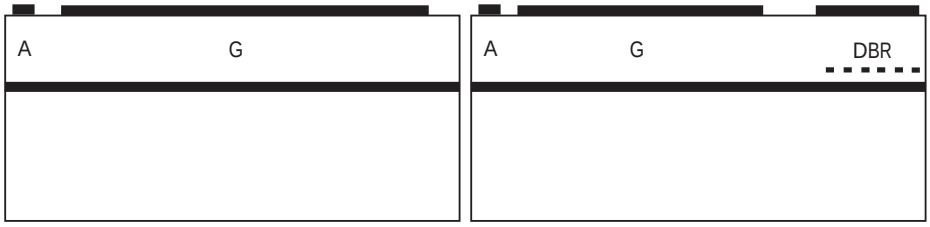

(a) FP-type MMLL (b) DBR-type MMLL

Figure 3.3: Two types of monolithic semiconductor lasers: a) FP-type & b) DBR-type. A is absorber section, and G is gain section. The black rectangle running through the whole structure represents the waveguide, while the black rectangles on top of the structures represents the contacts of different sections.

Tuneable repetition frequency Several papers report on an enhanced repetition rate tuning for Distributed Bragg Reflector MMLLs, see figure 3.3b) for a schematic drawing. For passive mode-locking 1 GHz is the widest range reported [55]. The large tuning range was accomplished by 4 different tuning schemes: phase section current, gain section current, absorber voltage and local thermal tuning of the DBR. Increase in repetition rate tuning during hybrid mode-locking has also been reported: 800 MHz has been achieved for a 40-GHz laser by varying the current through a passive phase section [56]. 3 GHz tuning with very small simultaneous wavelength tuning (1 nm/GHz) by the use of chirped gratings has been reported by [57] in a 40-GHz laser. The effective length of the DBR was tailored such that it was linearly varying over the DBR-peak, which compensated for chirp in the gain and absorber sections.

Tuneable wavelength Finally it should also be possible to tune the optical frequency (wavelength) by heating or with the plasma effect of injecting carriers into a DBR-section [51, 52, 55, 58]. The reported values of such wavelength tuning are quite small in most cases (4-6 nm) for MMLLs. 12 nm has been achieved by local thermal heating of the DBR [55]. Truly wide tuning has been achieved (20 nm in [59] and 40 nm in [60]), when more widely tuneable filters have been incorporated but with structures without saturable absorbers. In the case of the widely tunable lasers the pulse width was 10-15 ps, due to the lack of a saturable absorber.

3.2.2 Choosing filter type

Filters in optically active semiconductor material have been around for a while now. The filters that will be discussed here and later in this thesis are all bandpass filters (or band reflecting), i.e. selecting (through transmission or reflection) a narrow part of the optical spectrum. Contradirectional (reflecting) filters of Bragg type (see a schematic drawing is shown in figure 3.4b) in InP or GaAs were developed already in the 80's for use in DFB or DBR lasers. These filters were mostly made narrow enough for selecting just one longitudinal mode. Co-directional or transmissive filters of coupler type were popular in the 90's because of their large tuneability (see figure 3.4a). They were used for widely tuneable receivers [61] and widely tuneable

lasers [62]. Even wider tuning range can be achieved by combining couplers and Bragg filters [63] (114 nm). The research on widely tuneable lasers during the 90's led to many new designs and realisations of monolithic filters and combinations of them: the Sampled Grating DBR (SGDBR), the Grating-assisted codirectional Coupler with Sampled rear Reflector (GCSR) and the Y-laser, to mention a few.

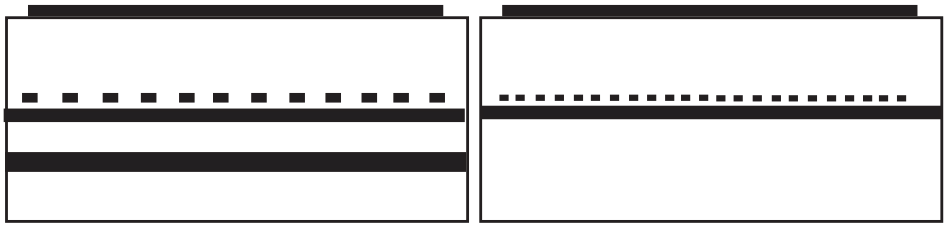

(a) Coupler (b) DBR

Figure 3.4: Schematics of Grating-Assisted Coupler (GAC) and Distributed Bragg Reflector (DBR) filters.

A mode-locked laser is per definition a multi-mode laser and thus a filter for such a laser should be wide enough to incorporate several modes. Already in 1980 Ippen et al. experimentally investigated the effects of an intracavity bandwidth limiting element [64] (in an external configuration). They came to the conclusion that not only did the time-bandwidth product improve, but the pulse width could also improve from the case without the bandwidth limitation. When the bandwidth became too narrow the pulses broadened again as expected. The pulse narrowing effect can partly be attributed to less spontaneous emission noise. Both DBR and coupler filters can be made with a proper bandwidth for multi-GHz mode separation.

A 5.5 mm long regrown extended cavity laser with a DBR was the first monolithic laser, to my knowledge, which incorporated internal spectral filtering [65]. Active modulation of a long gain section and a long DBR with a narrow spectrum were the reasons for the long pulses of 20 ps. The same group made one of the other earliest reports on a mode-locked laser incorporating an integrated filter. But this time with a Grating-Assisted Coupler [59]. Pulses around 12 ps at a repetition rate of 15.8 GHz were reported with a time bandwidth product of 0.6-1.4. Mode-locking was achieved by active modulation of the gain section. The bandwidth of the filter was 3 nm. This was the first and only report of a mode-locked laser incorporating a Grating-assisted Coupler (GAC) filter, to my knowledge. This might be a little surprising since if wide tuneability is wanted the coupler is clearly to prefer. The complex fabrication is probably the explanation. The laser in [59] was not developed for mode-locking in the first place but as a widely tunable single mode CW laser, see reference [62].

Instead numerous groups have reported mode-locking with a DBR as filtering element. Their main purpose with the DBR are in most cases the same: achieving a repetition frequency tuning that can compensate cleaving errors by increasing the locking bandwidth to the synchronising RF-oscillator. The locking bandwidth is the frequency range with tolerable degradation.

The requirements for such a filter in combination with a mode-locked laser might in some cases be slightly different from those of a filter which is part of a

widely tuneable laser which is by far the most frequent application for these two filters. Thus the advantages and drawbacks might also be somewhat different.

3.2.2.1 Requirements for a mode-locked laser filter

Bandwidth The exact requirement on the bandwidth depends on how short pulses we expect. The transform limited spectrum of a 1 ps pulse is 3.5 nm with an assumed Gaussian pulse and spectral shape. The DBR and GAC filters are band-pass wavelength filters. In a mode-locking state, the filters are not single-pass. The pulse passes through the filter many times so that the spectral bandwidth must be larger than the transform-limited value. In a DBR, a high reflection results in more filtering than a low reflecting filter with the same single-pass bandwidth. In [66], a filter width of 4 nm gave an optical spectral width of 0.9 nm when the laser was mode-locked. From our measurements on our FP mode-locked lasers we achieve pulse widths down to one picosecond. It is therefore natural to try to obtain a bandwidth that can tolerate such short pulses. A bandwidth of 5-10 nm is probably a good starting point.

Reflectivity The required reflectivity depends on the gain and loss in the laser. From our earlier results on FP-lasers a 5 % AR-coating was advantageous for our 10 GHz lasers while the as-cleaved facet reflection (∼30 %) was suitable for 40 GHz operation.

Loss A low loss is desired for the grating. In our all-active structure the loss can be changed with current injection (plasma effect) or by voltage change (quantum confined Stark effect). The loss can also be influenced by the choice of centre wavelength of the filter as in [71], where the loss was lowered by detuning the Bragg wavelength of the DBR to the longer wavelength side of the gain peak of the active material.

Repetition rate tuning To compensate for cleaving errors, a tuning, $\Delta\nu_{rep}$, of 0.5-2.0 % of the repetition frequency, ν_{rep}, is needed dependent on the cleaving accuracy of the cleaved mirror, ΔL, and the variation in group index, Δn_g, due to growth and processing, see equation 3.2 and 3.3.

$$\Delta\nu_{rep} = \frac{\partial\nu}{\partial L}\Delta L + \frac{\partial\nu}{\partial n_g}\Delta n_g = -\frac{c}{2n_g L}\left(\frac{\Delta L}{L} + \frac{\Delta n_g}{n_g}\right) = \nu_{rep}\left(\frac{\Delta L}{L} + \frac{\Delta n_g}{n_g}\right) \quad (3.2)$$

$$\frac{\Delta\nu_{rep}}{\nu_{rep}} = \left(\frac{\Delta L}{L} + \frac{\Delta n_g}{n_g}\right) \quad (3.3)$$

The tuning in repetition rate should be done with as low simultaneous change in optical frequency as possible. Sometimes one speaks of the locking range (bandwidth). It's a frequency tuning range within which the mode-locked laser can lock to an electrical or optical modulation without degrading the performance substantially.

Wavelength Tuning A tuning range of 30 nm matching the C-band EDFA-window would be ideal, but is probably unrealistic without degrading more important functionalities such as short pulses and low jitter. But a range capable of compensating for variations in the Bragg wavelength,$\Delta\lambda_B$, originating in effective index variations, Δn_{ave}, and grating period variations, $\Delta\Lambda$, equation 3.4, is a minimum.

$$\Delta\lambda_B = \frac{\partial\lambda_B}{\partial n_{ave}}\Delta n_{ave} + \frac{\partial\lambda_B}{\partial\Lambda}\Delta\Lambda = 2\Lambda_0\Delta n_{ave} + 2n_{ave}\Delta\Lambda \tag{3.4}$$

3.2.2.2 Grating-assisted coupler vs. DBR

The coupler The major advantage of the GAC filter is its huge tuning potential, equation 3.5. Tuning ranges of more than 100 nm has been achieved with tuneable lasers [63]. The large tuning in a GAC is proportional to an index change relative to an index difference, instead of just the index change as in single waveguide tuning (e.g. DBR). As a comparison, the largest tuning range reported from an "ordinary" DBR is 15 nm [67]. However the bandwidth of the filter is of much higher importance than the tuning for a MMLL intended for telecommunication.

The tuning improvement factor for a GAC filter compared to a DBR filter is given by

$$F = \frac{n_g}{n_{g1} - n_{g2}} \tag{3.5}$$

where n_g is the average group index of the two waveguides and n_{g1} *and* n_{g2} are the group indexes of the two modes in the two waveguides. Since the denominator usually is quite small the improvement is large. The coupler bandwidth is given by

$$\Delta\lambda_{1/2} = 0.8\frac{\lambda_c^2}{L_{tot}(n_{g1} - n_{g2})} \tag{3.6}$$

where λ_c is the wavelength of the transmission peak of the coupler and L_{tot} is the total length of the grating. The bandwidth is thus dependent on the group index difference of the two modes in the two waveguides, which in turn depends on the differences in waveguide material composition and geometry. A bandwidth requirement of 5-10 nm for a MLL means that the group index difference must be 0.19-0.38 with a coupler length of 1 mm (0.1-0.2 if the coupler is made 2 mm long). Such a large change in dispersion cannot be achieved with geometry variations only (see Appendix A). The only reliable method to do this is to make a vertical coupler, in which the different materials are easily alternated and layer thickness is accurately controlled during the growth. To integrate the vertical coupler with other elements, such as amplifiers and absorbers, requires regrowth and many complex processing steps (or very complex semiconductor processing [61, 68]) and good butt coupling. The long length of the coupler compared to a DBR, is a clear disadvantage when making high-frequency mode-locked lasers. Making a 40-GHz MMLL with a coupler will be very difficult, even if a vertical coupler is used.

The DBR With a DBR it's usually easy to make a narrow filter, since the lower the index difference is, the narrower is the bandwidth, see figure 3.5 which plots the bandwidth of a third order grating against the index difference. For

index differences below 0.01 the bandwidth is only weakly dependent on the index difference. The bandwidth also gets narrower with longer gratings. So for the DBR-type filter it might in fact be harder to get a wide enough spectrum for a mode-locked laser with a picosecond pulse length and still have a reasonably high reflection. The amplitude of the reflection is directly proportional to the index difference (see equation A.7 in appendix A).

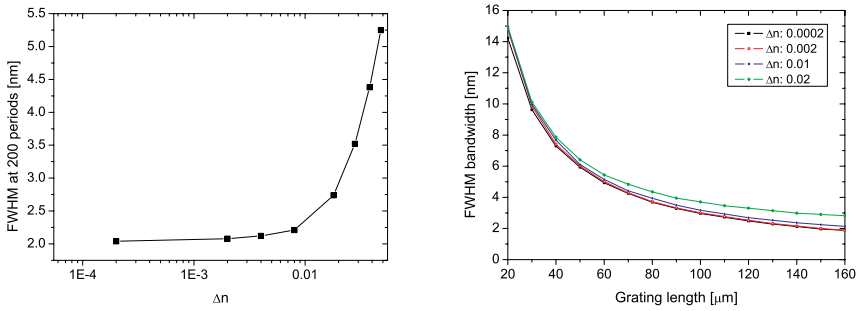

(a) (b)

Figure 3.5: Simulation (transmission matrix multiplication) of FWHM of a DBR vs. index difference. a) FWHM vs index difference, $L_{DBR} = 145\mu m$. b) FWHM vs. grating length for different index differences (grating strengths). Parameters used are: $\lambda_B = 1550nm$, 3$^{\text{rd}}$ order with 50 % duty cycle.

Also on the plus side for a DBR reflector is the straightforward fabrication. The only drawback is the necessity of an electron beam writer for the lithography because of the small grating period (typically submicrometer). Holographic methods also exist.

Compared to the GAC filter the tuning range of the DBR is the weakest point. It is tunable by the change of index in the grating, which can be controlled by carrier injection or temperature. The tunability is typically on the order of 0.1% of the wavelength [69], and is given by

$$\frac{\Delta\lambda}{\lambda_0} = \frac{\Delta n_{DBR}}{n_{DBR}} \tag{3.7}$$

where λ_0 is the untuned Bragg frequency, Δn_{DBR} is the induced index change and n_{DBR} is the average index in the grating.

We have chosen to realise a DBR filter based on the following: 1) It doesn't require regrowth (which wasn't available) and 2) the long length of the coupler filter makes it unsuitable in high repetition rate mode-locked lasers (short cavities).

3.2.2.3 Active vs. passive DBR material

Although the choice of a passive waveguide for DBR gratings (figure 3.6b), e.g. [63, 67] and many others, is far more common than the active waveguide (figure 3.6a), there are a few advantages of the latter [70]: 1) no extra processing that could decrease the yield is involved, 2) no regrowth is necessary which means that

it is possible to buy epitaxial material from a foundry (keeping the fabrication cost-effective), 3) no or very small reflection from the interface between different sections and 4) enhanced (current) tuning because the closer the photon energy is to the bandgap the stronger is the index change. The most serious disadvantage of the active configuration is the risk of high loss through absorption when injecting high concentrations of carriers for tuning. But this loss can be reduced by detuning the Bragg wavelength of the grating to a longer wavelength than the gain peak wavelength of the active material [71]. Also, since obtaining a large tuning range is not the most important requirement of the mode-locked laser grating, we could pump the grating at transparency and thereby avoid loss originating from absorption.

40-GHz MMLLs with passive bulk DBRs have been reported in [55, 72] with good results, while MMLLs with a DBR consisting of active material, with repetition rates of 20-160 GHz, have been reported in [52, 57, 66, 73]

There are ways to combine the advantages of both active and passive waveguides by changing the bandgap of the active material in parts of the wafer. One such method is Selective Area Growth (SAG), where the bandgap is changed during growth. The active regions of a wafer are masked by an SiO_2-pattern. The bandgap shifts locally due to the increased layer thickness by the enhanced growth rates of up to a factor of 2, induced by the SiO_2 [58]. MMLLs with a DBR made on passive QWs formed by SAG was reported in [18, 58]. A desirable feature with the QW-DBR is that it's possible to change the repetition rate by changing the loss, and thereby the effective length in the DBR by the quantum confined Stark effect [18].

Quantum Well Intermixing (QWI) has been a popular post-growth method for changing the bandgap of active quantum well waveguides. QWI can be done selectively on the part of the laser that is going to be the passive reflector. QWI can e.g. be done by proton implantation [74] or by laser ablation [75]. To my knowledge no MMLL with a DBR formed by QWI have been reported so far.

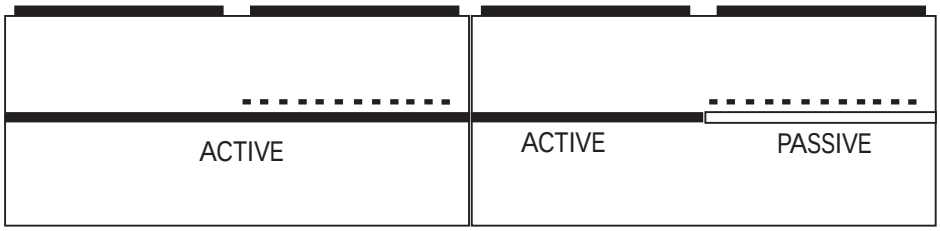

(a) Active (b) Passive

Figure 3.6: Schematics of a laser with a) an active DBR and b) a passive

3.2.2.4 Regrowth vs. post-growth processing of DBRs (deep etching)

The most common way to make a DBR-grating is to grow a thin grating layer on top of the waveguide, interrupt the growth, do lithography and a shallow etch in the grating layer (typically 50-100 nm). After cleaning, the wafer is put into the growth machine again and the laser structure is finished. MMLLs with this type of grating have been made by several groups as mentioned before, e.g. [18, 58, 66].

If regrowth is not wanted or not possible, the grating can be made by etching from the surface of the laser, see figure 3.7 and 3.8. To have a large overlap of the grating with the optical mode it is usually necessary to etch very deep into the structure. This deep etching is more difficult than the shallow etching because of mask erosion and high aspect ratios. It usually requires a careful optimisation of the etching. This is a clear drawback of the latter method. The first method also has drawbacks in processing. Surface preparation of the grating surface, in order to remove contamination from the grating fabrication, is extremely critical for a good overgrowth.

With the latter method it's possible to achieve larger index differences since one can fill the trenches with low refractive index material, such as BCB (Benzo-CycloButene Cyclotene 3022-32, a polymer). Such large index differences can be used to make very wide stop bands. From a commercial point-of-view, it's economically desirable to omit regrowth. Wafer material can be bought from large wafer foundries and processed in-house, thus lowering start-up cost for a laser factory.

Deep-etched DBRs integrated with lasers in InP have been fabricated by a few groups. In 1997 Lammert et al. reported 500 nm deep, first order surface gratings made by Chemically Assisted Ion Beam Etching (CAIBE) [76] combined with wet etching to form the ridge. The gratings were made for single mode operation. The laser performance was good (thresholds of 32 and 43 mA for different etch depths) but suffered somewhat from the fact that the Bragg wavelength was redshifted with 40 nm from the gain peak, which was located at 1320 nm. Ke at al. etched first order gratings with CH_4/H_2-RIE to the depth of 1 μm in P-quarternary material [77], but the lasers had high current thresholds and low output power. Raj et al. also used the CH_4/H_2 chemistry to simultaneously dry etch fourth order gratings (740 nm wide openings) and a ridge through the active layer to a depth of 4 μm (but inside the grating the etch depth was only 3 μm because of microloading effects, see section 4.2.3) [53]. When etching through the active layer a high-reflectivity grating is formed with very broad reflectivity, such that no selectivity exists over the gain bandwidth. Such a grating is not useful as a filter.

So far there has been no reports on a mode-locked laser with a surface etched DBR to my knowledge. To design and realise a MMLL with a surface etched DBR is one of the goals of this PhD-project. The ridge and grating should be etched simultaneously. The ridge height is 2125 nm which is fairly high. This was a result of earlier designs where the loss from the contact and more importantly the bonding pad capacitance should be low.

3.2.3 Design flow of the DBR

The actual calculations needed to perform the design of the DBR are presented in appendix A. Here an overview will be given. The design of our integrated filter starts with choosing the Bragg wavelength, λ_B. Then the indexes in the low and high index regions, n_l, and n_h are calculated with a commercial mode calculation software (Selene, OlympIOs). The Bragg wavelength and indexes are fed to a matrix multiplication program made in Matlab. The Matlab program calculates the period, $\Lambda_m = \lambda_B m/\overline{n}_{ave}$ (λ_B is the Bragg wavelength, m is the order of the grating and $\overline{n}_{ave}$ is the average effective index of one period), and the length of the low and high index regions of the grating (see appendix A) for a specified order of the grating (e.g. 1, 2 or 3). The duty cycle is chosen to achieve

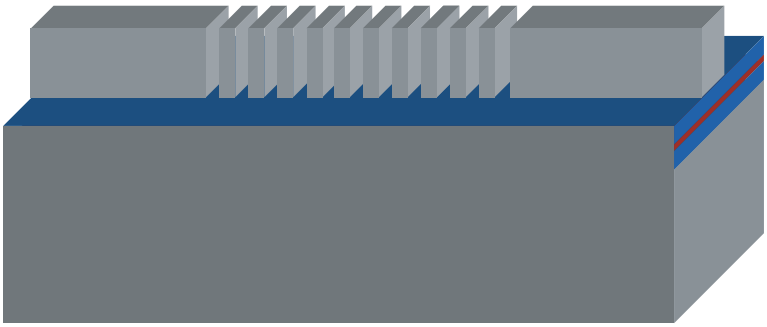

Figure 3.7: Drawing of a deeply etched Bragg grating of the type realised in this project (the fabrication is described in chapter 4). The grating is incorporated in the laser ridge. The trenches can be filled with a low-index material, such as BCB.

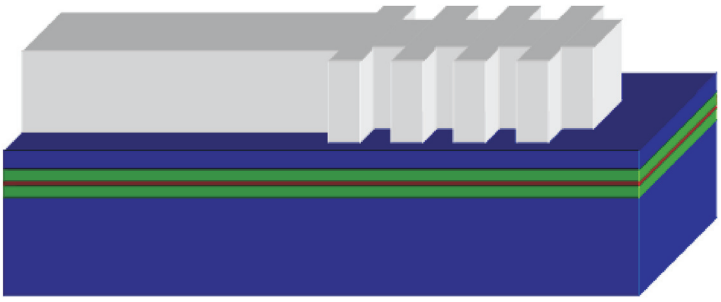

Figure 3.8: Another variation of the deeply etched grating (which was not realised in this project): here only the side of the ridge is modulated. This gives a lower index contrast between each step, but can give considerable advantages during processing.

the strongest coupling possible for each order, (see equation A.15 and figure A.5). The total peak reflectivity, R, and the FWHM bandwidth, λ_{FWHM}, of the filter is calculated and figure 3.9 plots R and λ_{FWHM} vs. the length of the grating for the first three orders, assuming the same index difference is achieved. For each length of the grating there will be a given set of reflectivity and bandwidth, which can be changed by changing the index difference or the order of the grating. The reflectivity and bandwidth should be chosen according to the requirements mentioned in section 3.2.2. The general trends are that longer gratings give higher reflectivity and narrower spectra. Increasing the order of the grating lowers both reflectivity and bandwidth for a given length. The coupling factor decreases for higher order gratings which reduces the strength of the grating

The order of the grating can be an important extra free parameter to play with when you are limited in other parameters, such as the index contrast. If for instance the index contrast is fixed (or only small variations can be achieved, because of a nearly fixed etch depth) then it's not possible to chose freely between different combinations of reflectivity and bandwidth. Difficulties with making high aspect ratio gratings might make it impossible to fabricate lower order surface gratings, making higher orders interesting.

3.2.4 Results

A deeply etched Bragg mirror has been designed for integration with a Ridge Waveguide (RW) mode-locked laser. Other types of filters have been taken into consideration, such as vertical and horisontal couplers and conventional Bragg gratings. The other options have been disregarded since they all require regrowth, which was not available. All DBR-calculations assume a Bragg wavelength of 1550 nm. Calculations of the index difference of an etched and unetched ridge (appendix A), consisting of the material structure that will be presented in section 4.1, shows that it should be possible to obtain a sufficiently large index contrast by deep etching the grating at the same time as the ridge is etched. The depth of the grating trenches is fixed by the depth of the ridge etch, 2125 nm (or more precisely the grating and ridge is assumed to be etched simultaneously). Figure 3.9 presents the reflection and bandwidth of different orders of a deeply etched grating, assuming that the depth of the trenches is 300 nm less than the ridge height because of the high aspect ratio of the etch (see chapter 4).

A more realistic scenario is that the etch depth in the grating is different for different aspect ratios and thus the index difference also varies. Such a calculation is presented in figure 3.10. Calculations of a first order grating is not presented since the 120 nm narrow pillar is expected to be eroded in the etch. Based on the requirements to have at least 5 % reflection and at least 2 nm bandwidth the length of the gratings were chosen to be between 80 and 145 μm.

Figure 3.11 presents the reflectivity and effective length vs. wavelength for an ideal third order grating with a length of 145 μm.

Figure 3.12 and figure 3.13 presents the reflectivity and the chirp for unideal conditions, including a higher loss, a random disturbance of the period, a mismatch in etch length (or duty cycle) and finally a finite facet reflection. A higher loss just lowers the magnitude of the reflection while the other disturbances to the grating induces an asymmetry in the shape of the filter. The chirp is small over the filter bandwidth for all cases but can be quite large depending on the phase of the facet

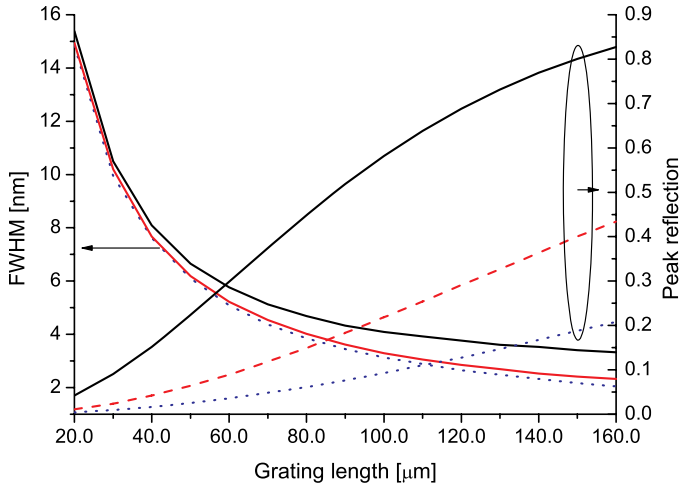

Figure 3.9: FWHM vs. grating length for 1st, 2nd, and 3rd order gratings. It is assumed that $\Delta n = 0.008$ for all orders, i.e. processing difficulties for higher aspect ratio openings are not taken into account. The Bragg wavelength is 1550 nm, the loss is 10 cm^{-1}, the index in the high index region is 3.199 and the duty cycle is optimised for each order. Ideal fabrication is assumed, meaning perfect period duty cycle and no facet reflections.

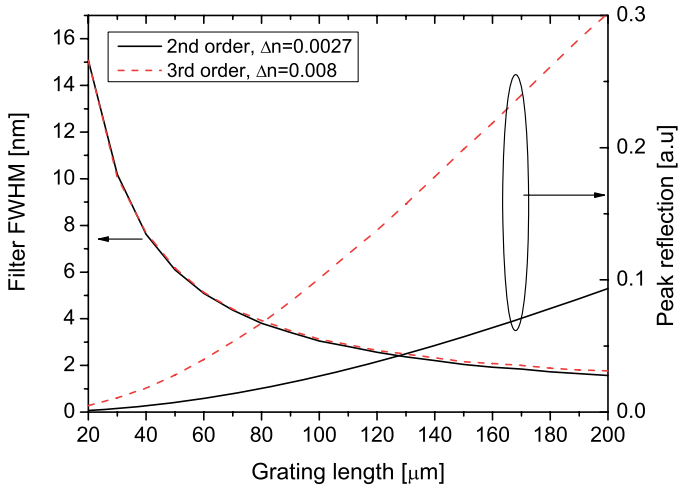

Figure 3.10: FWHM vs. grating length for second and third order gratings. Loading effects from high aspect ratio etching is taken into account. Etch openings are approximately 120 nm and 360 nm, corresponding to the ideal duty cycles of 25 % and 50 %. The pillar width is the same, 360 nm. $\Delta n_2 = 0.0027$ (etch depth is 1300 nm) and $\Delta n_3 = 0.008$ (etch depth is 1800 nm). Bragg wavelength is 1550 nm and loss is 10 cm^{-1}. Reflection from facet is set to be zero.

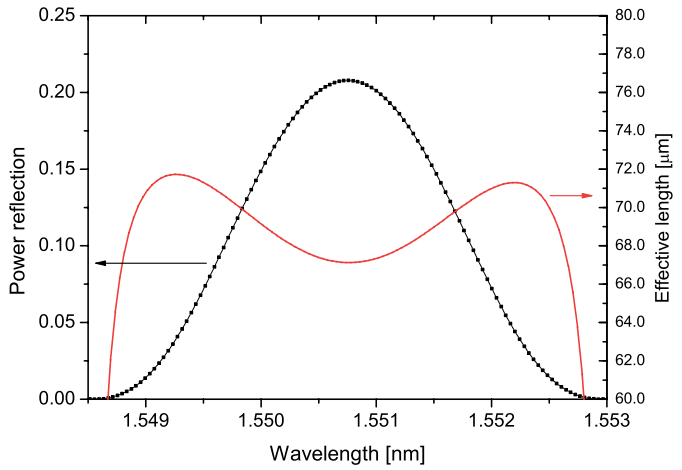

Figure 3.11: Reflectivity and effective length vs. wavelength for an ideal third order grating with a length of 145 μm. Bragg wavelength is 1550 nm and loss is 10 cm^{-1}. Reflection from facet is set to be zero.

reflection (not modelled here).

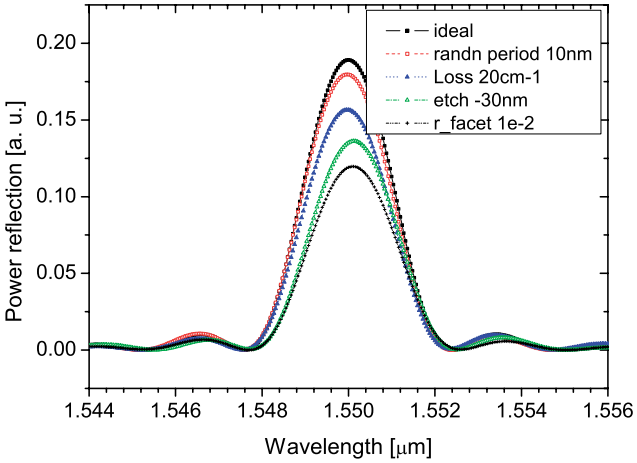

Figure 3.12: Reflectivity vs. wavelength for ideal and non-ideal third order gratings, all with a length of 145 μm. Bragg wavelength is 1550 nm. The first non-ideality is a random disturbance of the grating period. The following disturbances all include the preceding disturbances. Thus the next curve includes both a higher loss of 20 cm^{-1} and the random disturbance of the period. Then a mismatch of the etch length of -30 nm is inserted and finally a finite facet reflection.

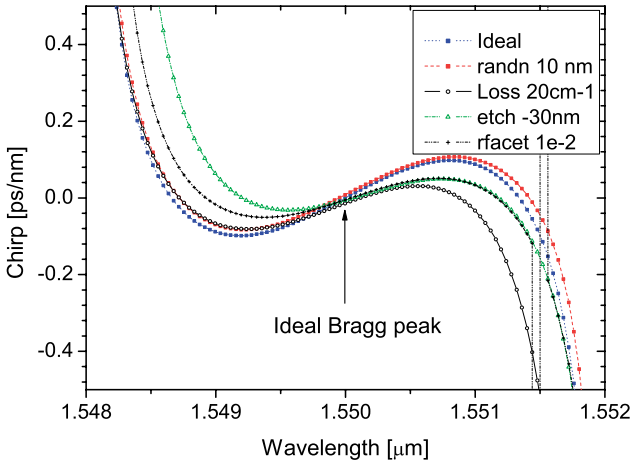

Figure 3.13: Chirp vs. wavelength for ideal and non-ideal third order gratings, all with a length of 145 μm. The same conditions as in figure 3.12 holds.

Chapter 4

Device fabrication

This chapter is concerned with the realisation of the designed lasers from the previous chapter. It starts with presenting the epitaxial structure, while most of the chapter is spent on an in-depth presentation of the dry etch optimisation of InP (and to some extent SiO_2), enabling the realisation of nanostructured DBR-mirrors without regrowth. Such deeply etched DBR-mirrors are an important step toward realising low-cost high-performance lasers from foundry-made wafer material. All fabricated lasers are Ridge Waveguide (RW) lasers, as depicted in figure 4.1. One of the restrictions on the process for the DBR is that it must be compatible with the process for making ordinary RW FP-lasers. The entire final process for the DBR mode-locked lasers is given in appendix C.

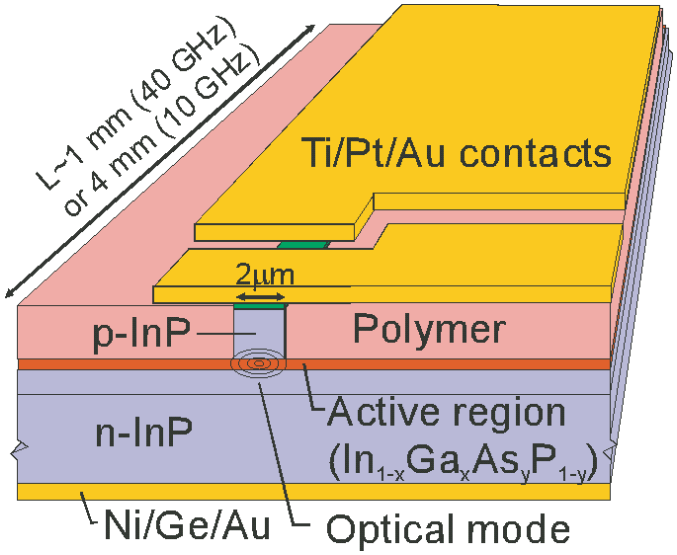

Figure 4.1: Drawing of Ridge Waveguide laser.

4.1 Epitaxial material of all-active lasers

This section presents the epitaxial structure of the wafer used for fabrication of MMLLs with DBR-mirrors (structure MMLLSOA3). It also presents the epitaxial structure of the other QW-lasers which have been examined (characterised) throughout this project (structure SCOOP6). The actual growth and related issues, such as band calculations and reactor calibration was not performed by me and will not be discussed here. Instead, the readers are referred to [30]. The two epitaxial structures (shown in table 4.2and X), which are similar, are implemented after the design ideas in section 3.1, which are brief references of [39, 30]. The quantum wells in MMLLSOA3 and SCOOP6 are $In_{1-x}Ga_xAs_yP_{1-y}$, grown with constant y, zero net strain. While MMLLSOA3 have only one quantum well, SCOOP6 can have 1, 2 or 3 wells. The most significant difference lies in the use of Al-containing barrier layers in the MMLLSOA3-design. The Al-barriers reduces thermionic emission of electrons at high currents in the gain section and facilitates the sweep-out of holes in the negatively biased absorber.

The material used for the fabricated lasers have been grown by Metal-Organic Vapour Phase Epitaxy (MOVPE, sometimes called Metal-Organic Chemical Vapour Deposition, MOCVD). The actual growth of the MMLLSOA3-structure was performed by Landmark, a Taiwanese foundry company. Figure 4.4 shows a schematic of the MMLLSOA3 structure with a blow-up of the waveguide region.

Table 4.1: Epitaxial structure of the wafer material used for the DBR-MMLLs (MMLLSOA3).

Layer	Material	(x)	(y)	Strain (%)	Thickness (μm)	N (cm^{-3})	dopant
14	InP				0.025	>1e18	Zn
13	$GaIn_xAs$	0.53		0	0.175	>1e18	Zn
12	$GaIn_xAs_yP$	0.67	0.71	0	0.1	>5e18	Zn
11	InP				0.9	>1.5e18	Zn
10	InP				0.5	9e17	Zn
9	InP				0.4	5e17	Zn
8	InP				0.05		
7	$GaIn_xAs_yP$	0.85	0.32	0.00	0.24		
6	Al_xInAs	0.48		0.00	0.02		
5	$(Al_xGa)In_yAs$	0.16	0.53	0.00	0.015		
4	$GaIn_xAs_yP$	0.71	0.90	0.90	0.007		
3	$(Al_xGa)In_yAs$	0.16	0.53	0.00	0.005		
2	$GaIn_xAs_yP$	0.85	0.32	0.00	0.24		
1	InP				1	1.5e18	Si

4.2 Process development of dry etching

4.2.1 General concepts

Dry etching is used in the laser processing to define the ridge and the perpendicular grating. In general dry etching is used for precise pattern transfer down to the

Table 4.2: Epitaxial structure of SCOOP6-3, where -3 denotes the use of three quantum wells. Q(λ) denoted the quarternary InGaAsP compound that has a bandgap of $\lambda\,\mu m$ and is lattice matched to InP. The structure with one and two quantum wells is adjusted such that the Q(1.29) layers are made thicker to preserve the same total thickness.

Layer	Material	Dopant conc. (cm^{-3})	Thickness (nm)
16	Highly doped InGaAsP contact layer		275
15	InP:Zn	$2 \cdot 10^{18}$	900
14	InP:Zn	$9 \cdot 10^{17}$	500
13	InP:Zn	$5 \cdot 10^{17}$	200
12	InP:Zn	$1 \cdot 10^{17}$	200
11	Q(1.1):Zn		10
10	InP		40
9	Q(1.07)	0.85	200
8	Q(1.29)		18
7	$In_{1-x}Ga_xAs_yP_{1-y}$ x=0.530, y=0.86		3.7
6	$In_{1-x}Ga_xAs_yP_{1-y}$ x=0.268, y=0.86		7.2x3
5	$In_{1-x}Ga_xAs_yP_{1-y}$ x=0.530, y=0.86		7.3x2
4	$In_{1-x}Ga_xAs_yP_{1-y}$ x=0.530, y=0.86		3.7
3	Q(1.29)		18
2	Q(1.07)		200
1	InP:Si	$1.5 \cdot 10^{18}$	1000

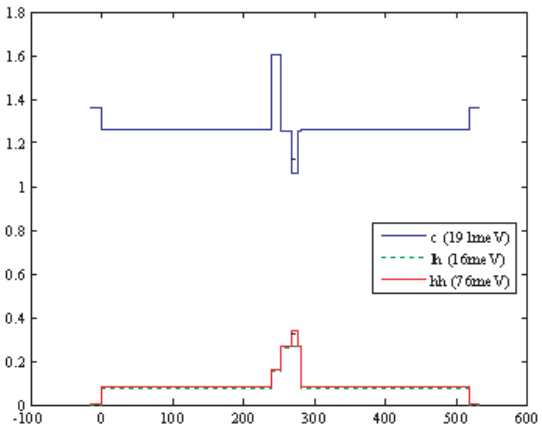

Figure 4.2: Band diagram of MMLLSOA3 showing the waveguide region with the QW and Al-containing barrier. X-axis: depth in nm. Y-axis: Energy in eV. (0,0) corresponds to layer 8.

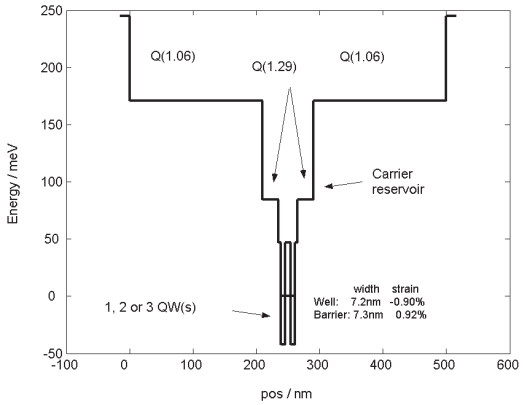

Figure 4.3: Band diagram of SCOOP6_2.

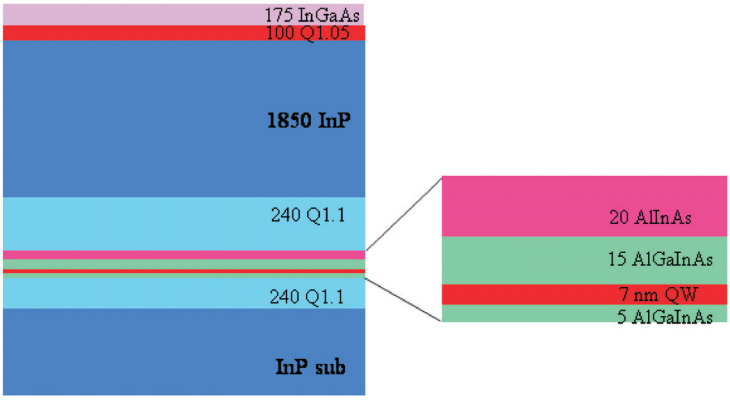

Figure 4.4: Schematic (not to scale) cross-section of the whole epitaxial structure of MMLLSOA3-wafer.

nanometer scale, which is possible because of the high anisotropy of the etch. Wet etching is usually isotropic and hence cannot be used for small patterns with large etch depths. The selectivity over other layers/materials can however be worse for dry etching than for wet etching. Reactive ion etching is often divided into two subcategories according to which etching mechanism is the dominant: ion assisted chemical etching & physical etching (sputtering). Both the dry etches described in this thesis are thought to be mainly ion assisted chemical etching, where the ions contribute with energy for the chemical reaction or for desorption of the formed reaction product [78, 79] (see section 4.2.3 for details).

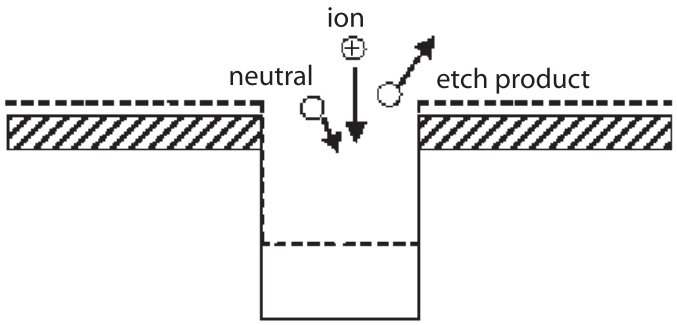

Figure 4.5: Simplified picture of reactive ion etching. The neutrals react with the atoms at the surface. The ions provide extra energy for the reaction or the removal of the reaction product, thus increasing the etch rate at surfaces open for ion bombardment.

Ion assisted chemical etching The chemical etching in plasma systems is usually performed by free radicals. A free radical is a neutral atom or molecule that have unpaired electrons. The flourine free radical used for etching silicon dioxide is such an atom. It has seven outer electrons instead of the more energetically favourable eight. This means that the reactivity with other atoms or molecules is very high in order to produce more stable products. Free flourine atoms can be produced in plasmas were the high energy electrons can break bonds of the input gases. The free radicals can then react with the material to be etched to form the more stable products. The volatility of the product is very important in order for it to leave the surface and expose new material. Such chemical etching is however isotropic and will work very much like a wet etch. By introducing a voltage drop between the plasma and the wafer electrode, positive ions will be accelerated toward the wafer, see figure 4.5. In contrast to sputtering, where the ions physically break the bonds of the crystal, the energy of the ions (which is much lower for ion-assisted etching than for sputtering) can enhance one or several steps in the chemical etching, such as surface adsorption, etching reaction or removal of etch-products. The enhancement will only take place where the ions hit the surface. The result is an etch that is much faster than the sum of the physical and chemical etches, in case only one of them were present, and with an anisotropy almost as good as for sputtering but with a much better selectivity and less damage to the crystal.

Technical specifications Our RIE system is a parallel plate system from PLASSYS with an RF-frequency of 13.56 MHz. The oscillating electromagnetic field creates a plasma and a voltage drop between the plasma and the wafer. Most of the RF-power at 13.56 MHz goes into ion energy (accelerating voltage drop). The ion concentration is mostly dependent on the flow and pressure of the gases [80]. Other RIE-systems exist where a high density plasma is created by induction, but the voltage drop is controlled a parallel plate RF-power. Thus two different frequencies are used to control the ion energy and concentration separately. These systems are generally just referred to as Inductively Coupled Plasma (ICP) etching systems. In our chamber the cathode is covered by a quartz plate with a diameter of 20 cm. Gases have an inlet in the top which also serves as anode. The gas inlet is distributed in the form of small holes in a ring with a diameter of 3 cm. The chamber is pumped by a combination of rather small pumps, which does not allow independently selecting flows and chamber pressure (this will be further discussed in section 4.2.3).

Through the top lid is a glass window which allows for in-situ laser end detection of transparent materials (at $\lambda = 628$ nm). The reflectivity is measured during the etch and will go through an oscillation of maxima and minima as the path length forth and back through the material changes. As soon as the transparent material is etched through there will be no further change in reflectivity.

The etch is changed by the chamber conditions, such as the concentration of free radicals and ions and the voltage drop between the plasma and the electrode. Unfortunately we cannot change these chamber conditions directly. We are restricted to the control of the power, the pressure, the flow, the mixture of the gases and to the cathode temperature. How we have optimised these chamber parameters will be discussed individually for the two etches developed for etching SiO_2 and InP.

4.2.2 SiO_2-RIE

The etching of SiO_2 is well developed and well described since it is one of the most important materials in the microelectronics industry. Almost any university text book on microelectronic fabrication can be used as a reference, e.g. [78]. Flourine based etches are well suited for the etching of silicon dioxide, because of the high volatility of the etch product SiF_4. This means that once it is formed it can easily leave the surface (desorption). We make use of a combination of CHF_3 (Freon) and O_2, where the small amount of oxygen is used to prevent formation of organic residues (originating from the carbon content in CHF_3). The masking material for pattern transfer can be both electron beam resist, e.g. ZEP520-A, or a UV-resist such as the AZ5206 (AZ5214 with extra thinner). The most significant chamber reactions are [78]

$$e^- + CHF_3 \rightarrow 3F + CH + e^- \tag{4.1}$$

$$4F + SiO_2 \rightarrow SiF_4 + O_2 \tag{4.2}$$

Selectivity, verticality and uniformity The used chemicals do not etch the underlying InP or InGaAsP by chemical reactions. Thus any etching of the InP is pure sputtering. This sputtering can be controlled by the induced bias (controlled by setting the power), where a higher voltage results in more sputtering. We

varied the power from 40 to 80 W, see figure 4.6, and found that above 330 V the sputtering of the underlying semiconductor was too severe. At 80 W the etch rate of the glass was also too high to obtain reproducible etches for layers of 100-200 nm.

The selectivity over the resist mask is approximately the same for both electron beam resist and UV-resist (a little worse for e-beam resist). The resists etch faster for a higher bias but the selectivity seems to be nearly constant over the bias range tested here. Instead the resist selectivity is very dependent on the oxygen content: a low oxygen content means high selectivity and a high content results in low selectivity. However, with very little or no oxygen there will be polymerisation on the sidewalls from the carbon rich gas, resulting in angled sidewalls. The optimum is reached for the lowest oxygen content that results in no polymers on the sidewalls (table 4.3). The uniformity of the etch over the wafer is good since the wafer is surrounded by the quartz plate.

Table 4.3: Settings of the chamber parameters and resulting bias for the developed SiO_2 etch: SiO2_602 (see table 4.4 for etch rates).

Flow CHF_3/O_2 (sccm)	Pressure (mTorr)	RF-power (W)	T (°C)	V_{bias} (V)
18(16/2)	100	60	20	300

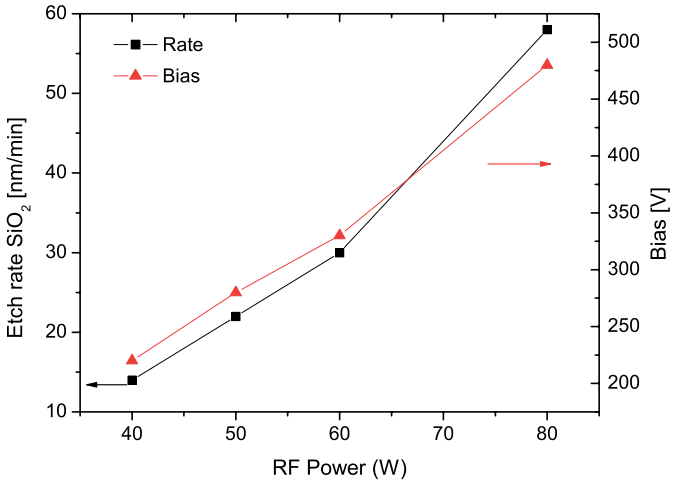

Figure 4.6: SiO_2 rates and bias vs. power for glass-RIE. The rates have been obtained by the in-situ reflectometer described below or by stylus profilometer before and after etching (the two methods give coherent results). Other chamber parameters are: pressure 100 mTorr, Flow 16/2 (CHF_3/O_2) sccm and plate temperature 20 degrees Celsius.

Table 4.4: Etch rates of glass, resists and InP for the chosen glass etch.

etch	SiO_2 rate (nm/min)	ZEP rate (nm/min)	AZ rate (nm/min)	InP rate (nm/min)
SiO2_602	27	30	25	2.5

End-point detection The etches are timed after having determined the etch rate on test wafers. The etch rate can be established either by Dektak measurements or with the in-situ laser reflectometer. Since the etch rate is very reproducible there is no need for individual end-point detection. As an extra security however it is possible to detect the endpoint of each individual process with the in-situ laser reflectometer. Since we observe microloading effects on our samples, where open areas etch faster than small openings and areas close to masked material, such as ridges, there is a need for a certain amount of overetch. The overetch time was established by etching different samples with longer and longer overetches until all unmasked glass was removed.

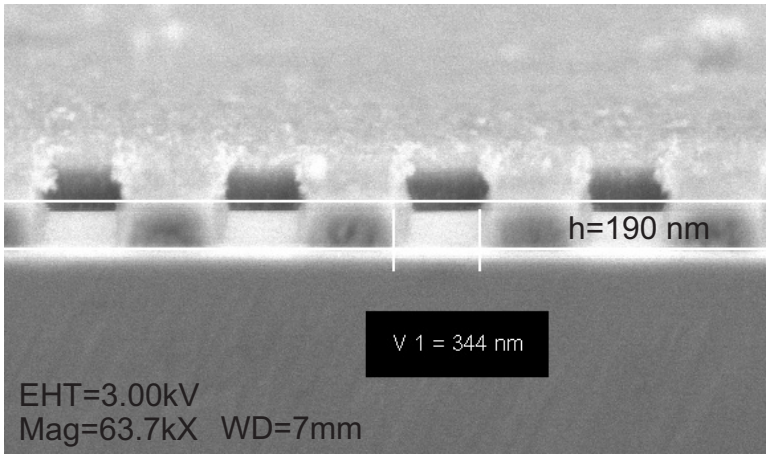

Figure 4.7: SEM micro graph of SiO_2 grating mask after grating glass etch.

The obtained etch has a suitable etch rate for the etching of films with thicknesses in the range 50 to 500 nm with reproducible results. The slope of the sidewall, see figure 4.7, is almost vertical because of the high bias, removal of polymer film with oxygen and the over etch.

4.2.3 Metal Organic RIE of InP/InGaAsP

General The first use of CH_4/H_2 chemistry to etch InP was performed by Niggebrügge et al. in 1985 [79]. At that time $Cl_2 - based$ dry etching of InP and related materials existed but has some serious disadvantages: toxic and corrosive etch products, a low volatility of the indium chloride etch product (an elevated process temperature is necessary, 150-200 °C [81]), rough surfaces because of the low volatility of the indium chloridcyclicallyes and heavy erosion of common masking materials (e.g. silicon dioxide). There are of course some drawbacks with the

methane based etch too: It requires seasoning of the reaction chamber and periodic removal of polymer from mask and chamber walls. The etch rate is usually quite low (tens of nanometer per minute). Creation of Phosphine (PH_3) as etch product (toxic). Since then there has been a number of reports on etching InP with CH_4/H_2 in parallel plate systems. While most of the articles focus on the use of the etch for making devices, e.g. [82], a few of the reports have tried to analyse the physical events and chemical reactions in the chamber while changing the chamber parameters (power, pressure and flow) in order to optimise the etching [83, 84, 85].

Applications of MORIE Wet etching of InP can be performed in a mixture of HCl and H_3PO_4 with a high rate and with very good selectivity over quarternary material (InGaAsP). However wet etching of InP and related compounds suffer from being isotropic for most crystal planes. The exception is the [0, $\overline{1}$, $\overline{1}$]-plane. Everything with etch planes with an angle against the [0, $\overline{1}$, $\overline{1}$]-plane will etch nearly isotropically. The result is that micro or nano patterning isn't possible in all directions, especially if deep etches are desired. Such patterning could be etched mirrors [80], waveguides [82, 86], Y-splitters or distributed gratings [53, 54]. One of the most recent and impressive device fabrications comes from the University of Tokyo, were fourth order distributed Bragg gratings with 3 micrometer depth have been made with an ordinary parallel plate RIE-system (Samco RIE-10NR). However, the etch was made through the waveguide and active layer. This relaxes some of the process tolerances (difficulties) such as non-uniformity and micro loading effects in the gratings. Etching through the waveguide results in a very broad reflection spectrum, which will not act as a wavelength selective filter. The purpose of the gratings in [53, 54] was a short high-reflectivity mirror (95 % reflectivity for 15 periods, each period was 1.34 micrometer).

InP is not the only material that can be etched by a methane-hydrogen plasma; InGaAsP, InGaAs and GaAs can also be etched but with decreasing etch rate when going toward GaAs [79]. For the sake of simplicity and because our etch consists of 87 % InP-etching (the contact layers are Q(1.3) and InGaAs, 275 nm in total) the rest of the discussion will assume we are etching InP.

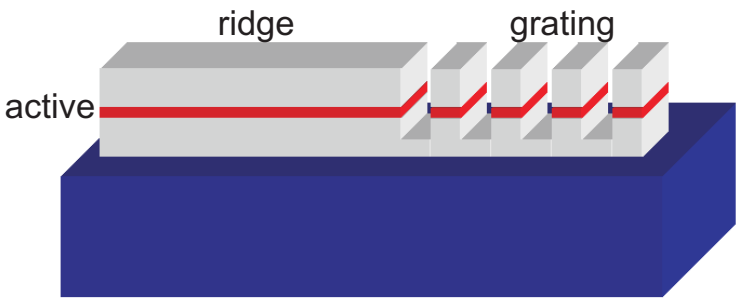

Figure 4.8: Sketch of the Japanese high-reflectivity surface grating. The etch is continued through the active layer to achieve high index contrast.

Chemical reactions Several early observations supported the fact that the etch by MORIE was primarily chemical. Niggebrügge [79] compared SEM-pictures of samples etched with CH_4 and Ar, and found a substantially lower etch rate for the Ar-plasma (although Ar is recognised as a very good sputtering species). He also found the formation of a protective carbon-rich film on SiO_2 and resist (which also suggests chemical etching), with a deposition rate of 1-6 nm/min. The film could be removed with an O_2-plasma (suggesting organic content). Since etching can be thought of as the reverse of epitaxy, it is natural to think that In would leave the surface as an organometallic compound, and P as phosphine (PH_3). Hayes et al. detected PH, PH_2 and PH_3 in a mass analysis of the MORIE plasma in 1989 [83] and so did Feurprier et al. [84]. Both neutral hydrocarbon species, C_xH_y, with x ranging up to 7, and hydrocarbon ions with x up to 11 has been observed by optical emission spectroscopy on the plasma [84]. The $C_2H_5^+$ was found to be the major ion-component of the plasma. It was also suggested in [84] that the primary etchant of In was neutral methyl radicals, since the concentration of the methyl radicals matched the etch rate when changing the methane concentration of the input gas mixture from 0 to 75 %. The etch rate seemed to be limited by the removal of In, since the etch rate matched the strength of the optical emission of In in the plasma. The stoichiometry of the etched surface has been studied by means of surface analysis, such as x-ray photoelectron spectroscopy (XPS). It was found that the surface was P-depleted and that the depletion decreased with increased methane content (In/P-ratio of surface: 0.5-0.7). However the ratio was never one and thus the surface will always be depleted of phosphor. The three most important reactions in the chamber are

$$e^- + CH_4 \rightarrow CH_3 + H + e^- \tag{4.3}$$

$$3CH_3 + In \rightarrow In(CH_3)_3 \; and \; 3C_2H_5 + In \rightarrow In(C_2H_5)_3 \tag{4.4}$$

$$3H_2 + 2P \rightarrow 2PH_3 \tag{4.5}$$

The following paragraphs will treat the effects of changing the chamber parameters: power, pressure, partial pressure, flow and temperature.

Power Generally an increased RF-power results in both an increased production of free radicals and ions, and also increased energy of the ions hitting the sample (the bias). All these things tend to increase the etch rate. Both [83, 85] found a linear relationship between the etch rate and the RF-power, as we also have found (over the explored range), figure 4.9. A higher energy of the ions increases the physical etching. A too high physical etching leads to unwanted surface roughness, inset of figure 4.9 and figure 4.10, while a too low bias results in polymerisation on InP (150 V in [79], 200 V for [85]). In order to find the highest bias giving a smooth surface, SEM-micro graphs were taken on 3 different samples etched with 60, 80 and 100 W RF-power (corresponding to biases of 430, 490 and 560 V) but otherwise with the same chamber parameters. Both the 100 W and 80 W samples had considerable surface roughness, see figure 4.9 and 4.10.

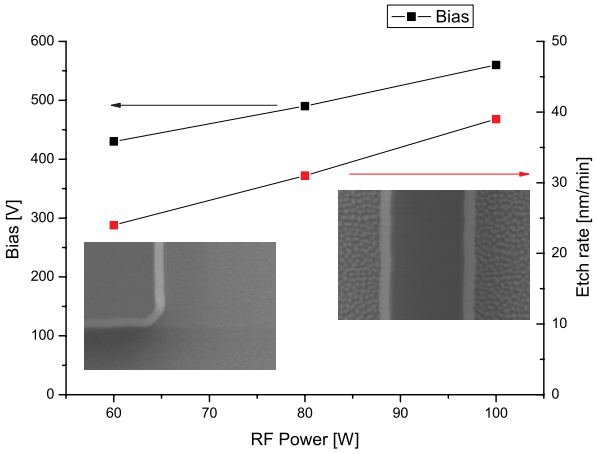

Figure 4.9: Etch rate and bias vs. RF-power. Pressure is 80 mTorr, total flow is 42.1 sccm and CH4-content is 25 %. The small SEM micro graphs were taken at 60 W and 100 W RF-power, and is included to illustrate the surface roughness dependence on bias.

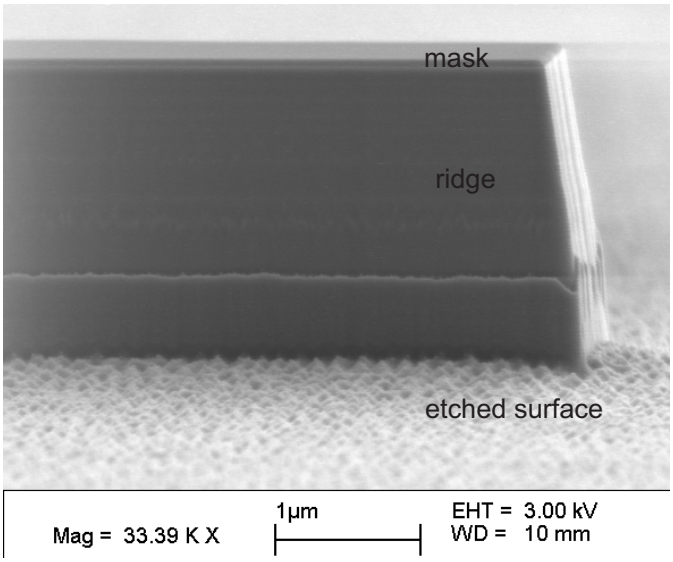

Figure 4.10: SEM-micro graph showing surface roughness on a sample etched with 570 V bias.

Pressure and partial pressure of CH_4 (gas mixture). Increasing the chamber pressure means an increase in the density of methane and hydrogen in the chamber. This in turn leads to an increase in the density of free radicals and ions. The result is an increased etch rate and also an increased polymer deposition rate. The dependence on total pressure is however not as strong as the dependence on the methane partial pressure. Increasing the methane content increases the methyl density. For low partial pressures (∼up to 30 % methane) the etch rate increases strongly with higher methane content, but for higher contents the etch rate saturates and increased polymer deposition occurs on inert surfaces such as masks (e.g. SiO_2) [83, 85]. At even higher partial pressures there is even polymer deposition on InP surfaces. Decreasing pressure results in a decrease of the etch rate and polymer formation, but also results in an increase of the physical etching compared to the chemical.

Flow Generally both the etch rate and polymer deposition rate should increase for a higher flow according to [83], since the number of methane molecules available for reaction increases per unit time. However, the ratio of etch rate and deposition rate is not constant when varying the flow or rather the nominal residence time, τ, given by

$$\tau = \frac{P \cdot V}{Q} \tag{4.6}$$

Where P is the pressure, V the chamber volume and Q is the flow (Q should be expressed in Torr litre/s).

$$1sccm = 1cm^3/min \,@\, 760Torr = 0.3167Torr\,litre/s$$

Hayes et al. [83] found that changing the nominal residence time (in their case only by changing the total flow rate and keeping the pressure constant) can change the ratio of InP etch rate to the polymer deposition rate. In their case this ratio increased when going from residence times 1.0 to 0.4 seconds. Hayes et al. also found that decreasing the pressure from 90 mTorr to 50 mTorr, while maximising the flow (to keep a short residence time) would increase the etch rate to deposition rate ratio from 22 to 37. With Hayes equipment, 50 mTorr was the lowest possible pressure where a plasma could be ignited. Table 4.5 presents the residence time for four of the etches tried in my development study. Lowering the pressure results in a shorter residence time although the maximum flow had to be lowered because of the small pump. To conclude this paragraph, the etch with the lowest pressure in table 4.5 should maximise the etch to deposition ratio. This is important since an oxygen etch is cyclically used to remove the polymer. Long oxygen etches also sputter the glass mask where it is not covered (polymer does not form homogeneously) and secondly increases the total etch time, which is several hours.

Temperature The dependence on temperature (i.e. plate temperature, the actual wafer temperature will be higher) is low, and the etch rate increases with only 10% when going from room temperature to 100 °C [79]. Because of the low influence, the temperature has not been varied in this study. All etches presented in this thesis have been performed at 20 °C (or 25 °C).

Table 4.5: Nominal residence time in seconds for different etches tried during the etch development. The chamber volume is ~7 litres (30 cm in diameter).

Etch #	P (mTorr)	Q (sccm)	t (s)
1	100	42	1.32
2	80	42	1.05
3	50	37	0.75
4	25	26.5	0.52

Mask erosion, verticality and etch depth Ridge verticality depends to a large extent on mask erosion. The ions hit the surface under near vertical angle, which results in very etch rate of the sidewalls. Mask erosion has been studied for different masking materials in for example [82]. SiO_2 does not have the least erosion of the known masking materials, but we have chosen it because it's easy to pattern with dry etching, it's easy to remove and it's compatible with other materials (it doesn't contaminate). In particular titanium seems to be a popular masking material [82, 53]. As a matter of fact deeply etched gratings with very high quality has been fabricated with Ti as an etch mask [53] (as mentioned before). Erosion of SiO_2-masks has been studied in [87], where a weak dependence was found on bias and methane content. Nor did the sidewall angle of the mask have any strong impact on the erosion. The measured erosion was 400-600 nm normalised to an etch depth of 3.5 μm (corresponding to 250-380 nm for an etch depth of 2.2μm). The horisontal mask erosion measured in our etch was about 300 nm (total erosion from both sides) at the desired etch depth (mostly depending on the total etch time). The corresponding horisontal rates were quite similar and of the order of 3 nm/min. The vertical etch rate of horisontal mask surfaces is about 1 nm/min in our etches, and is also very weakly dependent on process parameters. The maximum etch depth is governed by the mask erosion for a given set of chamber parameters.

Micro uniformity/microloading Microloading is the change in etch rate seen in small mask openings. We observe microloading effects in the grating trenches (120 - 360 nm wide). The middle of the trench etches more slowly than the edge after a certain etch depth. How much slower is dependent on the aspect ratio of the trenches. The more narrow the trenches are the higher will the aspect ratio be for the same etch depth and the more severe will the microloading be, see figure 4.12. Shadowing by atoms or molecules can be ruled out as a cause because of the low pressure during the etch (below 100 mTorr). The mean-free-path of the particles in the chamber is inversely proportional to the pressure and is given by [78, ch. 9],

$$\lambda = \frac{kT}{\sqrt{2}\pi d^2 P} \tag{4.7}$$

where λ is the mean-free-path, k is Boltzmann's constant, T the temperature in Kelvin, πd^2 is the cross-section for collisions of the particles (d is approximately 0.4 nm for most molecules of interest) and P is the chamber pressure. At room temperature the length between collisions is about 0.4 mm at a pressure of 100 mTorr. One possible reason for a lower etch rate could be geometrical shadowing by the pillars. Both ion and radical shadowing are well documented in silicon RIE with high aspect ratios [88]. The etch rate in a RIE can be described with the

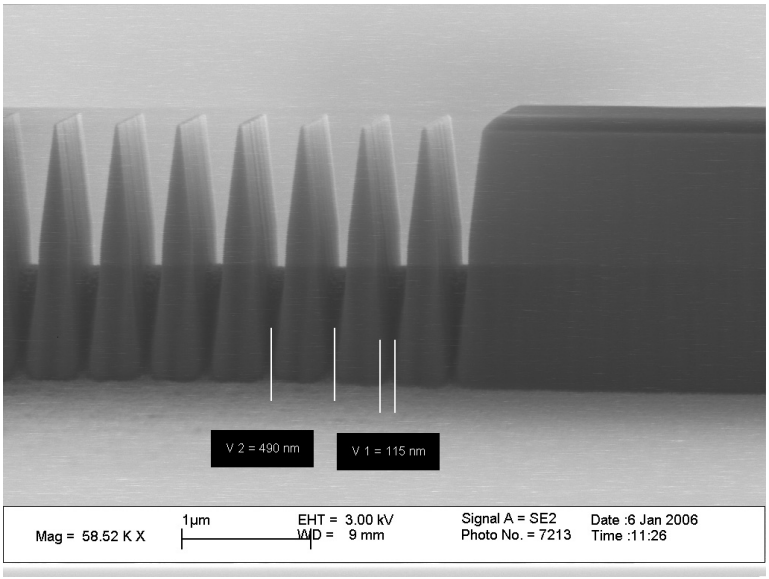

Figure 4.11: SEM micro graph showing mask erosion and verticality differences.

following equation [88]

$$\frac{1}{R} = \frac{1}{k_R \phi_R S_R} + \frac{1}{k_I \phi_I E_I} \tag{4.8}$$

where k_I is the volume removed per unit ion bombardment energy, k_R is the volume removed per radical, ϕ_R is the radical sticking-flux, ϕ_I is the ion energy-flux, S_R is the sticking probability of the radical on a bare surface and E_I is the ion energy. Whenever either of the fluxes is small the etch rate drops dramatically. This means that a lag in etch rate will be seen even if only one of the fluxes is decreased. Although the ions are strongly accelerated toward the wafer surface by the strong field (400-500 V), there is still a narrow distribution of arrival angles. The ion angle distribution (IAD) and the ion energy distribution (IED) was measured by Liu et al. [89] for Ar-plasmas vs. pressure and bias. A low pressure and high bias was favourable for a narrow distribution of ions and energy, and also favourable for ions with a high energy. At a peak-to-peak voltage of 130 V (the DC-bias was not given but was assumed to be a few volts more than $1/4$ V_{pp}) and a pressure of 10 mTorr the average angle was 10°, and at 50 mTorr it was 13°. Jensen [88] found that the critical aspect ratio, $AR_c$was equal to half the FWHM of the IAD for narrow distributions (low pressure). Thus it is very plausible that ion shadowing is part of the RIE lag seen in my etches. In contrast to the ions, the neutrals hit the surface coming from all angles. Since we have a large mean-free-path, the chemical flux to any point in the grating will be given by the space angle it sees, which is dependent on the aspect ratio of the trench (figure 4.12), but also on the position in the grating. A smaller space angle means a lower chemical flux and thus a lower etch rate. The fact that there is an increased RIE lag effect close to the sidewall at the bottom of the pillars in figure 4.12 supports the theory of a lag caused by ion flux shadowing. At the very bottom it looks like there is a lag effect even at the edge of the grating close to the sidewall. The radical flux is the same close to

the sidewall as in the center (moving along the ridge direction), since the radical flux is evenly distributed. The ion shadowing is different: although ions with 10° angle will still reach the bottom of the sidewall, they are few because of the narrow distribution and they have a lower energy.

The consequences of the loading effect are that the index difference will be smaller than for a corresponding grating without loading effects and that the simulation of the mode and index requires a somewhat more complex modelling of the geometry to give "exact" values. Depending on how big the effect is it can make the index difference too small for a reasonable reflectivity, since the overlap of the mode and the grating is highest in the middle. There is actually one positive result of the micro loading effect also. If the loading isn't very big, say 100-200 nm, then the small "bump" in the middle helps to form a more guided mode also in the trenches. So we conclude that a small loading effect could be desireable but a too large will kill the grating.

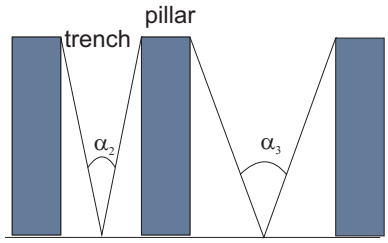

Figure 4.12: Drawing of grating trenches to illustrate the influence of the aspect ratio. The angles of the fully etched 3rd and 2nd order trenches are given by: $tan\frac{\alpha_3}{2} = 180/2100$, $\alpha_3 = 9.8°$, and $tan\frac{\alpha_2}{2} = 60/2100$, $\alpha_2 = 3.2°$

To minimize the micro loading effect we chose a 3^{rd} order grating with trenches of 360 nm and 50% duty cycle. A 2^{nd} order grating could be made with the same trench length but that would mean a pillar length of 120 nm and the mask erosion would destroy the pillars.

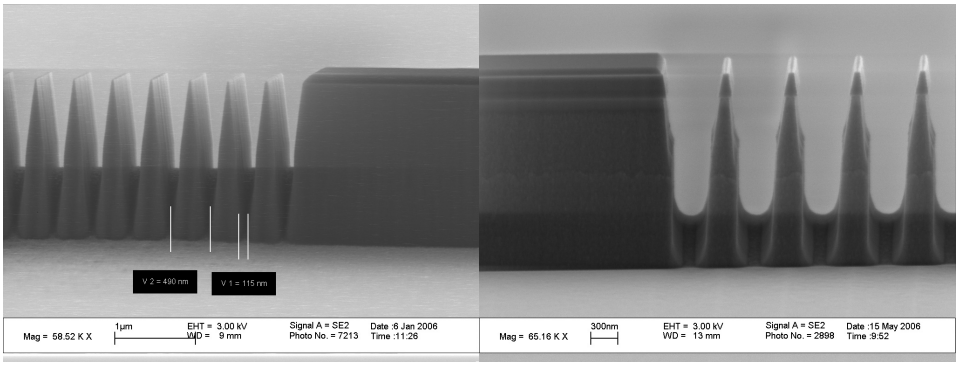

(a) original mask opening of 120 nm (b) Original mask opening of 360 nm.

Figure 4.13: SEM micro graphs of micro loading effects in deep gratings.

Ways of reducing the bump by changing the process parameters was also per-

formed. By reducing the pressure the ion energy flux should become more narrow. When decreasing the pressure it was also necessary to decrease the total flow because of the limitations of the pump.

Macro uniformity Macro uniformity over the whole wafer area is important, in order to achieve the same device performance over the wafer and to be sure not to etch into any layer that cannot tolerate etching. For the grating fabrication a depth non-uniformity means that the reflectivity and bandwidth will change somewhat over the wafer (this could of course be a positive feature when you are in the test stadium, however when one has found a suitable process and device design, this variation will kill device performance). A depth difference of 100 nm corresponds to a change in index contrast of about 0.004 (see appendix A).

In [90] Janiak and Niggebrügge found that the etch rate depends on the lateral position on the wafer for wafers with a low degree of masking (a few percent), but the etch rate was nearly uniform all over the wafer for a mostly covered wafer. An increased etch rate was found going from the center of the wafer to the edge. A plausible theory for the increased etch rate was suggested: the higher concentration of etchant outside the wafer (because there is a lower consumption) creates a gradient and flux toward the center of the wafer. This lateral flow causes an increased etch rate at the edges. A hyperbolic cosine function was derived from one-dimensional modelling and could be fitted to all of their data, equation 4.9

$$r(x) = r_v + r_l(x) \propto C_v + C_l(x) = C_v + Kcosh(x/L) \tag{4.9}$$

where r is the total etch rate, x is the lateral displacement from the center of the wafer, r_v is the vertical etch rate proportional to C_v which is independent of x, r_l is the lateral etch rate, K is a constant and L is the lateral diffusion length of the reactive species. It was also found that the only chamber parameter affecting the non-uniformity was the pressure. A lower pressure would lower the non-uniformity. As the overall etch rate also decreases with pressure, this method has it's clear disadvantage. Instead a "guard ring" was suggested. Several rings around the wafer with different heights were tested and the non-uniformity could be changed from high to zero and even negative. Such a ring can effectively stop the lateral diffusion of gases.

Janiak and Niggebrügge found that the zero-diffusion ring height was independent of pressure. The uniformity was also improved with a so-called "getter plate" (an underlying InP-wafer with greater radius, in this particular case a 3" wafer). A summary of my own work on non-uniformity issues is presented in table 4.6. Since our tests were performed on parts of wafers there was no circular symmetry, and thus the analysis a bit more difficult. Anyway, uniformity values are calculated from the maximum etch depth (at the edge) divided by the minimum (centre) etch depth. We also found a rate distribution with an approximate hyperbolic secant dependence. The tested guard rings all had a circular shape with a diameter of 60 mm (slightly larger than a 2" wafer). We found a clear increase in uniformity with a guard ring of the right height, but also an unexpected small decrease of the etch rate. A quarter-wafer shaped guard ring was also made but there was no time to test it.

Dry etch induced damage and post-treatment Three different types of damage are known. Closest to the surface there is a phosphor depletion, 2-3 nm deep,

Table 4.6: Experimental non-uniformity of etch depth of ridges in InP using the PLASSYS MG300. Non-uniformity was calculated from max and min data.

Sample	Pressure (mTorr)	Guard ring height (mm)	Getter plate	Non-Uniformity (%)	Rate (nm/min)
1	80	no	2"	8	28
2	25	no	2"	6	18
3	25	no	-	6	26
4	25	5	2"	-25	14
5	25	4	2"	1.2	15
6	25	4	-	3.5	20

because of the lower binding energy and higher reactivity of phosphor [91]. The ratio of P and In atoms in the surface layer is affected by the choice of etching parameters, most effectively by the partial pressure of CH_4. A higher methane ratio will decrease the P-depletion. Below the P-depleted layer there is an ion induced lattice disorder. The amount of damage depends on the bias. The third kind of damage is impurity in-diffusion (hydrogen) to a depth of 100-200 nm. In order to remove the damaged material the wafer can be treated with a wet etch with a sufficiently low etch rate. Such a wet etch is concentrated H_2SO_4 (sulfuric acid) [92]. We found an etch rate of 16 nm/min for InP close to the RIE-etched surface and a rate of around 12 nm/min for the material further down. No etch in quarternary material could be detected from our experiments. We have measured the photoluminescence (PL) intensity after the dry etch and after a succeeding wet etch with H_2SO_4. A comparison, figure 4.14, shows that the PL-intensity is almost unchanged for the different treatments for a large part of the wafer. Comparing the PL-intensity map with a map of the ridge height shows a very good agreement. The parts of the wafer where the etch has gone into the quarternary waveguide have a substantially lower PL-intensity. Since the wet etch does not remove quarternary material (or at least with a rate lower than we could measure), any damage in the quarternary waveguide will not be removed.

4.3 Results

4.3.1 MORIE

The first cyclic MORIE test etches gave undesirable horisontal surface roughness. A lowering of the bias (through a lower RF-power, 100W to 60 W) from 560 V to 430 V gave a smooth surface. By lowering the power, the etch rate was also affected in a negative manner, dropping 38 %. Therefore the methane content was increased from 20 % to 25 % of the hydrogen content. With that etch it was possible to dry etch 1.9 μm deep ridges with little inclination of the ridge sidewalls and smooth horisontal surface with only a 110 nm thick glass mask.

However the grating was not as good. The 120 nm openings of the second order grating had severe microloading effects (more than 600 nm over the ridge level) and was discarded as a possible solution. Second order gratings with 360 nm openings

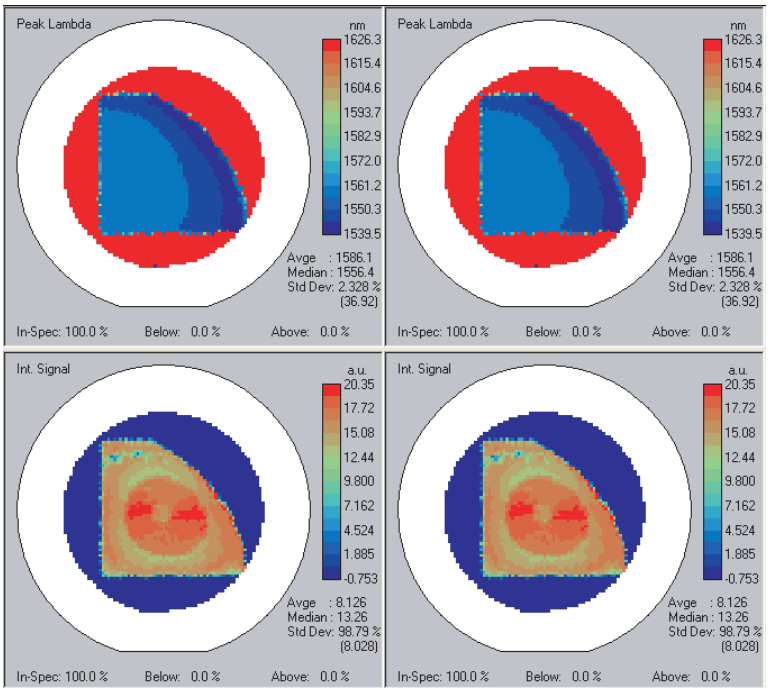

(a) before wet etch (b) after etch

Figure 4.14: Photoluminescence intensity maps of the laser wafer before and after wet etch in sulfuric acid.

and 120 nm pillars were also written by e-beam lithography but the dose used for the other gratings (with 360 nm spacing between lines) was too high and there was no time for another dose optimisation. The third order gratings with 360 nm openings and 50 % duty cycle also suffered from microloading effects. The etch depth inside the grating was about 300 nm less than outside the ridge for a 2 μm high ridge in InP, see figure 4.13. The etch depth uniformity was another issue. At a pressure of 80 mT the non-uniformity was 8 % (max to min), see table 4.6, corresponding to 170 nm at an average etch depth of 2125 nm. To decrease both loading effects the total pressure was lowered to first 50 mT and later 25 mT. With decreased pressure followed a higher bias and lower etch rate. In addition, the total flow also had to be changed because the turbo pump was too small to maintain the lower pressure with the same flow. To keep the bias constant the RF-power was lowered. Both these changes had the effect to decrease the etch rate. Therefore the thickness of the glass mask had to be increased to 200 nm to withstand the longer etch time. The chamber parameters and the etch rate for the final etch are given in table 4.7, while a SEM micro graph of a ridge etched at 25 mTorr is shown in figure 4.15.

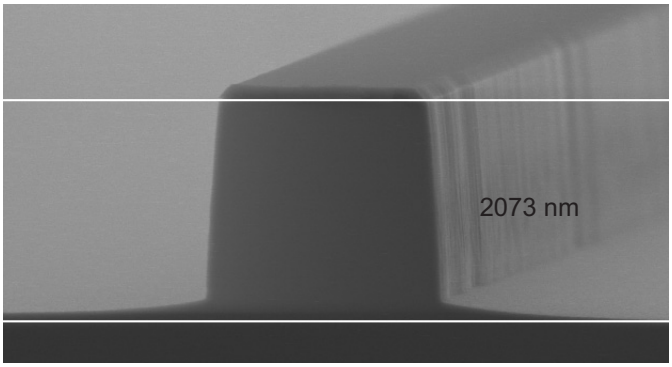

Figure 4.15: Dry etched InP ridge. The erosion of the glass mask is responsible for the small angle of the ridge wall, while the pedestal is due to loading effects as discussed earlier.

Table 4.7: Chamber parameters (settings), the bias and the etch rate for the final MORIE.

RF-Power (W)	Power density (W/cm^2)	p (mTorr)	F (sccm)	CH_4/H_2 (%)	Bias (V)	R_{InP} (nm/min)
43	0.14	25	26.5	25	430	22

4.3.2 Laser processing

This section gives information on some of the particular process details that I find could be interesting to the reader, in order to understand the final result of the wafer that was processed for laser fabrication. A general description of the complete process is given in appendix C.

A quarter of a wafer with the MMLLSOA3-epitaxy was covered with 220 nm glass, functioning as the mask for the ridge and grating. 530 nm electron beam resist (ZEP) was then spun on, and third order gratings with 50 % duty cycle were made with e-beam lithography. The designed opening was 300 nm instead of the calculated 364 nm, because test wafers showed a larger opening than designed for. Glass-RIE for the definition of the gratings was performed for 11.5 min (which was the time for the reflectometer to become constant plus 4 min, i.e 100 nm over etch). The ZEP-thickness was measured to 50-200 nm (edge-center) with a stylus profilometer. The ZEP was removed and UV-resist was spun on to a thickness of 600 nm. This resist fell off during this particular development and the reasons for this are still unclear since it had not happened previously with the test wafers. However the difficulties with the UV-resist led to resist leftovers in the part of the gratings outside the ridge, and might be a reason for extra loss. In the next step the ridges were defined through a glass RIE (11 min). The resist height was measured to 170-200 nm after the etch. The etching of the epitaxial layers was performed in three steps with two different etches. First a "high" pressure etch consisting of 12 cycles (30 min) was used to etch through the contact layers, table 4.8. Then a second etch of 20 cycles, with the parameters given in table 4.7, was performed to calculate a reliable etch rate (this is critical since etch rate vary with chamber condition). The third and final MORIE was timed from the calculated etch rate and was 12 cycles long. The etch depth measured with a stylus profilometer was 2250 ± 80 nm, but the profilometer measures several micrometers away from the ridge where the etch depth is around 100 nm less than at the ridge. A fully processed and mounted laser chip is shown in figure 4.16

Table 4.8: Chamber parameters and resulting bias for the contact layer etch.

RF-Power (W)	Power density (W/cm^2)	p (mTorr)	F (sccm)	CH_4/H_2 (%)	Bias (V)
60	0.19	80	42.1	25	430

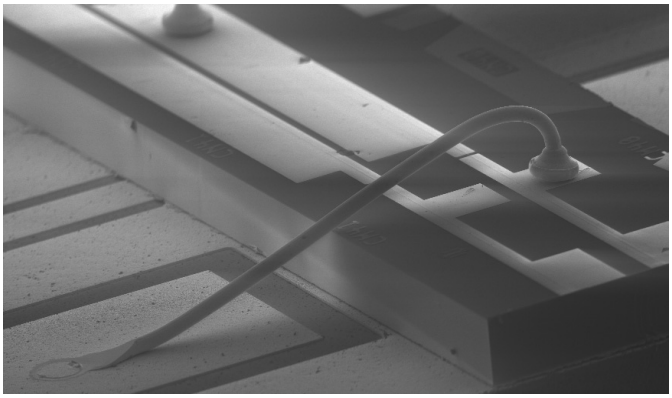

Figure 4.16: Fully processed and mounted laser chip.

4.3.3 Improvements

Several improvements can be made with respect to the current MORIE etch. The most straightforward ones involves the epitaxial design of the wafer material. Growing a thin Al-containing etch stop layer above the waveguide would decrease the micro (bumps in grating) and macro (non-uniformity over wafer) loading effects. After the MORIE, the Al-containing material can be selectively wet etched in phosphor acid to obtain a uniform etch depth. This will also improve the crystal quality by removing ion-induced damage in the surface. The current laser design has a rather high ridge to reduce losses from the highly doped contact layers and more importantly to reduce the pad capacitance. However, the current height is based on the older SCOOP-epitaxy, where the mode of the contact layer was much more similar to the waveguide mode. Thus reducing the height of the MMLLSOA3-design with 300 nm could improve the grating without affecting the loss greatly. The higher capacitance for 10-GHz lasers will also be acceptable.

The DBR-design can also be changed to provide larger openings: fourth order gratings with 600 nm openings and 360 nm pillars would decrease the microloading, with only 8 % decrease in the reduction factor or the gratings compared to the third order gratings.

4.4 Post-processing

4.4.1 Mounting

The lasers are cleaved into bars with 6 pairs of lasers on each. The total chip lengths, the absorber lengths and the grating lengths are given in table 4.9 for the cleaved lasers. All lasers are soldered n-side down on AlN high-speed laser mounts. Some of the absorber sections were bonded to a coplanar 50-ohm matched transmission line on the laser mount for active modulation.

Table 4.9: Laser lengths for fabricated DBR and FP lasers.

Laser	L_{tot} (μm)	L_{DBR} (μm)	L_{abs} (μm)
DBR 1 CM41-46	4390	80-120	90-110
DBR 2 BT41-45	4412	145	80-100
FP	4412	0	80

4.4.2 Coatings

Two coatings are used: a high reflective (HR) coating on the absorber facet and an anti-reflection (AR) coating on the grating facet. The HR coating is composed of a trilayer of $SiO_2/Ag/SiO_2$ (1500/1000/1000 Å) and yields a reflectivity of about 98 % over the entire gain bandwidth of the gain material. The AR coating is composed of a bilayer of SiO_2 and TiO_x. A reflectivity on the order of 10^{-4} is readily achieved. The coating materials are deposited in an e-beam vacuum chamber (physical vapour deposition).

Chapter 5

Characterisation

This chapter will present measurements on several different types of monolithic mode-locked lasers. 10-GHz lasers with DBR-gratings will be compared with FP-lasers of the same epitaxy. 10-GHz QW-lasers with different number of wells will be compared, and finally 40-GHz lasers with different active material will be compared: QW-lasers with 1, 2 and 3 wells and QD-lasers. But first we will take a look at the characterisation of the fabricated gratings themselves.

5.1 Characterisation of gratings

5.1.1 Electrical characterisation

IV The series resistances, R_s, of amplifier sections with and without gratings were calculated from IV-measurements as the derivative dV/dI above the diode onset. For an ideal conductor the resistance is given by

$$R_s = \rho\frac{d}{A} = \rho\frac{d}{wl} \tag{5.1}$$

where ρ is the resistivity (here it represents an average resistivity of several materials), d is the thickness and A is the area of the conducting material. Since the grating reduces the effective area of the metal/semiconductor interface (where most of the resistance relies), we should expect an increase of the series resistance proportional to the area reduction. By design half the area should be left after etching. Since the measured devices had different lengths a property independent of the length, $R_s l$, was calculated. Doing so, the $R_s \cdot l$ for a section without a grating was found to be 3500 +-300 $\Omega\,\mu m$, while the grating had a value of 12-20 $k\Omega\,\mu m$. The resistivity, the thickness and the width is the same for the two types of devices, which implies that the effective length of the epitaxial contact layers is 4-6 times smaller than for the structure without the grating. Comparing this result to the actual achieved duty cycle in the contact layers, about 100/720 nm (see figure 4.12b), we find that the measured resistance in the gratings correlate well.

Intersection resistance The resistance between neighbouring sections were measured with a multimeter to about 3 $k\Omega$, which should be enough for isolation.

Threshold current density The threshold current density is a good measure of the total loss (including mirror losses) in the laser cavity, and achieving low cavity loss and thereby low spontaneous emission was earlier pinpointed as one of the most important things to achieve low noise. The thresholds current of DBR-lasers with varying lengths (1 and 4 mm) were measured before coating of the facets and compared to lasers without any grating from the same laser bars, figure 5.1. The thresholds were very similar for lasers with and without DBR (sometimes even lower for the DBR). Since the length of the DBR is only between 2.5 and 10 % of the total length, a moderate extra loss in the grating doesn't influence the total loss very much. The variations in threshold is probably due to extra loss because of the problems with removing resist, as discussed in section 4.3.2. The threshold current density is 1.045 kA/cm^2 for 1 mm devices and 0.34 kA/cm^2 for the 4 mm.

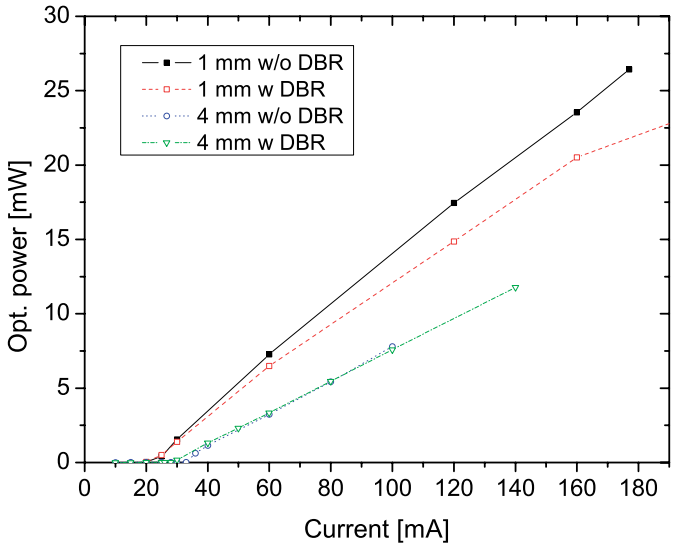

Figure 5.1: LI-curves for uncoated lasers, 1 and 4 mm long. Power measured with Large Area Detector.

5.1.2 Optical characterisation

Reflectivity and bandwidth SOAs with 7 degrees angle (facet reflectivity is a few percent) were cleaved and AR-coated, (R$\sim 10^{-4}$) in order to measure the grating reflectivity from ASE-spectra, but no dip could be seen in any of the spectra. This could indicate that the reflectivity is very low. In order to evaluate the gratings properly a more advanced reflection measurement scheme is necessary. Since we expect the reflection from the grating to be modest it's possible to use methods developed for evaluating AR-coatings. One such method relies on the measurement of sub-threshold ASE spectra from both the coated and uncoated facets. Our method is based on [93], and in short one measures the modulation depth of the FP-modes vs. wavelength from both facets. The reflectivity of the as-cleaved facet

is known and is 32%. The coupling ratio is unknown but can be estimated with the following arguments: 1) the ratio is nearly independent of wavelength and 2) is equal to the ratio of spontaneous emission at wavelengths well below the bandgap (long wavelength side) [30].

Two laser bars with different lengths, 2 and 4 mm, were AR-coated for the measurement of the reflectivity. One laser from each bar were measured with the described method. The current threshold was 42-45 mA for the coated 4 mm long laser (CS56b), while it was above 90 mA for the 2 mm long laser (CX53b). The length of the grating was 80 μm for the 4 mm device and 145 μm for the 2.2 mm long laser. Sub-threshold spectra from the 4mm laser can be seen in figure 5.3, while the calculated grating reflectivity for the 2.2 mm laser is plotted together with the single-pass gain in figure 5.2. The same reflectivity, 1%, is retrieved from all three sub-threshold measurements (50, 70 and 90 mA) on the 2.2 mm laser, while the gain increases from 9 to 12 dB. For the longer device with the shorter grating the peak reflectivity is also 1% but the side peaks are higher in this case. The FWHM bandwidth varies between 1.5 and 2.0 nm for decreasing current from 90 to 50 mA.

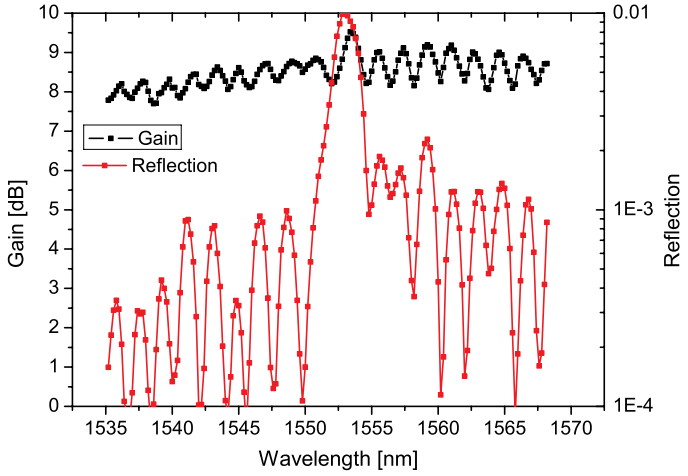

Figure 5.2: Retrieved reflectivity and single-pass gain from laser CX53b with 50 mA current (Length is 2.2 mm and the grating length is 145 μm).

ASE and laser spectra The gain peak of the lasers shifts somewhat with the two types of coating applied, and also varies over the quarter 2"-wafer. It also shifts with the length of the laser. The wavelength of the gain peak (table 5.1) correlate well with the PL-wavelength map of the wafer (figure 4.14), and depends mostly on thickness variations of the quantum well. The variation of the DBR-peak is much smaller than the gain peak variation (4 nm compared to 15 nm), and is attributed to the variation in effective index, which in turn is dependent of the variation in etch depth and growth thickness variation (which should be small

because of a rotating susceptor). 4 nm corresponds to a variation of less than 0.3 percent, which is 10 times less than the measured depth variation in chapter 4. However this can at least in part be explained by the fact that the measured lasers are not spread out over the entire wafer.

Table 5.1: Wavelengths for DBR-peak and gain peak (of uncoated laser) from different coordinates on the wafer. The closer the position is to the wafer edge, the greater is the etch depth and the smaller is the refractive index that governs the DBR-peak ($\Lambda_m = \lambda_B m/\overline{n}_{ave}$).

pos	device length [mm]	DBR-peak [nm]	gain peak [nm]
1	4.3	1551	1575-1580
2	4.3	1553	1565-1570
3	1	1551	1555
4	4	1553	1565-1570
5	2.2	1555	1565

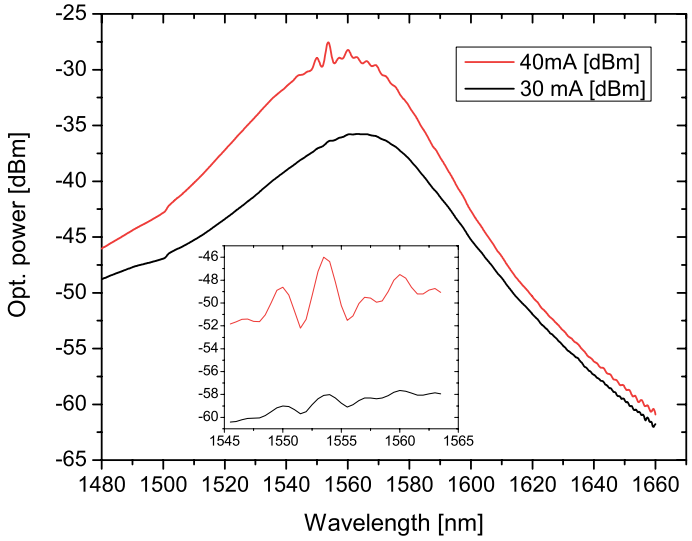

Figure 5.3: ASE spectra at two different biases below threshold for a 4 mm long AR-coated DBR-laser (CS56b). Grating length is 80 μm. Inset is a zoom-in on the peak with a higher resolution.

For lasers as long as several mm, the total gain is enough to make the DBR-lasers lase on more peaks than the central if not AR-coated (especially since in most cases the gain peak doesn't overlap with the DBR-peak). Figure 5.4 presents the output from a 2 mm long laser before and after AR-coating of the grating facet.

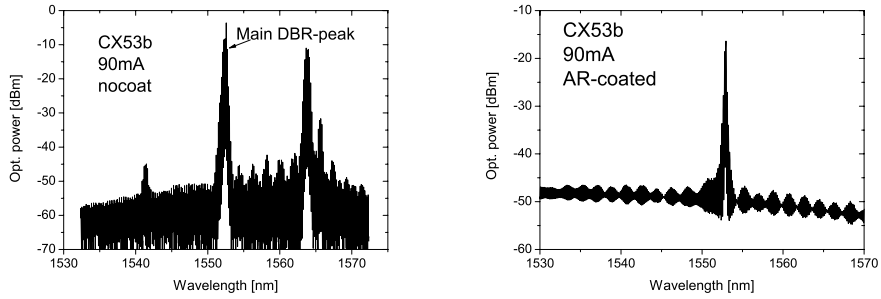

(a) Uncoated laser (b) AR-coated laser

Figure 5.4: Laser spectra from 2 mm long DBR-laser (CX53b) before and after AR-coating. The grating length is 145 μm. Bias is 90mA.

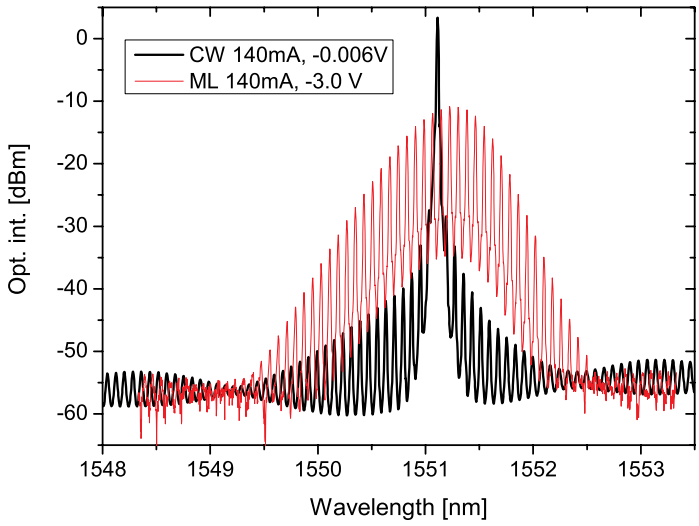

Figure 5.5: Comparison of CW spectrum and mode-locked spectrum for one of the DBR-MMLL, device BT42a (10 GHz).

5.2 Characterisation of mode-locking performance

This section presents comparisons of the mode-locking performance from several different monolithic MLLs. Noise measurements on the same lasers are grouped into a separate section. I will start with the mode-locked performance of the fabricated DBR-lasers along with the performance from the reference FP-laser without grating, but from the same wafer.

Passive mode-locking could be performed on all working lasers from the DBR wafer. Complete maps of the mode-locking area (gain current, absorber voltage) were not produced because of lack of time. However operating the lasers at approximately twice the threshold current seemed to produce reproducible and good results. With this gain current all lasers started mode-locking when the absorber bias exceeded approximately -2.2 V. Figure 5.5 shows the spectra for the same DBR-laser below and above the mode-locking absorber bias. The passive mode-locking performance of several DBR-lasers (from two different bars) have been measured with very similar results. Hybrid mode-locking has been performed on only two of the DBR-lasers because of lack of time.

LI for the compared DBR and FP mode-locked lasers The LI-curves for the coated DBR laser and reference laser are shown in figure 5.6. The FP-laser has a 5 % AR-coating, which explains part of the lower threshold (the uncoated threshold values were 31 mA for the FP-laser and 32-35 mA for the DBR laser, at 20 degrees Celsius). The thresholds of both lasers directly after coating were lower than the values given in figure 5.6, 40 and 57 mA respectively, but degraded after operation. The threshold degradation was partly recovered by heating the lasers to 50 degrees Celsius for several hours. The AR-coatings have been known to absorb water vapour when cooling the laser to below room temperature (25 degrees Celsius). Output powers from the lasers are similar.

5.2.1 Spectra and pulse width

10-GHz DBR lasers Passive mode-locking with high fibre coupled power and short pulses were seen from all tested DBR-lasers. The fibre coupled power of course varied with the coupling, but was generally only 3 dB lower than the CW-lasing power at the same gain current. This means a fibre coupled power of about 5 mW which is almost 30 times higher than for the 10-GHz DBR-MMLL in [18]. If we assume a 3 dB loss into the fibre the output power is 10 times the power reported for the 10-GHz laser in [58]. The passive spectrum of the DBR-lasers is quite close to a Gaussian but for most operating conditions with a small skewness, such that the high-energy side is somewhat broader than the low-energy side. The side-peaks of the filter were around 40 dB down (figure 5.5). Passive spectral widths (FWHM) ranged between 0.5 and 1.0 nm depending on operating conditions. The transform limited pulse width for such a narrow spectrum is 3-6 ps, which clearly will limit how short pulses it's possible to produce with these lasers. The actual pulse width directly from the DBR-lasers was not transform limited. However, in principle all excess bandwidth could be linearly compressed in $\sim$400 m standard SMF (total dispersion of 6.8 ps/nm). The spectrum and autocorrelation for such a pulse train is shown in figure 5.7 and 5.8. The pulse width obtained from the autocorrelation for this particular laser and operating condition was 5 ps if fitted with a Gaussian.

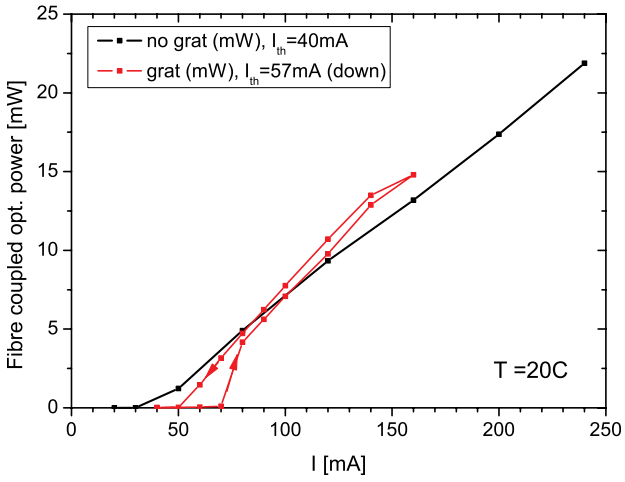

Figure 5.6: LI-curves of the compared 10-GHz DBR and FP lasers from the MMLLSOA3-design. Temperature is 20 degrees Celsius and all sections are biased together in forward.

The spectrum from the reference FP-laser is on the other hand far from transform limited, figure 5.9. As expected from earlier generations of FP mode-locked lasers the spectrum has much excess power on the high-energy side.

Active modulation of the absorber of the DBR laser was performed by applying a sinusoidal RF-signal from a synthesizer (RS SMR40), which was amplified with a 4-10 GHz electrical power amplifier (Cernex CBM041003030, gain 30 dB, P1dB: 30 dBm, NF 6dB). A 1 dB attenuator was placed after the amplifier for protection against reflections from the laser. No change in RF-spectrum could be seen after -8 dBm input. The conclusion should be that the gain is somewhat higher than the specified value and that we are already at 30 dBm output power at -8 dBm input. With the loss in the cable taken into account the maximum power delivered to the absorber was 28 dBm. However, a large part will be reflected (S11 measurements on other lasers at 10 GHz gave 40 % reflection).

To obtain short hybrid pulses with low noise the absorber voltage needed to be increased to -5-(-6) V (At 28dBm the peak-to-peak voltage swing is 15.9 V. If 50 % of this power is dissipated into the absorber then the voltage swing on the absorber would be about +-4 V). With the active modulation the pulses shortened somewhat, but since the the spectral bandwidth is limited by the grating width the shortest pulse was still 3.5 ps (after 400 m SMF). The spectrum became a little more skew than for passive mode-locking but the difference was not large and still fitted quite well to a Gauss. A FROG measurement was taken for what was considered the best operating condition and the retrieved spectrum and electric field is shown in figure 5.10 and 5.11. The FWHM TBP for this pulse was 0.34, and the shapes of the pulse and spectrum are close to ideal.

The reference laser was also hybrid mode-locked with short pulses and high

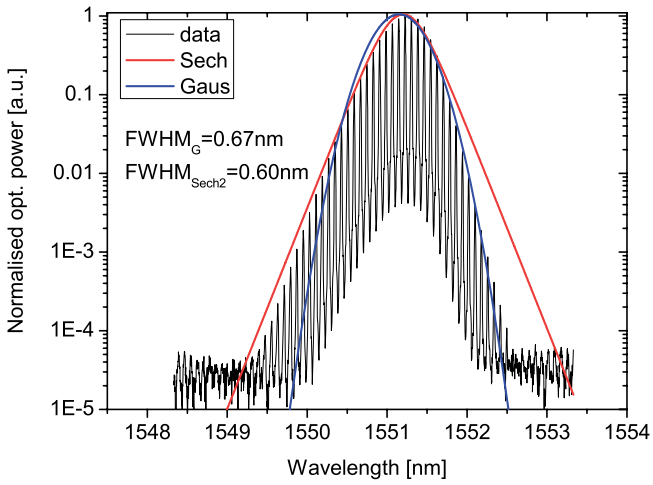

Figure 5.7: Spectrum for passive mode-locking of a DBR-MMLL. Gain current is 140 mA and absorber bias is -3.0 V.

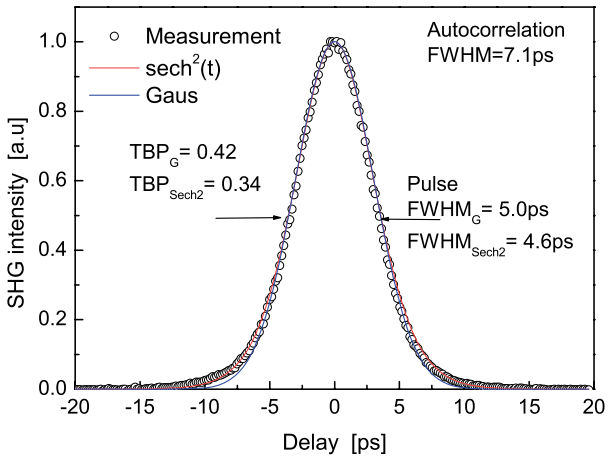

Figure 5.8: Autocorrelation for passive mode-locking of a DBR-MMLL. Gain current is 140 mA and absorber bias is -3.0 V.

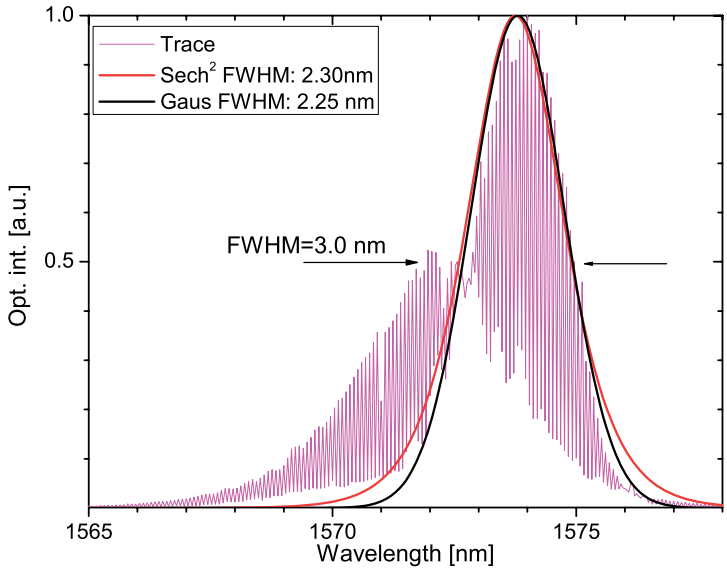

Figure 5.9: Spectrum for passive mode-locking in a FP-MMLL from the same wafer bar as the DBR-MMLL. Notice the different wavelength scale for this spectrum. Gain current is 80 mA and absorber voltage is -2.7 V.

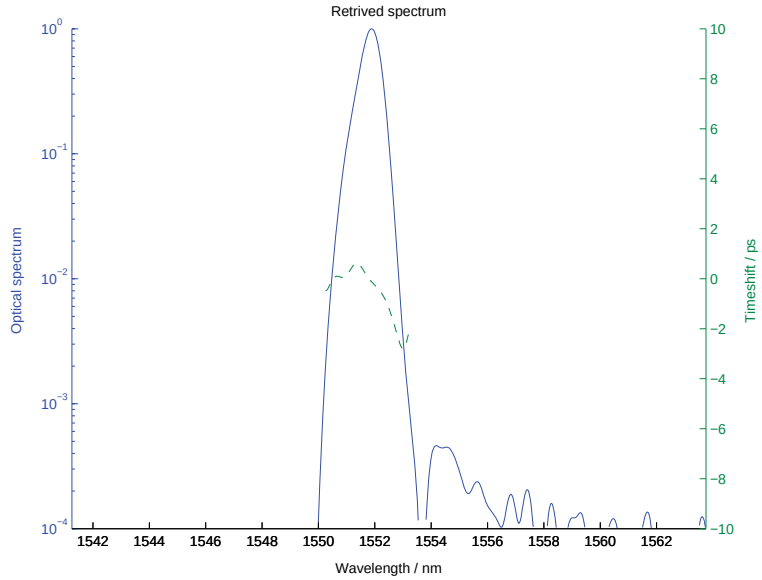

Figure 5.10: Spectrum of a hybrid mode-locked DBR-MLLL, retrieved from FROG-measurement.

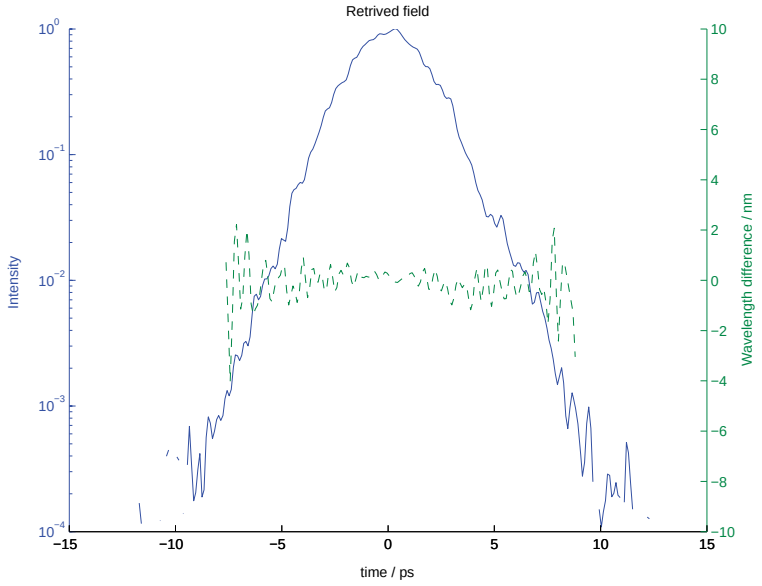

Figure 5.11: Field amplitude of a hybrid mode-locked DBR-MLLL, retrieved from FROG-measurement.

output power. No FROG could be produced from the reference laser since the wavelength was too far from the EDFA-window (which shows the importance of controlling the wavelength of the laser, e.g. with a DBR). An autocorrelation could be performed, and the result is shown in figure 5.12, together with the spectrum. Again the spectrum falls off poorly on the low wavelength side, which will limit the performance and the applications. The (uncompressed) pulse width, 2.1 ps if fitted with a hyperbolic secant, is comparable to results obtained on earlier wafers (SCOOP6) with wet-etched ridges [49].

The most important change for the DBR-lasers with modulation was the RF-spectrum, and measurements of timing jitter and RIN will be presented in section 5.2.2.

40-GHz QD and QW lasers The spectra of the measured QD and QW (SCOOP6_1) lasers were considerably different for most operating conditions. While the spectra for the 40-GHz QW-lasers (figure 5.13) have the same characteristic broad pedestal as the 10-GHz FP-laser spectra (especially for the low-noise operating conditions), the QD-laser spectrum (figure 5.14) falls off as something in between a Gaussian and hyperbolic secant for more than 3 decades. The reason for this has not been investigated, but the result is that the QW-lasers will require external optical filtering if to be used for multi wavelength fibre communication systems.

5.2.2 Noise characterisation

5.2.2.1 Measurement techniques for intensity noise

Time-domain (sampling scope) Intensity noise can be visualised and measured in the time-domain with a fast oscilloscope (sampling scope). The advantages

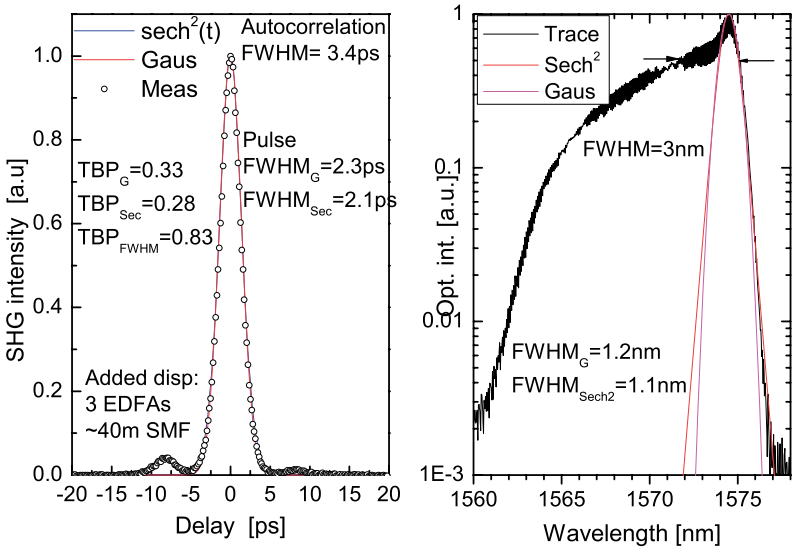

Figure 5.12: Spectrum and autocorrelation from hybrid mode-locking of a 10GHz FP-MMLL.

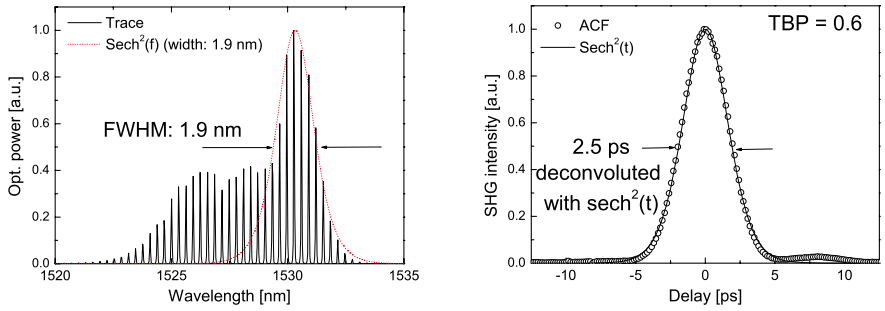

Figure 5.13: Mode-locked spectrum and autocorrelation from a 1 QW laser operating at ∼40GHz.

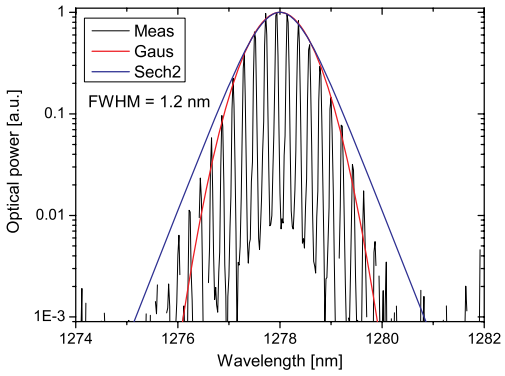

Figure 5.14: Passive mode-locked spectrum from a QD laser operating at ∼40GHz. Gain current is 75 mA and absorber bias is -5.6 V.

are that it's fast and easy to perform the measurement and that the time-domain is easy to understand. However the measurement is limited in resolution, which means that small noise levels cannot be accurately measured. Further on there's no information of the origin of the noise, which means that it's difficult to solve the noise problem if there is one.

Frequency domain (RF spectrum analyzer) As described by equation 2.7 the noise skirts around the delta functions from a perfect (actively restored) pulse-train are made up of a sum of amplitude and timing noise. However at $\mu = 0$, i.e. at baseband, the noise consists of pure amplitude noise. This baseband noise is usually measured as Relative Intensity Noise (RIN) [43] and is relatively easy to measure. There are complete systems for measuring RIN up to 22 GHz, such as the HP 70000 Lightwave Analyzer. This is our preferred method.

5.2.2.2 Measurement techniques for timing noise (timing jitter)

Three of the most common methods in the literature for determining timing noise are the sampling scope method, the phase-noise method and the optical cross-correlation method. This section will present the advantages and drawbacks of all the methods in short, but also a deeper analysis of the phase-noise technique, along with experimental data obtained with this method.

Sampling scope - Time domain Time domain measurements with a sampling scope (fast oscilloscope) offer fast and direct reading of timing jitter of a pulse in the time domain. The measured timing jitter is residual (difference between pulse and oscillator) since the clock is used to trigger the oscilloscope. The first drawback of this method is the high jitter of the sampling scope itself (arising from the trigger process), which makes it difficult to measure timing noise below 200 fs, which is the trigger jitter of the state-of-the-art sampling scope. The second drawback is the lack of frequency information about the noise. Thus no analysis

about the origin of noise can be made. A sampling scope measurement will not let us know if the noise is due to the noise from the RF-modulator or from laser spontaneous emission.

Pulse cross correlations - Time domain An optical cross-correlation is the correlation of a pulse with another pulse separated by a certain amount, say N, of round trips, $T = N \cdot T_R$, while the autocorrelation presented in chapter 2 is the correlation of the pulse with itself. The increased width of a cross-correlation compared with the autocorrelation is a direct measure of the timing jitter between the two pulses in a frequency range of approximately 1/4T to ∞ Hz and is given by [94]

$$\sigma_{pp} = \sqrt{\sigma_{XC}^2 - \sigma_{AC}^2} \tag{5.2}$$

where σ_{XC}^2 is the variance of the cross-correlation and σ_{AC}^2 is the variance of the autocorrelation. The technique is well suited to measure jitter between pulses close to each other (small delay or high frequency) and high-repetition rate lasers, since the delay length needed in one arm is $L(T) = c/n_g N \cdot T_R$. For a 10-GHz laser and 1000 round trips between the pulses the delay length in air is 30 m, which can be a practical problem. This is easiest solved by inserting a spool of fibre in one arm of the autocorrelator. To compensate for the broadening due to dispersion it is necessary to perform an extra autocorrelation measurement with the fibre spool inserted before the autocorrelator. In section 2.3 it was argued that for optical communication purposes the timing jitter should be integrated down to a bandwidth given by the clock-recovery low-pass filter. The jitter from a cross-correlation is integrated down to a bandwidth given by the delay $f_{low} = 1/4NT_R$ (taking the example of the 10-GHz laser and delay length of 30 m this corresponds to $f_{low} = 2.5MHz$. Such measurements, with up to 1000 m delay in fibre, have been performed by Jiang et al. [94] on both hybrid and passive mode-locked semiconductor lasers. From his measurements it could be seen that the passive jitter made a random walk (linear variance vs. time) and thus increased for increasing delay, while the timing jitter of the hybrid mode-locked laser was bounded by the restoring force of the electrical modulation, all in agreement with the theory [27, 41]. Jiang also compared his measurements to frequency domain measurements (see next paragraph) and found a good agreement.

Frequency domain (phase-noise) The so-called phase-noise method was first presented by von der Linde in 1986 [40]. Instead of measuring fluctuations in the time domain he measured the power spectrum of the light intensity (see section 2.2 for a theoretical treatment of his method). This frequency domain technique has many advantages, such as information about the origin of the noise, and a very low noise floor (high dynamic range). Timing jitter in the tens of femtosecond range can be obtained by this technique [39].

The pulse train is captured with a fast photodiode and the photodiode spectrum is processed with an Electrical Spectrum Analyzer (ESA). A schematic of the measurement set-up is given in fig. 5.15. The integrated noise skirts around the repetition rate peaks are directly proportional to the total noise due to amplitude and timing fluctuations (jitter) as outlined in chapter 2, section 2.2. To separate the two contributions, one should ideally integrate the noise around several peaks,

since the timing noise increases with the harmonic number squared, equation 2.7. This can be a tough technical task for high-repetition rate lasers at 10 GHz and especially at 40 GHz. However, assuming that the amplitude noise is low compared with the timing noise, we can make an upper limit measurement of the timing jitter by simply integrating the noise skirts around the fundamental frequency. This is what we do.

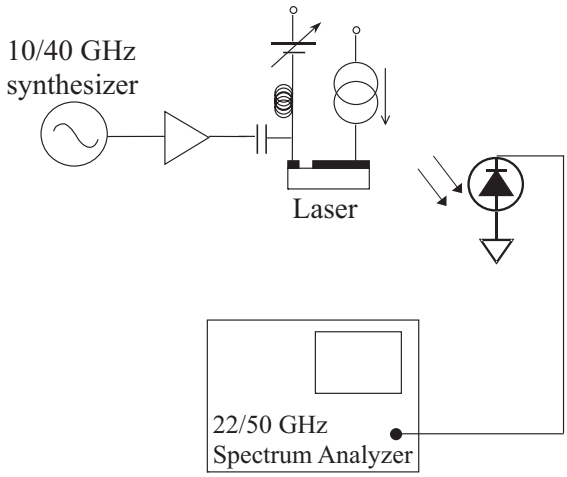

Figure 5.15: Absolute (direct) phase-noise set-up.

A note on Electrical Spectrum Analyzers: The processed ESA spectrum is not equivalent to the power spectrum of our laser. This is because the spectrum analyzer is calibrated to measure narrowband peak signals. When broadband noise is the signal, a correction of +2 dB needs to be added [95]. Peaks, such as the fundamental and harmonics of the repetition rate and spurious peaks from RF-pick-ups should not be corrected. Except for this correction the measured noise skirts are directly related to the desired power spectrum, S_F, and thus to the timing noise spectrum, S_J. Since the measurement technique originates from microwave noise measurements, we use some of the notation from it also, such as the Single-sideband (SSB) phase-noise spectral density $L(f)$, defined as the ratio of the measured phase-noise (timing noise is called phase-noise in microwave literature since the phase is related to the time by $\phi = \omega t$, and $\Delta\phi = \omega\Delta t$) in 1 Hz, $P_n(f)(1Hz)$ to the total carrier power, P_c at an offset frequency f.

$$L(f) = \frac{P_n(f)(1Hz)}{P_c} \tag{5.3}$$

The timing spectral density and phase noise spectral densities are related through $S_J = \left(\frac{1}{2\pi f_R}\right)^2 L(f)$ with f_r being the repetition frequency. The RMS timing jitter is given by (see equation 2.9 also)

$$\sigma_{rms}(f_{low},\, f_{high}) = \frac{1}{2\pi f_R}\sqrt{\int_{f_{low}}^{f_{high}} (L(f)_l + L(f)_u)df} \tag{5.4}$$

Integrating both the upper, L_u, and lower, L_l, sidebands will reduce the sensitivity to any amplitude noise, since it adds on one side and subtracts on the other [41, 43].

Integration ranges The measured phase-noise level (power spectrum) can be converted to RMS timing jitter by equation 5.4. The full timing jitter is obtained by integrating to infinity (over all times!) but is not very practical when making a measurement. Von der Linde decomposed the noise spectrum into a low frequency part and a high frequency part and integrated by taking the maximum noise level times the 3 dB bandwidth of the low and high frequency parts. Historically a very common integration range is 100 Hz to 10 MHz. However, it's extremely uncommon that authors comment on why they have chosen a certain integration range. Choosing an integration range also means choosing what noise not to include in the measurement. Of course the upper range might be limited by the equipment you use (and then that should be stated), otherwise a good way of choosing range is by the application. A long integration time means that low frequency jitter is important and vice versa. As the lasers described in this thesis are intended for telecom applications we must consider the following: 1) when used as a transmitter the laser's own noise will always be lower than that of the electronic modulator at low frequencies, 2) when used in clock-recovery the laser/CR-circuit can follow slow jitter and cancel it. In both these important applications for mode-locked lasers the high frequency jitter is important. For sampling applications everything up to the Nyquist frequency will count [25]. Measured timing jitter in this thesis is presented according to the recommended integration ranges for electrical clock-recovery given by the International Telecommunication Union in G.8251.

Table 5.2: ITU-T jitter measurement filter ranges for electrical CR [38]. Ranges in Hz. Multiplexing a 10-GHz laser four times to 40 GHz, results in a multiplication of the jitter range also by 4.

Line rate	Range 0	Range 1	Range 2	Range 3
10 GHz	<20k	20k-80M	4M-80M	80M-5G
40 GHz	<20k	20k-320M	16M-320M	320M-20G

5.2.2.3 Measurements of noise in mode-locked lasers

10-GHz QW-lasers with different number of wells Long monolithic mode-locked lasers have long been thought to have higher intrinsic jitter than their external cavity counterpart, because of their higher cavity loss [47]. However this is not a physical limitation, but rather a limitation of the design. While waveguide losses in [47] were around 7.5 cm^{-1}, waveguide losses of 2-3 cm^{-1} [30] can be achieved by lowering the number of quantum wells. These measurements serve to corroborate the low-noise design of the active material originally presented by Yvind [96] and summarised in chapter 3 in this thesis. The two measured lasers have an approximate repetition rate of 10 GHz and are 4.25 mm long. They have the same epitaxy (SCOOP6, see chapter 3) except that they have one or two QWs. The lasers are hybrid mode-locked by modulating the reversed biased absorber, in this case with the amplified signal from an HP8673C synthesizer. The pulse train is detected with a 22 GHz HP Lightwave section integrated in the HP70000 Lightwave Analyzer, also comprising the ESA (Figure 5.15).

Three measurements of phase-noise of mode-locked lasers are presented in figure 5.16. One of an AR-coated 2-QW laser and two of a 1-QW laser with and without AR-coating (AR-coating is 5 % in this case). A measurement of the synthesizer noise is also included. For frequencies lower than 1 MHz the measured noise is entirely given by the transferred synthesizer noise, while the noise floor is met after a few hundred MHz. From the data between these frequencies it is clear that as expected from the design considerations (ch. 3) the 1-QW devices exhibit less noise than the 2-QW laser.

Integrating the jitter according to our earlier specified telecom ranges for 10 GHz (20k-80M), the jitter is 81 fs for the AR-coated 1-QW laser and 110 fs for the 2-QW laser. Now, as stated earlier, comparing jitter values might be difficult because of changing ranges. However comparing the white noise plateau with earlier results on semiconductor mode-locked lasers we find that the values for all three lasers are record low (2-QW: -125 dBc/Hz, 1QWs: -130dBc/Hz) even when compared with external-cavity lasers, which were supposed to have lower noise than monolithic lasers due to low loss in the external cavity. The lowest phase noise plateau value for an external-cavity laser to date and to our knowledge is at -123 dBc/Hz reported in [97].

Comparison of DBR-laser and FP-laser at 10 GHz The same set-up is used as described in the preceding paragraph, except the synthesizer is now a Rhode&Schwartz SMR40, since the HP8673C was not available at the time of the measurement. This synthesizer has a somewhat worse noise level, meaning that the integrated timing jitter will be worse, but hopefully the high-frequency noise spectrum can still reveal some information about the intrinsic laser noise. As can be seen in figure 5.17 the synthesizer contributes to a lot of low-frequency jitter. The absolute jitter for the DBR-laser is 250 fs while the jitter is 187 fs for the reference FP-laser. If we can imagine that we can reveal the intrinsic low-frequency spectrum of the lasers by a residual measurement (see paragraph) then a -120 dBc/Hz plateau, as is the case with the DBR-laser, corresponds to 142 fs. The DBR-plateau is higher and drops off later than for the FP-laser, which would be contradictory to the design rules presented in chapter 3. The explanation lies in the strength (or rather weakness) of the grating.

The grating reflectivity which was calculated to be over 10 % in chapter 3, was measured in section 5.1 to be 1%. Compared with the 5% reflectivity of the FP-laser this has implications for the noise: the losses increase and thus the threshold increases, which in turn increases the spontaneous emission level, P_{ASE}. The grating also introduces extra loss because of radiation modes and extra waveguide loss introduced by the incomplete removal of the UV-resist in the grating beside the ridge during the processing. The threshold of the DBR-laser was 57 mA (shown in figure 5.6) but had some hysteresis, while the threshold of the FP-laser was 40 mA (figure 5.6). Somewhat lower phase-noise spectra ($\sim$-125dBc/Hz) could be achieved with the DBR-type lasers but at the cost of longer pulses, and are thus not presented here. A comparison of the passive and hybrid RIN of the DBR-lasers and FP-laser can be seen in figure 5.18 and 5.19.

In summary, a comparison of the results on the DBR-lasers with earlier reported 10-GHz DBR MMLLs with a wavelength close to 1550 nm is quite favourable. The first reported long monolithic cavity mode-locked laser with an integrated DBR was by Hansen et al. [65]. The repetition frequency was 8.1 GHz and transform-

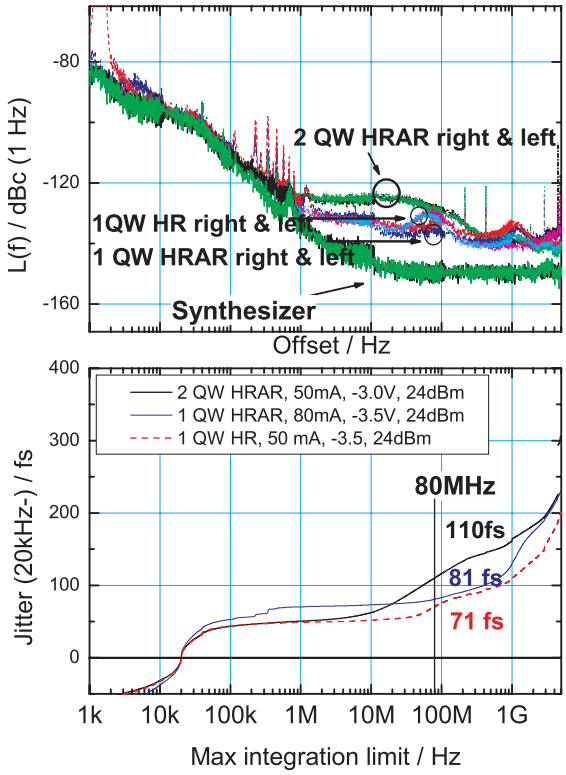

Figure 5.16: Single-sideband absolute phase noise spectrum and integrated timing jitter for 10 GHz all-active lasers. The SSB of the synthesizer is also added.

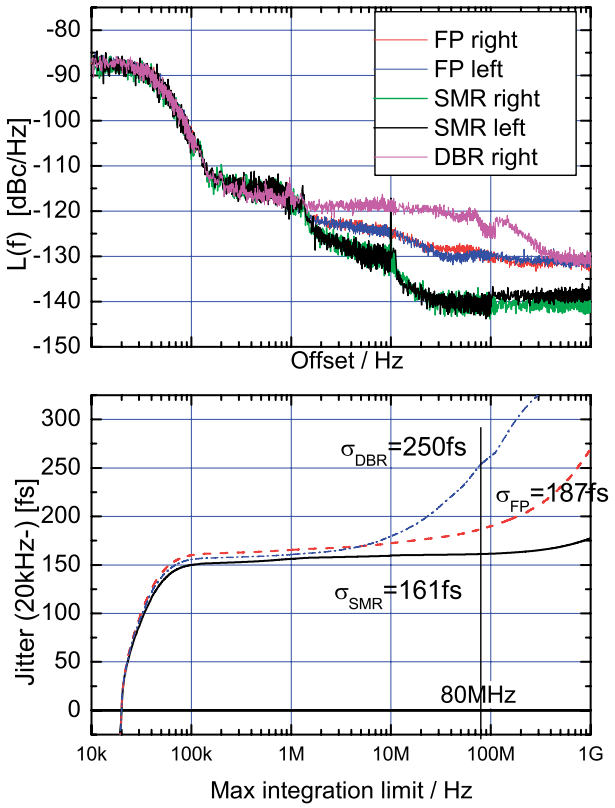

Figure 5.17: Absolute phase noise spectra and integrated RMS timing jitter for DBR-laser, FP-laser and the driving synthesizer (R&S SMR40).

limited pulses of 20 ps duration was produced. Neither the output power, nor any noise level were reported. The laser of Weber et al. [58] had a repetition rate of 9.95 GHz with a TBP less than 0.4 ($sech^2$-shaped pulses were assumed). The pulses were above 8 ps and the average output power was 1 mW. Finally, Ogura et al. [18] obtained 6.1 ps $sech^2$-shaped pulses with a TBP of 0.38 and a fibre-coupled output power of 0.18 mW. The timing jitter was stated to be 0.3 ps but without stating measurement method or integration interval. The measured noise level of the fabricated lasers in this project is lower than in [18], while the (linearly compressed) pulses are shorter than in all the references, and the output power about ten to thirty times higher than in [58] and [18]. All the references use one of the techniques described in section 3.2.2 to make passive DBR waveguides. Considering the growth advantages of our laser it's even more favourable.

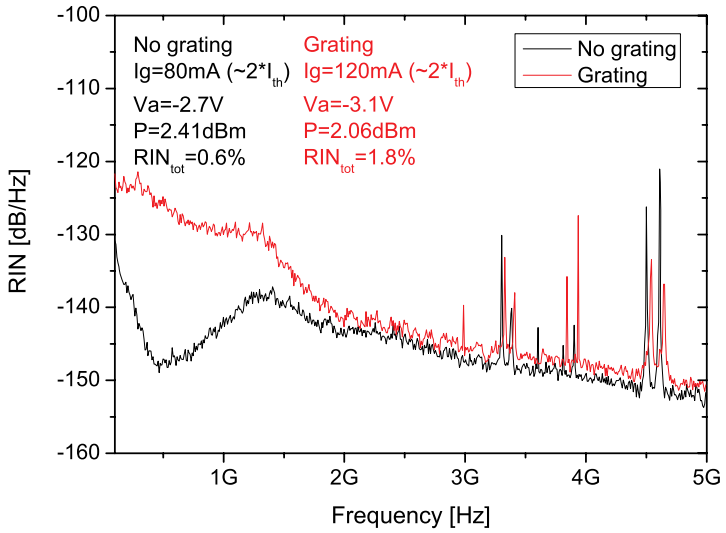

Figure 5.18: Comparison of RIN from passively mode-locked DBR-MMLL and FP-MMLL. Both are biased at approximately twice times the threshold.

Comparison of QD and QW lasers at 40 GHz Quantum dot lasers have received increased attention during the last couple of years. Several of the improved properties for such lasers fit well with the design rules for low-noise mode-locked lasers presented in chapter 3. Some of them are low differential gain when the laser is biased high above threshold, resulting in high saturation energy and little pulse shaping in the gain section. Low loss decreases the spontaneous emission noise and a low alpha factor decreases the chirp in the long gain-section. On the negative side is a lower absorption per length in the absorber, because of a lower confinement factor and reduced quantum confined Stark effect (QCSE), which results in long absorbers. This decreases the effectiveness of a self-colliding pulse effect (HR-coating) and increases the capacitance of the device resulting in

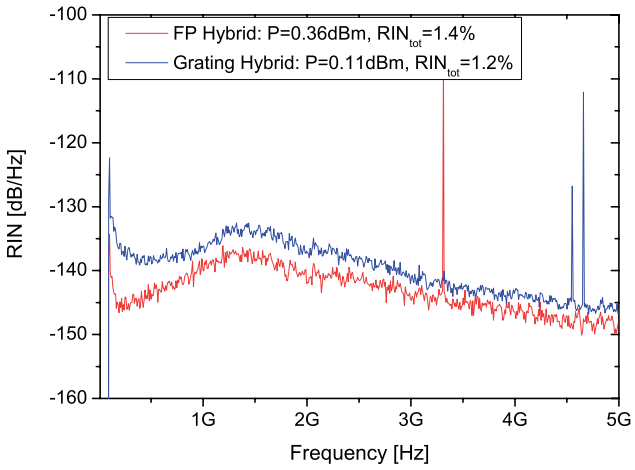

Figure 5.19: RIN spectra from hybrid mode-locked 10-GHz DBR and FP lasers.

lower bandwidth and hence lower modulation when hybrid mode-locked. The lower QCSE also decreases the modulation capability. Here we compare a 40 GHz QD-laser with a 40 GHz QW-laser. Both lasers are about 1 mm long and are all-active with the same material in the gain and absorber sections. The QW-laser has the SCOOP6 epitaxy (chapter 3). The QD-material is grown on an GaAs-substrate using Molecular Beam Epitaxy. The active region consists of a ten-fold stack of identical $In_xGa_{1-x}As$ QD layers in a GaAs waveguide and $Al_{0.35}Ga_{0.65}As$ cladding layers. The laser has an emission wavelength of ~1280 nm. Being aware of the differences other than the dimension of the grown material, we would still like to do a comparison of the two lasers. Both lasers have HR-coated facets for a self-colliding pulse effect, while the output facets are as-cleaved. The length of the absorber is 100 μm in both cases. They are mounted and bonded in the same manner.

The threshold current of the QD-laser is 30 mA when only the gain section is biased, while the threshold of the all-forward QW-laser is 7 mA. But since the ridge of the QD-laser is 3 times wider (6 μm) the threshold current densities are quite similar (350 and 500 A/cm^2) especially if we take into account the extra loss introduced by the unbiased absorber. Now that we have the background facts we are ready to have a look at the noise measurements. Operating conditions were quasi-optimised for low phase-noise from looking at the RF-spectrum while changing the parameters (however no complete systematic log of noise vs. operating conditions was made).

Figure 5.20 shows the passive mode-locking RF-spectra of the QD and 1-QW lasers, while the operating conditions are given in table 5.3. It's clear that the noise skirts around the QD-laser are much lower than in the 1-QW case.

Looking at the passive SSB-spectra, 5.21, we find that both lasers drop off with a 20 dB/decade, in perfect agreement with theory [41], however with a 20 dB difference in the magnitude until the QD laser meets the noise floor (which is higher for the QD laser because of the lower average power). Integrating the measured

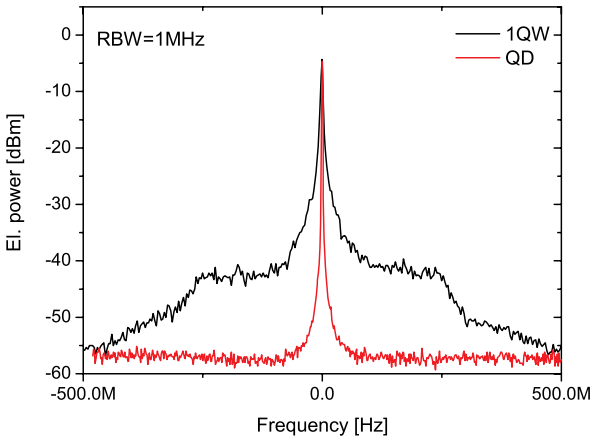

Figure 5.20: ESA-trace with fundamental peak and noise skirts for passive mode-locked 40-GHz QD-laser and 1-QW laser. To aid the comparison a vertical alignment of the peak values have been performed by shifting the QD-peak X dB.

curves in the ITU-T-specified band 16-320 MHz (see table 5.2) results in a timing jitter of 219 fs for the QD laser, about 6 times less than the 1.3 ps of the QW-laser. The jitter value for the QD laser is actually overestimated since the noise floor is met already at 100 MHz.

In order to understand why the QD laser is so remarkably better concerning the phase-noise we will go through the design for low noise again. Achieving a large pulse power at the same time as a low spontaneous emission will minimise the noise. The linear cavity loss is approximately the same for the two lasers (same threshold density), indicating that the spontaneous emission levels are similar. However QD-lasers tend to have higher inversion which reduces the spontaneous emission in comparison with the QW-laser. The pulse energy is in favour of the QW-laser since it is much higher at the particular measurement operation point (indicated by the measured average facet power of 20 mW for the QW-laser compared to 7 mW for the QD-laser), especially if one speaks about the pulse energy per area since the QD-laser is 3 times as broad as the QW-laser. The pulse saturation energy which is inversely proportional to the differential gain and the confinement factor would probably be slightly in favor of the QD-laser. This will lower the dynamic loss in the absorber since less pulse broadening is produced in the gain section. Finally the internal quantum efficiency also plays a role in this game by governing the carrier shot noise. Generally longer wavelength means more non-radiative radiation and lower efficiency. The internal efficiencies have not been measured. Potentially the alpha factor could be lower in the QD-SOA section but without measurements to prove it we cannot be sure about it. Unfortunately the above information doesn't lead to any real conclusion about the answer to the question. Detailed measurements of the above mentioned quantities should be undertaken in order to progress.

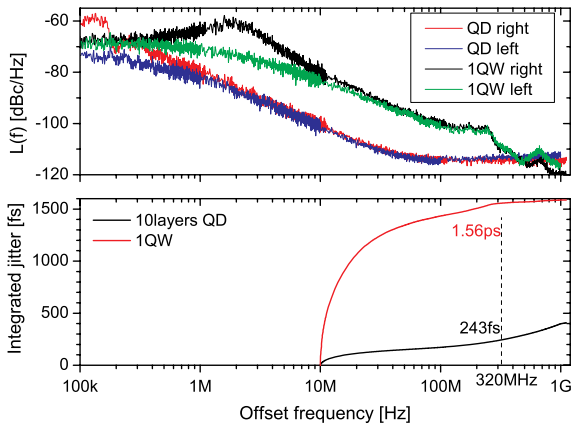

Figure 5.21: Absolute phase noise spectrum and integrated timing jitter for passive mode-locked 40-GHz QD-laser and 1-QW laser.

Table 5.3: Operating conditions for the passive mode-locked QD-laser and the compared 1-QW-laser.

Laser	I_g (mA)	V_a (V)	λ (nm)	$\Delta\lambda$ (nm)	P_{fibre} (mW)
QD	75	-5.6	1278	1.2	~ 1
1-QW	175	-2.7	1531	2.2	9

Hybrid mode-locking was also performed by modulating the absorber section of the lasers. The phase-noise and resulting absolute RMS timing jitter is presented in figure 5.22. Although the value of the jitter in the ITU-T specified range 2 (20kHz-320MHz) is low - 124 fs - it's clear that the phase-noise deviates earlier from the synthesizer noise than in the QW case. However, this is probably not only reflecting the choice of active material but more so the electrical modulation performance of the laser structure. In the QD-laser the absorber was not designed for high-speed modulation. A thin glass layer is used as passivation and results in a capacitance about ten times higher than the capacitance in the QW-laser. This high capacitance lowers the modulation bandwidth considerably. Taking this into account the hybrid timing jitter from the QD-laser is excellent and can be expected to be even lower with a high-speed design of the absorber.

Residual high-dynamic range phase-noise measurements (at 40 GHz)

Motivation and introduction Much of the content in this section is general and the methods and analysis apply for any residual measurement. However the specific set-up used here is for 40 GHz operation only and all the lasers that have been measured operates at a frequency between 39 and 40 GHz.

Residual timing jitter of a hybrid mode-locked laser is the jitter relative to the synthesizer and not relative to a perfect pulse train as in the case of the direct measurement. In comparison with the direct phase noise method, there are three important advantages of the residual method. The first is linked to the fact that today's mode-locked lasers can have inherent phase noise (timing jitter) values that are considerably lower than those for frequency tuneable synthesizers over many decades of frequency. In a direct phase-noise noise measurement the total noise is measured, including the transferred noise of the dc-source and the RF-oscillator. The effect of this is that noise originating from the laser itself might not be detectable. No laser improvements can be done based on such measurements. It will also be difficult to compare different lasers (especially if different synthesizers have been used). This is particularly true for low offset frequencies, say below 1 MHz (see figure 5.22). A way to get around this problem is to use electrical high-stability single frequency oscillators as RF-sources like [43, 97] do. This is possible if you have a large tuning range of the laser repetition frequency combined with an exact cleave length. If not our residual method is to prefer.

The second advantage is connected to the noise floor of the spectrum analyzer. Because of a finite noise floor of spectrum analyzers there is a limited dynamic range in an absolute measurement of the phase noise. This dynamic range must include both a high power signal (several actually in the case of short pulses) and the low power noise. The residual measurement shifts the signal to baseband, making it easy to filter the carrier now at DC (e. g. with a bias-T). Once we are left with only the (laser) noise at baseband we can preamplify it, and the dynamic range is now given by the possible noise power level and the combination of thermal noise of the electronics and the photodiode shot noise (see Appendix B for further details about the calculation of thermal and shot noise). The dynamic range usually becomes an issue at high frequency offsets, where the noise of the mode-locked laser usually drops of as f^2 (figure 5.23). The third advantage is that for the intended application of the laser, optical communication systems, the slow noise dominated

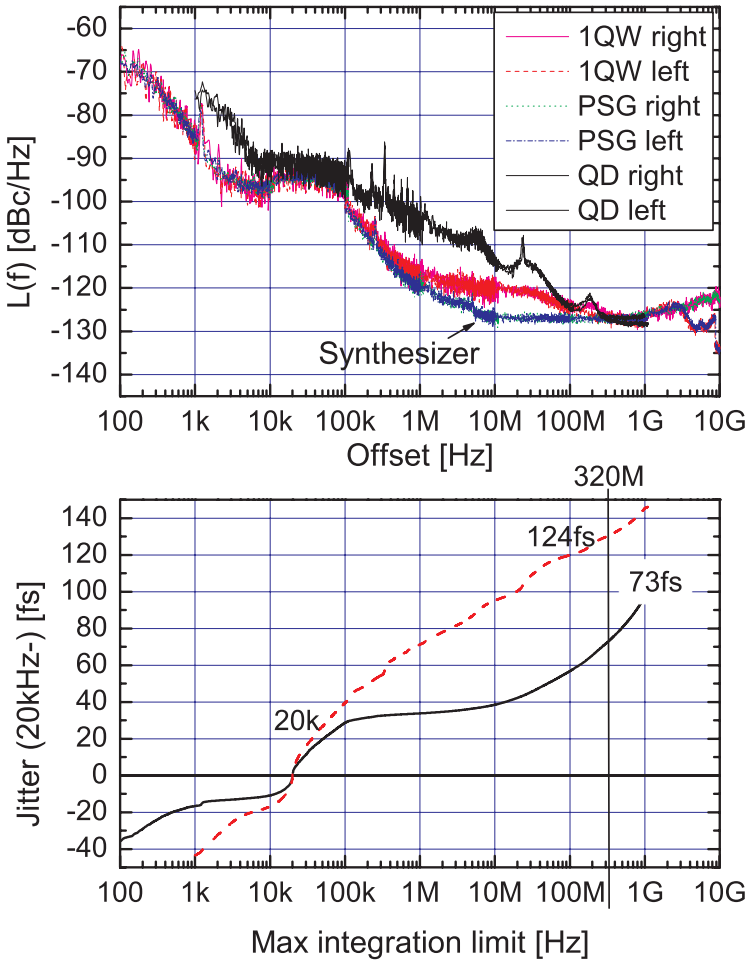

Figure 5.22: Absolute phase noise spectrum and integrated timing jitter for hybrid mode-locked 40-GHz QD-laser and 1-QW laser. The operating conditions are given in table 5.3.

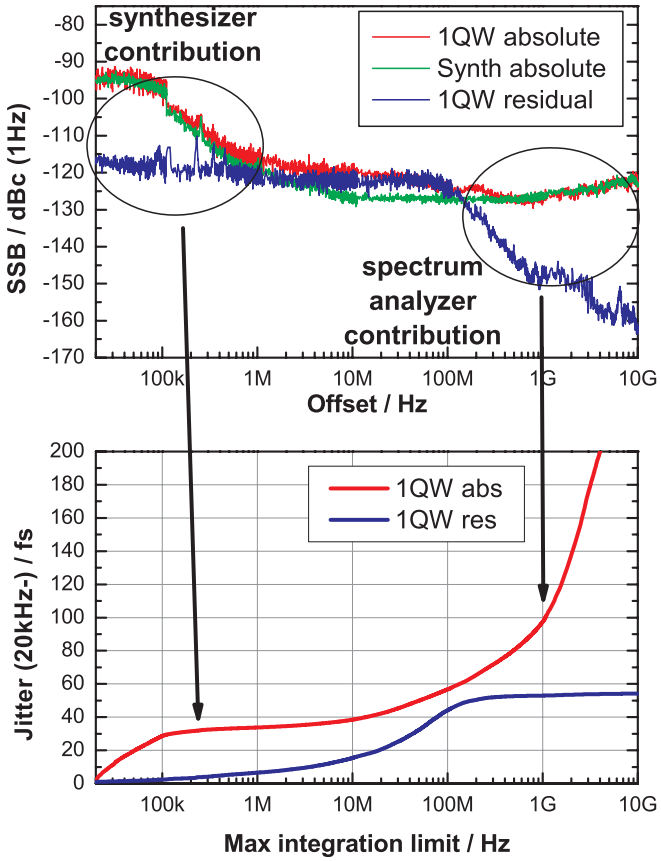

Figure 5.23: Comparison of direct and residual phase noise measurements with the same 1-QW laser diode (and approximately the same operating conditions). At low frequencies (<1MHz), the absolute laser spectrum is dominated by the noise of the synthesizer, which it tracks perfectly. At high offset frequencies (>100 MHz in the case of this laser), the spectrum analyzer sets the lower measurement limit, in this case -125 dBc(1Hz) at best. The absolute measurement was performed with an Agilent E6585 SA.

by the RF-oscillator can be tracked by the CR-circuit, as discussed in chapter 2, and thus the residual noise is actually a better measure of the total jitter after CR.

Such residual measurements, as described above, have been performed by several mode-locking groups in the past [97, 98, 42] at a repetition frequency of 10 GHz or lower. A more thorough treatment on how to make good residual phase-noise measurements is given in the journal paper of Scott et al. [43]. Scott et al. goes into details about the dynamic range requirements, the photoreceiver design for high bandwidth and low noise and finally the calibration of the measurement system. Appendix B in this thesis goes through some of the details of how to choose individual components of the system, how to calibrate the system and how to calculate and measure the noise-floor. At 40 GHz repetition rate the difficulty of making the measurement has scaled with the frequency (at least if you are interested in the high-frequency noise). The electronics on the input side (to the mixer) and the mixer should have a bandwidth of 40 GHz around the centre frequency 40 GHz to allow for integration to the half repetition rate. The output electronics should have a bandwidth of 20 GHz from DC. Furthermore all the electronics should have low noise and at the same time a high gain or low loss. We have chosen waveguide electronics to achieve a large bandwidth around the 40 GHz repetition rate. The so-called Q-band extends from 33 to 50 GHz (17 GHz bandwidth), and this is the band we use.

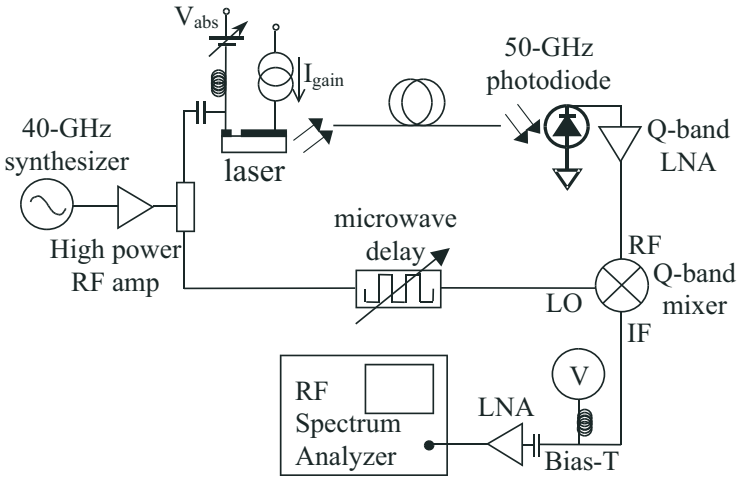

Figure 5.24: Residual phase noise measurement set-up. The laser noise signal travels in the upper part to the RF port, while the synthesizer reference signal travels in the lower part to the LO port. V_{abs}, absorber DC voltage; I_{gain}, gain current; RF, radio frequency (signal); LO, local oscillator; IF, intermediate frequency; V, voltage meter. Only the mixer, first LNA (Q-band) and the microwave delay are waveguide components (<10 cm in each arm).

The set-up The heart of the set-up, fig 5.24, is the double balanced waveguide mixer. Before reaching the mixer the laser signal is detected by an ac-coupled

and 50ohm-terminated high speed photodetector with an almost flat response (0.08 dB/GHz and BW_{3dB} >50 GHz) in the frequency range of the electronic waveguides. After conversion to electrical signal, the signal is in principle a sinusoid. Before entering the RF-port of the mixer the signal is amplified 24 dB. The reference LO-signal to the mixer can be shifted in phase by a tuneable phase shifter, making it possible to put the two signals in quadrature (out of phase). The output of the mixer (DC-17 GHz) is filtered in a broadband bias-T, and the dc-level is monitored on a voltage meter in order to adjust the phase shifter to obtain quadrature. The high frequency part (20 kHz-15 GHz) passes on to a broadband preamplifier (f_{3dB} : 30 kHz/12 GHz) before it reaches the Spectrum Analyzer.

The mixer produces an output proportional to the product of the two inputs. The fundamental line of the laser photo current and its noise band shifts in frequency with the frequency of the LO, $\pm\omega_{LO}$ (up and down conversion). If the LO-frequency is the same as the fundamental then the spectrum shifts to baseband, which makes it easy to filter high frequency components as well as the DC-component. The RF-port is driven by our noisy signal, $v_{RF}(t) = V_{RF}\cos(\omega_0 t + \phi(t))$, where ω_0 is the fundamental repetition frequency of the laser and $\phi(t) = (\omega(t) - \omega_0)t$ contains all the phase (dependent on repetition frequency or equivalently timing) uncertainty. The local oscillator port is driven by a pure sinusoid with an adjustable phase, $v_{LO}(t) = V_{LO}\cos(\omega_0 t + \theta)$. When $\theta = \pi/2$, i.e. the two signals are out of phase, the output is (after low-pass filtering)

$$v_{if}(t) = v_{RF}(t) \cdot v_{LO}(t) = \frac{\alpha}{2} V_{LO} V_{RF} \sin\phi(t) \approx \frac{\alpha}{2} V_{LO} V_{RF} \phi(t) \qquad (5.5)$$

where α is the gain or loss in the mixer, the so-called mixer conversion constant. We see that for small phase deviations the output voltage is linearly proportional against the phase deviation. If we measure the RMS voltage spectral density of v_{if} with an ESA, and can calculate the proportionality constant, in this case $\frac{\alpha}{2} V_{LO} V_{RF}$ (how to calculate the transfer function of the entire system will be shown in appendix B), then we can convert the measured spectrum into S_ϕ. The computed S_ϕ is the double sideband phase-noise spectrum (since both lower sideband and upper sideband components are converted to the same frequency) and to get the SSB we divide by two, $\mathcal{L}(f) = S_\phi(f)/2$ [43].

Noise floor It is interesting to make a calculation of the noise floor of the system, since it limits the minimum detectable signal. The calculation can be found in Appendix B. The noise figure of the total system is dominated by the first amplifier, which has a NF of 5 dB and a gain of 24 dB, giving a theoretical thermal noise floor of -169 dBm/Hz. The phase-noise contribution from shot-noise in the photodiode is -168 dBm/Hz at an optical average input power of 4.5 dBm (2 mA DC-current), which is the maximum level that doesn't saturate the mixer. The noise floor is however also influenced by the rejection of the synthesizer noise. The noise originating from the synthesizer is correlated and cancel if the two arms are equal, but the rejection worsens with the offset frequency and is zero at $f = 1/4\Delta t$, where Δt is the difference in path length of the laser and reference paths [27]. In order to reduce the synthesizer contribution it is a good idea to use 1) as equal path lengths as possible (in principle as short fibre length as possible) and 2) a low-noise synthesizer. Our shortest possible fibre length is 2 m and we make use of an Agilent E8247C synthesizer with ultra-low phase-noise option. The noise floor

including the synthesizer contribution can be measured by replacing the laser by an equivalent attenuator (38 dB in this case), and is included in figure 5.28. This is our experimental noise floor. Integrating the noise floor results in a timing jitter floor of 5 fs.

Calibration The calibration of the system is done with the so-called Beat-Note Method [43]. A second 50-GHz tuneable synthesizer (HP 83650A) is swept in frequency between 33 and 50 GHz, simulating the frequency components of the noise. Since we know the input signal and measure the output, we can calculate a transfer curve. This transfer curve is valid over a large range of input powers. Before putting the parts together to a complete system we have measured transfer curves of the photodiode, the first LNA and the mixer in order to define a linear power operating regime. By monitoring the DC-current of the photodiode we can be sure not to saturate any part of the system. After passing the mixer, saturation is of less importance since the DC-signal is filtered away in the bias-T and only the (laser) noise passes on to the next LNA. More details on calibration can be found in Appendix B.2.

Measurements on 40-GHz QW lasers with different number of wells The measured lasers are Fabry-Perot type monolithic mode-locked lasers with 1, 2 or 3 QWs, with the epitaxial structure SCOOP6 described in chapter 3. All lasers have an HR-coated absorber facet (section 4.4.2). The temperature is 20 °C except for the 3-QW laser which is kept at 18 °C to keep the laser inside the EDFA-window. The other operating conditions are chosen for lowest noise after the following scheme: 1) Passive mode-locking maps are made, 2) from these a smaller range of gain and absorber biases are explored now with the RF modulation also applied to the absorber. 3) When a good pair of gain and absorber biases is found during hybrid mode-locking, everything is fixed except the RF-frequency. 4) While the frequency is varied the RIN is logged and gives us instantaneous feed-back on the level of the noise. Figure 5.25 shows the dependence of RIN on RF-frequency (2-QW laser) with all other operating conditions fixed. Figure 5.26 shows the dependence of the integrated timing jitter for the same laser.

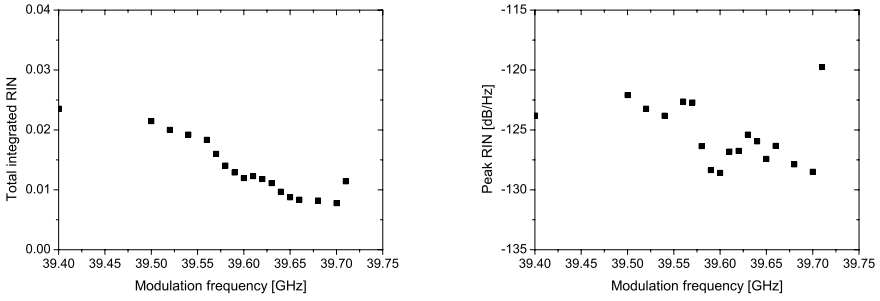

(a) Total RIN

(b) Peak RIN

Figure 5.25: Total RIN and peak RIN as function of the synthesizer frequency. I_{gain} and V_{abs} was kept constant.

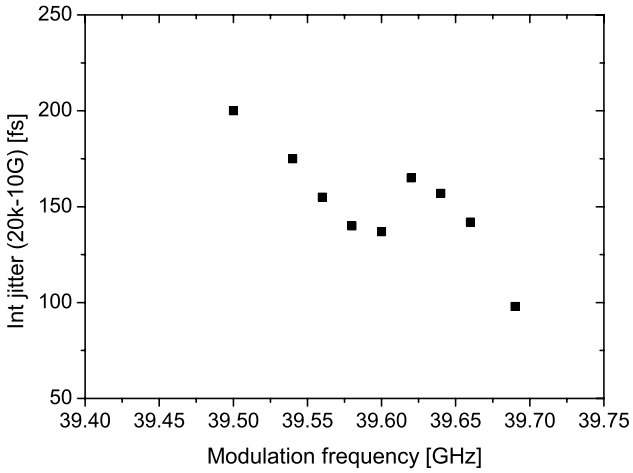

Figure 5.26: Integrated residual RMS jitter as function of the synthesizer frequency. I_{gain} and V_{abs} was kept constant.

Figure 5.27 displays the optimised single side-band (SSB) phase-noise for the three FP-lasers. These spectra have several features that are worth analysing in more detail. If we compare them to the theoretical results of Jiang (see section 2.2), i.e. equation 5.6, we conclude that the most important features are the white noise plateau and the following roll-off.

$$L_{fgs}(f) = \left(\frac{2\pi}{T_M}\right)^2 \frac{2\tau^2}{A_0^2} \frac{1}{(2\pi f) + (2\gamma_0^{\Re})^2} \left[\frac{P_{ASE}}{4\pi} + 0.16\omega_{relosc}^2 \tau^2 T_R^2 \frac{1}{A_0^2} S_A(\omega)\right] \tag{5.6}$$

According to [27] the first feature is associated with the strength of the spontaneous emission level, P_{ASE}, relative to the pulse steady-state power, A_0^2. How to minimise noise and optimise pulse power was described in chapter 2 and 3. In short the spontaneous emission level is set by the loss in the laser cavity and the population inversion factor, while the pulse power is determined by the pulse saturation energy (power), E_{sat}, defined in chapter 3. A low loss and high power laser will have a low white noise level! The Lorentzian roll-off originates from the low-pass filtering of the cavity, with a corner frequency, $\gamma_0^{\Re} = M_{AM}\omega_M^2\tau^2/4T_R$, given by the strength of the modulation, M_{AM}, the pulse width, τ, the modulation frequency, ω_M, and the round-trip time of the cavity, T_R. Yilmaz et al. found experimentally that there was an inverse relationship between the roundtrip time and the corner frequency [42]. They also found that the corner frequency and the longitudinal mode linewidth of the laser matched closely when changing the cavity frequency in their external cavity laser [99].

The roll-off is characterised by a 25 dB/dec slope and peaks (especially in the case of 2 and 3 QWs) of a few hundred MHz width in the range between 500 MHz and 2 GHz. From equation 5.6 we see that the roll-off should be 20 dB. A higher slope can be a sign of slight detuning, according to the theory of Hjelme

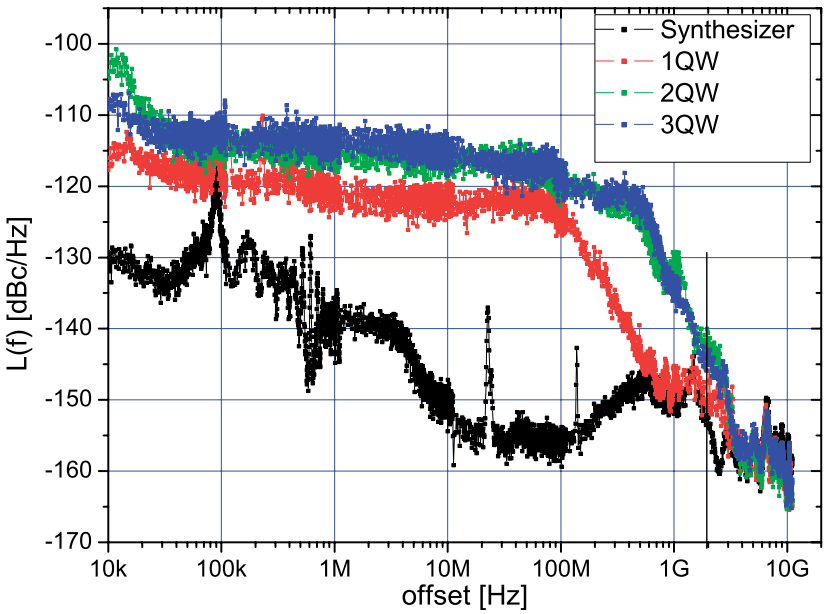

Figure 5.27: Residual single sideband traces (obtained from Double sideband traces by subtracting 3 dB) of lasers with 1, 2 and 3 QWs. The experimental noise floor is also added.

and Mickelsen [36] (see section 2.2 also). Similar peaks at the same frequencies are found in the RIN-spectra, figure 5.27. This indicates a coupling between amplitude noise and phase-noise due to a finite alpha factor and finite recovery times of the gain medium. The amplitude noise power spectrum, S_{A} in equation 5.6, is also a Lorentzian with a pole at the relaxation oscillation frequency [27, appendix B]. For diode lasers the amplitude noise contribution to the timing noise can be significant around the natural frequency of the laser. After the relaxation oscillation frequency the amplitude contribution rolls off as f^4 and should be of less importance. The low frequency slope (<30 kHz) is thought to be due to noise from the current source. At frequencies higher than 3 GHz all lasers have met the noise floor.

Figure 5.28 presents the RMS timing jitter obtained from integrating the phase noise spectrum from 20 GHz to a lower variable integration limit. This is equivalent to integrating down to a the bandwidth of a clock-recovery circuit. The figure presents an upper limit of the jitter since the integration is performed with the noise floor value for frequencies between 20 GHz and 10 GHz. If we assume that the roll-off continues as predicted by theory [36, 27], then the total timing jitter (10 kHz-20 GHz) for the 1-QW laser is 44 fs. This can be done because the laser is mode-locked at the fundamental cavity frequency and no supermode noise is present.

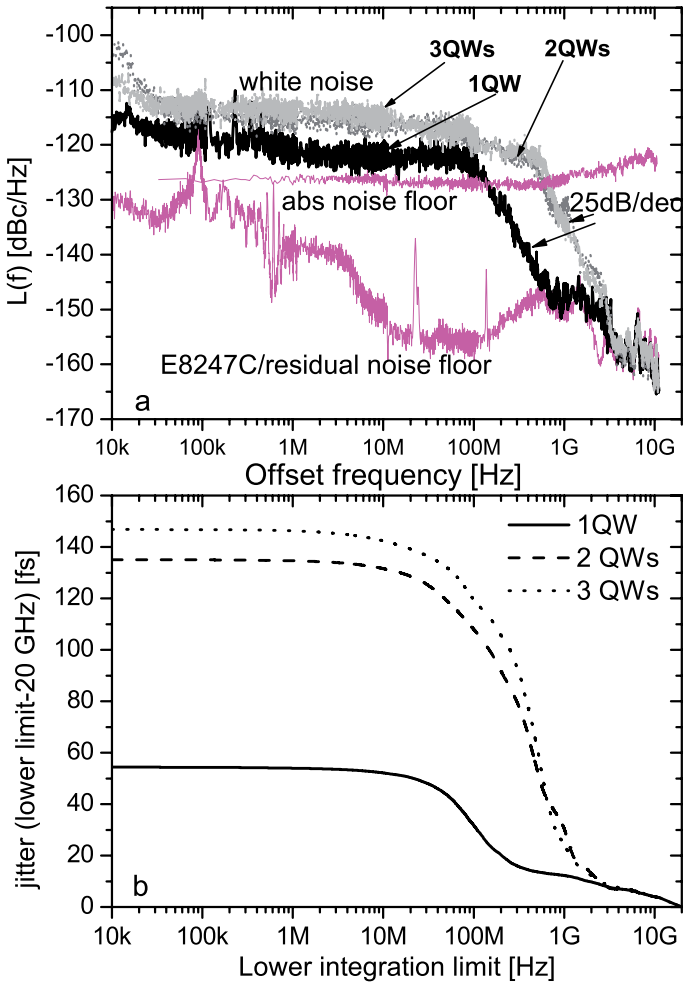

Figure 5.28: a) Same as former figure. b) Integrated timing jitter from 20 GHz to lower integration limit. Between 20 and 10 GHz an upper limit of the jitter is calculated from the 10 GHz noise floor.

The RIN-spectra for the three lasers are found in figure 5.29 for the same operating conditions as the residual phase-noise spectra. The peak values correspond to relaxation oscillations, which are most prominent in the lasers with multiple quantum wells. After the relaxation oscillation frequency the amplitude noise drops off and met the noise floor quickly (around -152 dB/Hz). The 1-QW laser is well below the level that is required for 1 dB power penalty (c.f equation 2.17 and table 2.1). The maximum RIN of the other lasers is very close to the maximum allowable value, but since we should integrate to 20 GHz the RMS value is much below the requirement.

Table 5.4: Operating conditions for figure 5.28. P_{RF}, modulation power (No 50 Ohm matching, ∼28% is absorbed). Both temporal and spectral widths are given by fits to a hyperbolic secant. The 1-QW spectrum exhibits an extended tail on the short-wavelength side of the peak, meaning that the FWHM spectral width isn't a good figure of merit in this case.

#QW	I_g (mA)	V_a (V)	P_{RF} (dBm)	f_{RF} (GHz)	λ (nm)	Δt (ps)	$\Delta\lambda$ (nm)	TBP	P_{fibre} (mW)
1	191	-2.7	26	39.78	1531	1.1	2.22	0.38	9.2
2	190	-3.8	26	39.58	1547	1.2	3.62	0.51	8.7
3	240	-4.0	26	39.53	1562	1.4	3.55	0.61	9.0

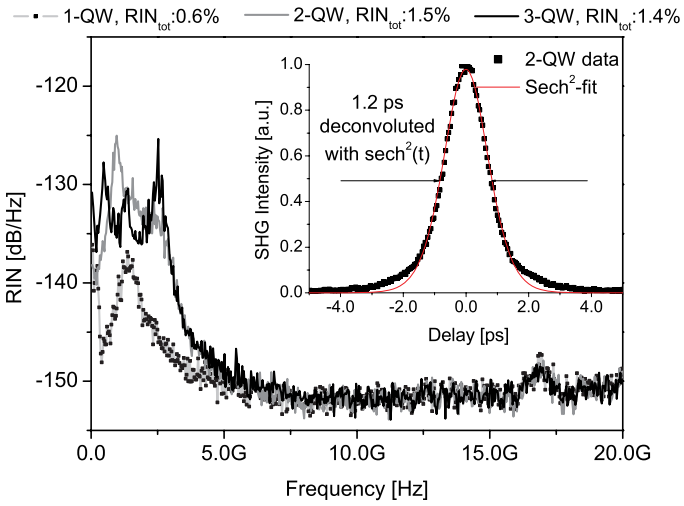

Figure 5.29: RIN of 40 GHz 1,2 and 3-QW lasers. All lasers exhibit relaxation oscillation peaks in the range from a few 100 MHz to a few GHz. The peak RIN is about 10 dB lower for the 1-QW laser. The total RMS amplitude noise (RIN_{tot}) is integrated from 0 Hz to 20 GHz and is in percent of the mean optical power hitting the photodiode. The inset shows the autocorrelation trace for a somewhat compressed pulse of the 2-QW laser with 0.63 ps/nm dispersion.

5.3 Results

In this chapter the performance of fabricated deeply etched surface gratings have been characterised. The gratings have a center wavelength very close to the designed one and a nearly Gaussian shape. The loss in the gratings alone have not been measured yet, but the total loss in lasers with gratings seems not to be larger than for equivalent FP-lasers, taken that they have approximately the same current threshold. The reflection of the gratings were evaluated with a method for measuring AR-coatings and found to be 1%, much below the calculated 17%. The bandwidth was also obtained with the same method and was about 2 nm. This indicate a much smaller effective index difference than the calculated 0.008, about 0.002 (the exact value depends on the loss in the grating). This is the major drawback of the fabricated gratings. However, as explained in chapter 4 the actual fabrication batch was far from perfect and more square gratings should give higher reflectivity (and slightly increased bandwidth). Longer gratings will also produce a higher reflection. Increasing the length with 50 μm should increase the reflection with 75 %, while the bandwidth decreases with 24 % only. Fourth order gratings is another option of achieving better grating shape.

The mode-locking performance of a number of high-speed monolithic mode-locked lasers have been investigated. These monolithic devices are well suited for applications in high-speed optical communication systems and high-speed photonic sampling, where timing jitter sets the hardest requirements. That's why a major part of this chapter was spent on measurements of timing jitter.

The measurements on 10-GHz FP-lasers have shown that long all-active lasers can have lower timing jitter than external cavity lasers, at the same time as they have short pulses and high output power. These measurements have corroborated design ideas about the gain material presented in [30]. The mode-locked performance of the first mode-locked laser with an integrated deeply etched surface Bragg grating has been presented and compares favourably to previously reported 10-GHz lasers with standard Bragg gratings. The performance was also compared to the performance of FP-lasers from the same wafer. The pulses were a little longer for the DBR, in which the bandwidth of the grating limits shortening of the pulse, but had a much better spectrum on the other hand. Output power was comparable, while the noise was a little worse for the DBR, which is explained by the low reflectivity of the DBR.

Lastly, the ultra-low-noise performance of 40-GHz lasers with different gain materials have been presented. A state-of-the-art measurement system has been made and was presented. The first residual phase-noise measurements on 40-GHz lasers have been presented. With the measurement it was possible to distinguish between small changes in the gain material and a record low jitter was found for a 1-QW laser. The first results of hybrid mode-locking a QD-laser at 40 GHz has also been presented. The results were compared to a laser with 1-QW gain material. It was found that the QD-laser had an exceptionally lower timing noise during passive mode-locking, and the plausible reasons for it were discussed.

Chapter 6

Conclusions and outlook

6.1 Conclusions

This thesis has presented the realisation of a monolithic mode-locked laser integrated with a deeply surface etched Bragg grating. The pulses from the new lasers are more well-behaved than the pulses from Fabry-Pérot lasers made from the same material and thus are more suitable for the intended applications: pulsed high-speed communication systems, microwave photonic communication and optical sampling. Design criteria for the grating were derived from the requirements on a filter for mode-locking. To realise the grating, cleanroom process development has been a central part of the work, especially the development of a cyclic reactive ion etch for the etch of InP with glass as a masking material. To reduce macro and especially micro loading effects in the etch was seen to be paramount in the realisation of deep gratings with a large index contrast. Macro loading effects can be reduced by working at low pressure and by guard rings preventing lateral flow of etch species. The micro loading effects were believed to be combination of geometrical shadowing of both ions and chemical etch species. A low pressure is also advantageous for reducing micro loading.

The performance of the 10-GHz DBR lasers was superior to the performance of the 10-GHz FP lasers from the same wafer when taking all requirements into consideration: short pulses and transform-limited spectra with a low background, a well-defined center wavelength that do not change with bias conditions, a high power and a low noise level. Transform-limited pulses from the hybrid mode-locked DBR laser were obtained after linear compression with a pulsewidth of 3.6 ps, an average fibre-coupled power of 5 mW and a jitter of 250 fs (20kHz-80MHz). The reflectivity of the gratings was too low to make good 40-GHz lasers. After AR-coating the threshold was 100 mA or more.

Measurements of timing noise on lasers designed to have very low quantum noise have been presented. In particular, a measurement system for quantum limited noise performance at very high repetition rates, 40 GHz, has been demonstrated. It has been used to successfully verify the design ideas for low-noise mode-locked lasers. Different noise sources can be distinguished from the measurements by a comparison to existing theory: amplified spontaneous emission, cavity detuning and amplitude noise coupled to timing noise at the relaxation resonance of the carrier-photon system. It was also able to distinguish the noise levels from three

different quantum well lasers with slightly different design. The lowest timing jitter of 44 fs integrated from 20 GHz to 10 kHz was achieved for a 1-QW all-active laser.

6.2 Outlook

There are several straightforward possibilities for making improved surface gratings for mode-locked lasers even without changing the current etch. If the same wafer material is to be used as during my PhD-project, then the most straightforward is to make fourth order gratings. This option was not tried yet because it was believed that a third order grating would give the desired result. If a new material structure is grown, then one should consider the following for better grating processing: 1) A lower ridge. This is especially true for 10 GHz lasers were the absorber does not need to have such a high bandwidth. 2) An thin Al-containing etch stop layer to enable overetch. 3) An emission wavelength slightly shorter than the Bragg peak.

Once the fabrication issues are solved it would of course be interesting to make wider filters than what was possible in this project. Chirped gratings are also interesting for compensation of chirp from the saturable absorber and gain sections as has already been presented in [52]. With a higher reflection, 40-GHz DBR laser can be made and one could use the high-dynamic range measurement set-up for comparing the quantum noise of DBR lasers and FP lasers.

The cyclic InP etch developed for the ridge and grating definition have great potential for making integrated photonics with ridge waveguides: Y-splitters, mirrors, bending waveguides and gratings in all crystal planes. An entirely lithographically defined monolithic mode-locked laser would be an interesting project. A short high-reflectivity mirror next to the absorber would make the pulse self-colliding without applying an HR-coating. The other grating will act as the bandpass filter and also as an output coupler to other integrated elements on the same chip, such as splitters and modulators and amplifiers. The lithographically defined length would make it ideal for applications where a fixed and exact repetition frequency is needed.

The extremely low noise of the passive mode-locked quantum dot lasers make it interesting to make high-dynamic range measurements on 40-GHz passive lasers. In principle the same set-up can be used but with the synthesizer exchanged for a voltage controlled oscillator. Gunn oscillators have high repetition frequencies, low noise and can be tuneable in sufficing ranges. The DC-signal from the output of the mixer is used as an error signal to the oscillator so that the oscillator follows the slow variations in the laser repetition rate and locks to it. A more thorough comparison of the noise in QD and QW is very interesting, and QDs made from material grown on InP could make the analysis a little easier.

Bibliography

[1] K. Gürs, "Beats and modulation in optical ruby lasers," in Quantum Electronics III, P. Grivet and N. Bloembergen, Eds. New York: Columbia Univ. Press, 1964, pp. 1113-1119.

[2] H. Haus, "Mode-Locking of lasers," IEEE, J. Sel. Top. Quant. Elec., Vol. 6, No. 6, November/December 2000.

[3] J. E. Bowers, P. A. Morton, A. Mar, S. W. Corzine, "Actively Mode-Locked Semiconductor Lasers," IEEE J. Quant. Elec., Vol. 25, No. 6, June 1989.

[4] H. Haus and H. Dyckman, "Timing of laser pulses produced by combined passive and active mode-locking," Int. J. Electronics, Vol. 44, No. 3, 1978.

[5] T. Nelson, IEEE J. Quant. Electron., Vol. 8, No. 29, 1972

[6] Y. K. Chen, M. C. Wu, T. Tanbun-Ek, R. A. Logan, and M. A. Chin, "Subpicosecond monolithic colliding-pulse mode-locked multiple quantum well lasers," Appl. Phys. Lett. 58 (12), 25 March 1991.

[7] G. Agrawal, "Fiber-Optic Communication Systems," Wiley Series in Microwave and Optical Engineering, Edited by K. Chang, ISSBN 0-471-17540-4, 1997.

[8] F. Zamkotsian, K.Sato, H. Okamoto, K. Kishi, I. Kotaka, M. Yamamoto, Y Kondo, H. Yasaka, Y. Yoshikuni, and K. Oe, "Monolithic integration of MQW modulators on an optical multiplexer on InP for 100 Gb/s transmission," Journal of Lightwave Technology, 14(10):2344-2352, October 1996.

[9] S. Kawanishi, H. Takara, K. Uchiyama, I. Shake, and K. Mori, "3 Tbit/s (160Gbit/s*19ch) OTDM/WDM transmission experiment, In OFC Technical digest, p. PD1-1, OSA, San Diego, USA, 1999.

[10] D. Breuer, and K. Petermann, "Comparison of NRZ- and RZ-modulation format for 40-Gb/s TDM standard-fiber systems," IEEE Phot. Tech. Lett., Vol. 9, No. 3, March 1997.

[11] A. Clausen, H. Poulsen, L. Oxenlowe, A. Siahlo, J. Seoane, P. Jeppesen, "Pulse source requirements for OTDM systems," in 2003 IEEE LEOS Annual Meeting Conference Proceedings.

[12] M. Jinno, "Effect of Crosstalk and Timing Jitter on All-Optical Time-Division Demultiplexing Using a Nonlinear Fiber Sagnac Interferometer Switch," IEEE J. Quant. Elec., Vol. 30, No. 12 Dec. 1994.

[13] L. Oxenlowe, COM-DTU, systems competence area, personal communication.

[14] L. Oxenlowe et al, "Pre-scaled clock recovery with compact semiconductor devices for ultra high-speed OTDM systems," ECOC 2004.

[15] T. Ono, T. Shimizu, Y. Yano, and H. Yokoyama, "Optical clock extraction from 10Gbit/s data by using monolithic mode-locked laser," OFC '95, Technical Digest, Postconference edition, p. 288-9, 1995.

[16] M. Shirane, Y. Hashimoto, H. Kurita, H. Yamada, and H. Yokoyama, "Optical sampling measurement with all-optical clock recovery using mode-locked diode lasers," OFC 2001.

[17] T. Ohno, K. Sato, T. Shimizu, T. Furuta, and H. Ito, "40-GHz optical clock recovery from a 160 Gbit/s optical data stream using a regeneratively mode-locked semiconductor laser," OFC 2002.

[18] I. Ogura, H. Kurita, T. Sasakiand, and H. Yokoyama, "Precise operation-frequency control of monolithic mode-locked laser diodes for high-speed optical communication and all-optical signal processing," Optical and Quantum Electronics 33, 709-725, 2001.

[19] S. Arahira, S. Sasaki, K. Tachibana, Y. Ogawa, "All-Optical 160 Gb/s Clock Extraction With a Mode-Locked Laser Diode Module," IEEE Phot. Tech. Lett., Vol. 16, No. 6, June 2004.

[20] T. Ohno, K. Sato, R. Iga, Y. Kondo, K.Yoshino, and H. Ito, "A 160-GHz Semiconductor Mode-Locked Laser Diode and Its Application to Optical Clock Recovery," 2005.

[21] I. Ogura, Y. Hashimoto, H. Kurita, T. Shimizu, and H. Yokoyama, "Picosecond All-Optical Gate Using a Saturable Absorber in Mode-Locked Laser Diodes," Phot. Tech. Lett., Vol. 10, No. 4, April 1998.

[22] H. Kurita, Y. Hashimoto, I. Ogura, H. Yamada and H. Yokoyama, All-Optical 3R Regeneration based on Optical Clock Recovery with Mode-Locked LDs," In ECOC proceedings, 1999.

[23] E. A. Avrutin, J. H. Marsh and E. L. Portnoi, "Monolithic and multi-GigaHertz mode-locked semiconductor lasers: Constructions, experiments, models and applications," IEE Proc.-Optoelectron., Vol. 147, No. 4, August 2000.

[24] T. Ohno, K. Sato, S. Fukushima, Y. Doi, and Y. Matsuoka, "Application of DBR Mode-Locked Lasers in Millimeter-Wave Fiber-Radio Systems," J. Ligtwave Techn., Vol. 18, No. 1, January 2000.

[25] P. W. Juodawlkis, J. C. Twitchell, G. E. Betts, J. J. Hargreaves, R. D. Younger, J. L. Wasserman, F. J. O'Donnell, K. G. Ray, and R. C. Williamson, "Optically Sampled Analog-to-Digital Converters," IEEE Trans. Microwave Theory and Techniques, Vol. 49, No. 10, October 2001.

[26] K. Ioakeimidi, R. F. Leheny, S. Gradinaru, P. R. Bolton, R. Aldana, K. Ma, J. E. Clendenin, J. S. Harris, R. F. W. Pease, "Photoelectronic Analog-to-Digital Conversion: Sampling and Quantizing at 100 Gs/s," IEEE Trans. Microwave and Techniques, Vol. 53, No. 1, January 2005.

[27] L. Jiang, "Ultralow-Noise Modelocked Lasers," PhD-thesis, MIT, May 2002.

[28] Paul W. Juodawlkis, Jonathan C. Twichell, Jeffrey L. Wasserman, Gary E. Betts, and Richard C. Williamson, "Measurement of mode-locked laser timing jitter by use of phase-encoded optical sampling," Optics Letters, Vol. 26, No. 5, March 1, 2001.

[29] T. Brabec, S. Kelly and F. Krausz, "Compact sources of Ultrashort Pulses" edited by Irl N Duling, Cambridge University Press 1995. ISBN 0 521 46192 8.

[30] K. Yvind, "Semiconductor Mode-Locked Lasers for Optical Communication Systems," PhD-thesis, Technical University of Denmark, 2003, ISBN 87-90974-46-8.

[31] D. J. Kane and R. Trebino, "Characterization of Arbitrary Femtosecond Pulses Using Frequency-Resolved Optical Gating," IEEE J. Quant. Elec., Vol. 29, No. 2, February 1993.

[32] K. W. DeLong, R. Trebino, J. Hunter & W. E. White, "Frequency-resolved optical gating with the use of second-harmonic generation," JOSA B Vol. 11 (11) 1994.

[33] R. Trebino, "FROG. The Measurement of Ultrashort laser pulses," Kluwer Academic Publishers, ISBN 1-4020-7066-7, 2000.

[34] P. Delfyett, "Compact sources of Ultrashort Pulses" edited by Irl N Duling, Cambridge University Press 1995. ISBN 0 521 46192 8.

[35] L. A. Jiang, M. E. Grein, H. A. Haus, and E. P. Ippen, "Noise of mode-locked semiconductor laser," IEEE Journal on Selected Topics in Quantum Electronics, 7(2):159167, March/April 2001.

[36] D.G. Hjelme and A. R. Mickelson, Theory of Timing Jitter in Actively Mode-Locked Lasers, IEEE Journal of Quantum Electronics 28, no. 6, 1594 (1992).

[37] L. A. Jiang, E. P. Ippen, and H. Yokoyama, "Semiconductor mode-locked lasers as pulse sources for high bit rate data transmission," J. Opt. Fiber Commun. Rep. 2, 1-31 (2005).

[38] G.8251 "The control of jitter and wander within the optical transport network (otn)," Recommendation G.8251, ITU-T, November 2001.

[39] K. Yvind, D. Larsson, L. Christiansen, C. Angelo, L. Oxenlowe, J. Mork, D. Birkedal, J. Hvam and J. Hanberg, "Low-jitter and High-Power 40-GHz All-Active Mode-Locked Lasers," IEEE Phot. Techn. Lett. , Vol. 16, No. 11, Nov 2004.

[40] D. Von der Linde, "Characterisation of the noise in continuously operating mode-locked lasers," Applied Physics B 39, pp 201, 1986.

[41] H. Haus and A. Mecozzi, "Noise of Mode-Locked Lasers," IEEE J. Quant. Elec., Vol. 29, No. 3, March 1993.

[42] T. Yilmaz, C. M. DePriest, and P. J. Delfyett, Jr., "Complete noise characterisation of external cavity semiconductor laser hybridly modelocked at 10 GHz," Electron. Lett., Vol. 37, No. 22, pp. 1338-1339, 2001.

[43] R.P. Scott, C. Langrock, and B. H. Kolner, "High-Dynamic-Range Laser Amplitude and Phase Noise Measurement Techniques," IEEE Journal on Selected Topics in Quantum Electronics, Vol. 7, No. 4, July/August 2001.

[44] D. Zibar, J. Mork, L. K. Oxenlowe, M. Galili and A. T. Clausen, "Timing Jitter Analysis for Clock-Recovery Circuits based on an Optoelectronic Phase-Locked Loop (OPLL)," Conference on Lasers and Electro Optics 2005, pp. 458-460.

[45] J. Zhang, M. Yao, X. Chen, L. Xu, M. Chen, Y. Gao, "Bit Error Rate Analysis of OTDM System Based on Moment Generation Function," IEEE J. Ligthwave Techn. , Vol. 18, No. 11, November 2000.

[46] G. Agrawal, and A. Olsson, "Self-phase modulation and spectral broadening of optical pulses in semiconductor laser amplifiers," IEEE J. Quant. Elec., Vol. 25, No. 11, p. 2297-2306, 1989.

[47] D. J. Derickson, P. A. Morton, J. E. Bowers, and R. L. Thornton, "Comparison of timing jitter in external and monolithic cavity mode-locked semiconductor lasers," Appl. Phys. Lett., Vol. 59, No. 26, December 1991.

[48] F. Camacho, E. Avrutin, P. Cusumano, A. Helmy, A. Bryce, and J. Marsh, "Improvements in Mode-Locked Semiconductor Diode Lasers Using Monolithically Integrated Passive Waveguides Made by Quantum-Well Intermixing," IEEE Phot. Techn. Lett., Vol. 9, No. 9, September 1997.

[49] K. Yvind, D. Larsson, L. J. Christiansen, J. Mork, J. M. Hvam and J. Hanberg, "High-performance 10 GHz all-active monolithic modelocked semiconductor lasers," Vol. 40, No. 12, 10th June 2004.

[50] D. Larsson, K. Yvind, J. M. Hvam, "Wide-Band Residual Phase-Noise Measurements on 40-GHz Monolithic Mode-Locked Lasers," IEEE PTL Vol. 17, No. 11, Nov 2005.

[51] B. Huettl, R. Kaiser, M. Kroh, C. Schubert, and G. Jacumeit, and H. Heidrich, "Optical 40 GHz pulse source module based on a monolithically integrated mode locked DBR laser," Optoelectronic Materials and Devices for Optical Communications, Proceedings of SPIE, Vol. 6020, 2005.

[52] K. Sato, H. Ishii, I. Kotaka, Y. Kondo, M. Yamamoto, "Frequency Range Extension of Actively Mode-Locked Lasers Integrated with Electroabsorption Modulators Using Chirped Gratings," IEEE J. Sel. Top. Quant. Elec., Vol. 3, No. 2, April 1997.

[53] M. M. Raj, J. Wiedmann, S. Toyoshima, Y. Saka, K. Ebihara and S. Arai, "High-Reflectivity semiconductor/Benzocyclobutene Bragg Reflector Mirrors for GaInAsP/InP Lasers," Jpn. J. Appl. Phys. Vol. 40, pp. 2269-2277, (2001).

[54] J. Wiedmann, M. M. Raj, K. Ebihara, K. Matsui, S. Tamura and S. Arai, "Deeply etched semiconductor/Benzocyclobutene Distributed Bragg Reflector Laser Combined with Multiple Cavities for 1.5-my-wavelength Single-Mode Operation," Jpn. J. Appl. Phys. Vol. 40, pp. 4031-4037, (2001).

[55] H.-F. Liu, S. Arahira, T. Kunii, and Y. Ogawa, "Tuning Characteristics of Monolithic Passively Mode-Locked Distributed Bragg Reflector Semiconductor Lasers," IEEE J. Quant. Elec., Vol. 32, No. 11, November 1996.

[56] Y. Katoh, S. Arahira, and Y. Ogawa, "40 GHz Actively Mode-Locked DBR Laser Diodes with a Wide (800 MHz) Locking Range," OFC 2001, WC5-1.

[57] K. Sato, A. Hirano, and H, Ishii, "Chirp-Compensated 40-GHz Mode-Locked Lasers Integrated with Electroabsorption Modulators and Chirped Gratings," IEEE J. Sel. Top. Quant. Elec., Vol. 5, No. 3, May/June 1999.

[58] E. Zielinski, E. Lach, J. Bouayad-Amine, H, Haisch, E. Kühn, M. Shilling, and J. Weber, "Monolithic Multisegment Mode-Locked DBR Laser for Wavelength Tunable Picosecond Pulse Generation," IEEE J. Sel. Top. Quant. Elec., Vol. 3, No. 2, April 1997.

[59] G. Rayborn, P. B. Hansen, R. C. Alferness, L. L. Buhl, U. Koren, B. I. Miller, M. G. Young, T. L. Koch, J.-M. Verdeill, and C. A. Burrus, "Wavelength-tunable mode-locked actively mode-locked monolithic laser with an integrated vertical coupler filter," Optics Letters, Vol. 18, No. 16, August 15 1993.

[60] L. A. Johansson, Z. Hu, D. J. Blumenthal, L. A. Coldren, Y. A. Akulova, G. A. Fish, "40-GHz Dual-Mode-Locked Widely Tunable Sample Grating DBR Laser," IEEE PTL Vol. 17, No. 2, February 2005.

[61] Y.-H. Jan, M. E. Heimbuch, L. A. Coldren and S. P. DenBaars, "InP/InGaAsP grating assisted codirectional coupler tunable receiver with a 30 nm wavelength tuning range," El. Letters Vol. 32, No. 18, 29 August 1996.

[62] R. C. Alferness, U. Koren, L. L. Buhl, B. I. Miller, M. G. Young, T. L. Koch, G. Rayborn, and C. A. Burrus, Broadly tunable InGaAsP/InP laser based on a vertical coupler filter with 57-nm tuning range, Appl. Phys. Lett. 60 (26), 29 June 1992.

[63] P.-J. Rigole, S. Nilsson, I. Backbom, T. Klinga, J. Wallin, B. Stalnacke, E. Berglind, and B. Stoltz, 114-nm wavelength tuning range of a vertical grating assisted co-directional coupler laser with a super structure grating distributed Bragg reflector, IEEE Photon. Technol. Lett., vol. 7, pp. 697-699, July 1995.

[64] E. P. Ippen, D. J. Eilenberger and R. W. Dixon, "Picosecond pulse generation by passive mode locking of diode lasers," Appl. Phys. Lett. Vol. 37, No. 3, August 1980.

[65] P. Hansen, G. Raybon, U. Koren, B. Miller, M. Young, M. Chien, C. Burrus, and R. Alferness, "5.5-mm Long InGaAsP Monolithic Extended-Cavity Laser with an Integrated Bragg-Reflector for Active Mode-Locking," IEEE Phot. Techn. Lett. Vol. 4, No. 3, March 1992.

[66] K. Sato, I. Kotaka, Y. Kondo, M. Yamamoto, "Actively Mode-Locked Strained-InGaAsP Multiquantum-Well Laser Integrated with Electroabsorption Modulators and Distributed Bragg Reflectors," IEEE J. Sel. Top. Quant. Elec., Vol. 2, No. 3, September 1996.

[67] F. Delorme, S. Slempkes, G. Alibert, B. Rose, and J. Brandon, "Butt-jointed DBR laser with 15 nm tunability grown in three MOVPE steps," Elec. Letters, Vol. 31, No. 15, 20 July 1995.

[68] Y.-H. Jan, G. A. Fish, L. A. Coldren, and S. P. DenBaar, "Demonstration of InPInGaAsP Vertical Grating-Assisted Codirectional Coupler Filters and Receivers with Tapered Coupling Coefficient Distribution," IEEE PTL VOL. 9, NO. 7, JULY 1997.

[69] C. Coldren and Corzine, "Diode Lasers and Photonic Integrated Circuits," Wiley, 1995. ISBN 0-471-11875-3.

[70] B. Broberg and S. Nilsson, "Widely tunable active Bragg reflector integrated lasers in InGaAsP-InP," APL 52(16), 18 April 1988.

[71] D. Delprat, A. Ramdane, A. Ougazzaden and M. Carri, "Very simple approach for high performance tunable laser realisation," Electronic Letters Vol. 32, No. 2, 24th October 1996.

[72] R. Kaiser, B. Hüttl, H. heidrich, S. Fidorra, W. Rehbein, H. Stolpe, R. Stenzel, W. Ebert, and G. Sahin, "Tunable Monolithic Mode-Locked Lasers on InP with Low Timing Jitter," IEEE Photonics Technology Letters, Vol. 15, No. 5, May 2003.

[73] T. Ohno, K. Sato, R. Iga, Y. Kondo, K. Yoshino, and H. Ito, "160-GHz Actively Mode-Locked Semiconductor Laser and Its Application to Optical Clock Recovery," Laser Soc. Japan Review of Laser Engineering, Vol. 33, Issue 2, 2005.

[74] E. J. Skogen, J. S. Barton, Steven P. Denbaars, and Larry A. Coldren, "A Quantum-Well-Intermixing Process for Wavelength-Agile Photonic Integrated Circuits," IEEE J. Sel. Top. Quant. Elec., Vol. 8, No. 4, JULY/AUGUST 2002.

[75] A. McKee, C. J. McLean, G. Lullo, A. C. Bryce, R. M. De La Rue, J. H. Marsh, and C. C. Button, "Monolithic Integration in InGaAs-InGaAsP Multiple-Quantum-Well Structures Using Laser Intermixing," IEEE J. Quant. Elec., Vol. 33, No.1, January 1997.

[76] R. M. Lammert, A. M. Jones, C. T. Yousey, J. S. Hughes, S. D. Roh, I. Adesida, and J. J. Coleman, "InGaAsP-InP Ridge-Waveguide DBR Lasers with First-Order Surface Gratings Fabricated Using CAIBE," IEEE Photonics Technology Letters, Vol. 9, No. 11, Nobember 1997.

[77] M. Ke, B. D. Allan, X. F. Liu, A. Boyd, B. C. Qiu, Y. H. Qian, C. J. Hamilton, S. D. McDougall, O.P. Kowalski, A. C. Bryce, R. M. De La Rue, J. H. Marsh, "Monolithically integrated distributed Bragg reflector lasers for 1.5 μm operation with band gap shifted grating section," Optical Materials 14 (2000) 193-196.

[78] J. D. Plummer, M. D. Deal and P. B. Griffin, "Silicon VLSI Technology," Prentice Hall 2000, ISBN 0-13-085037-3.

[79] U. Niggebrügge, M. Klug, G. Garus, "A novel process for reactive ion etching on InP, using CH4/H2," Int. Symp. GaAs and Related Compounds, Karuizawa, Japan, 1985.

[80] E. Gini, "Plasma Etched Optical Corner Mirrors and Grating Demultiplexers in InGaAsP/InP," PhD-thesis ETH No. 12093, 1997.

[81] S. C. McNevin, "Chemical etching of GaAs and InP by chlorine: the thermodynamically predicted dependence on Cl_2 pressure and temperature," J. Vac. Sci. Technol. B, Vol. 4, No. 5, 1216-1226, 1986.

[82] R. Grover, J. V. Hryniewicz, O. S. King, and V. Va, "Process development of methanehydrogenargon-based deep dry etching of InP for high aspect-ratio structures with vertical facet-quality sidewalls," J. Vac. Sci. Technol. B 19(5), Sep/Oct 2001.

[83] T.R. Hayes, M. A. Dreisbach, P. M. Thomas, W. C. dautremont-Smith, and L. A. Heimbrook, "Reactive ion etching of InP using CH4/H2 mixtures: Mechanisms of etching and anisotropy," J. Vac. Sci. Technol. B Vol. 7, No. 5, Sep/Oct 1989.

[84] Y. Feurprier, Ch. Cardinaud, and G. Turban, "Influence of the gas mixture on the reactive ion etching of InP in CH4-H2 plasmas", J. Vac. Sci. Technol. B 15(5), Sept/Oct 1997.

[85] Y. Feurprier, Ch. Cardinaud, B. Grolleau, and G. Turban, "Proposal for an etching mechanism of InP in CH4-H2 mixtures based on plasma diagnostics and surface analysis," J. Vac. Sci. Technol. A 16(3), May/June 1998. French CNRS, etch rate vs. etch conditions & chemical reactions & model.

[86] J. H. den Besten, "Integration of Multiwavelength Lasers with Fast Electro-Optical Modulators," PhD-thesis,Technical University of Eindhoven, 2004.

[87] B.-T. Lee, T. R. Hayes, P. M. Thomas, R. Pawelek, and P. F. Sciortino, Jr, "SiO_2 mask erosion and sidewall composition during CH4/H2 reactive ion etching of InGaAsP/lnP," Appl. Phys. Lett. Vol. 63, No. 6, December 1993.

[88] H. Jansen, M. de Boer, R. Wiegerink, N. Tas, E. Smulders, C. Neagu, and M. Elwenspoek, "RIE LAG IN HIGH ASPECT RATIO TRENCH ETCHING OF SILICON," Elsiever Microelectronic Engineering 35, pp. 45-50, 1997.

[89] J. Liu, G. Huppert, and H. Sawin, "Ion bombardment in rf plasmas," J. Appl. Phys. Vol. 68, No. 8, October 1990.

[90] K. Janiak and U. Niggebrügge, "Investigation of macroscopic uniformity during CH4/H2 reactive ion etching of InP and improvement using a guard ring," IPRM 1996, pages 111-114.

[91] U. Niggebrügge, "Recent Advances in Dry Etching Processes for InP-Based Materials," IPRM 1991.

[92] Y. S. Oie, "Novel RIE-Process for High Quality InP-based waveguide stuctures," ECIO 1995 Proceedings.

[93] R. Ludwig "Experimentelle Untersuchungen an Halbleiterlaserverstärkern für die optische Nachrichtentechnik," PhD-thesis, Technischen Universität Berlin, 1993.

[94] L. Jiang, S. Wong, M. Grein, E. Ippen and H. Haus, "Measuring Timing Jitter With Optical Cross Correlations," IEEE Journal of Quant. Elec. Vol. 38. No. 8, August 2002.

[95] B. Peterson, Spectrum Analysis. Application note AN150, Agilent technologies 1989.

[96] Kresten Yvind, David Larsson, Lotte J. Christiansen, Leif K. Oxenløwe, Jesper Mørk, Jørn M. Hvam, and Jesper Hanberg, "Design and evaluation of mode-locked semiconductor lasers for low noise and high stability," Proceedings of SPIE (ISBN: 08 19-45810-4) pages: 37-48, 2005, SPIE.

[97] L. A. Jiang, M. Grein, E. Ippen, C. McNeilage, S. Jesse, and H. Yokoyama, "Quantum-limited noise performance of a mode-locked laser diode," Optics Letters Vol. 27, No. 1, pp. 49-51, 2002.

[98] D. J. Derickson, A. Mar, J. E. Bowers, "Residual and absolute timing jitter in actively mode-locked semiconductor lasers," Electronic Letters Vol. 26, No. 24, 1990.

[99] T. Yilmaz, C. M. DePriest, P. J. Delfyett, Jr., A. Braun and J. Abeles, "Measurement of residual phase noise and longitudinal-mode linewidth in a hybridly mode-locked external cavity semiconductor laser," Opt. Lett., Vol. 27, No. 10, May 2002.

[100] M.-C. Amann and J. Buus, "Tunable Diode Lasers," Artech house, Norwood, MA, 1998, ISBN 0-89006-963-8.

[101] Z.-M. Chuang and L. A. Coldren, "Design of Widely Tunable Semiconductor Lasers Using Grating-Assisted Codirectional-Coupler Filters," IEEE J. Quant. Elec., Vol. 29, No. 4, April 1993.

[102] Johnson, J. B., "Thermal agitation of electricity in conductors," Phys. Rev. 32:97, 1928.

[103] Nyquist, H., "Thermal agitation of electric charge in conductors, "Phys. Rev. 32:110, 1928.

[104] Yariv, A., "Optical electronics in modern communications," Oxford University Press, 1997, ISBN 0-19-510626-1 (cl).

[105] ZEONREX Technical Report ZEP520 Ver.1.02 Mar.2001, http://www.zeon.co.jp.

Appendix A

Filter design calculations

A.1 Grating-assisted codirectional couplers

The coupler calculations in this appendix aim at corroborating the hand waving about the pros and cons given in chapter 4. Most of the formulas can be found in the two textbooks [100, 69]. Complementary reading about the design of integrated coupler filters can be found in [101]. A coupler is obtained when the mode fields of two separate waveguides come close enough to allow transfer of energy between the two waveguides. If there is a difference in dispersion between the two waveguides, there can only be transfer of energy for a certain wavelength range where the difference in propagation constant, $\Delta\beta$ is close to zero. This is the principle for the wavelength selectivity of the coupler. The propagation constant difference is given by

$$\Delta\beta(\lambda) = \beta_1(\lambda) - \beta_2(\lambda) \tag{A.1}$$

In order to have a narrow filter the difference in dispersion of the propagation constants should be large. In order to control the wavelength for the crossing of the two dispersion relations and still have a large difference in dispersion one can add a periodic perturbation leading to the following phase matching condition

$$\Delta\beta = \beta_1 - \beta_2 - \frac{2\pi}{\kappa} \tag{A.2}$$

The center wavelength of the filter, λ_c ($\Delta\beta = 0$) is determined by the period of the grating, Λ, and the difference in effective index between the two waveguides:

$$\lambda_c = \Lambda \cdot (\overline{n_1} - \overline{n_2}) \tag{A.3}$$

If a certain center wavelength is desired, the period can be calculated by this center wavelength and the index difference. Setting $\lambda_c = 1.55\ \mu m$ gives

$$\Delta n = 0.05 \rightarrow \Lambda = 31.90 \mu m$$

$$\Delta n = 0.10 \rightarrow \Lambda = 15.95 \mu m$$

The bandwidth of the filter is determined by the total length L_{tot}, and the difference in group index $(n_{g1} - n_{g2})$ [100, 101]

$$\Delta\lambda_{1/2} = 0.8\frac{\lambda_C^2}{L_{tot}(n_{g1} - n_{g2})} \tag{A.4}$$

Therefore L_{tot} should be as long as possible if one tries to minimize the bandwidth and is not concerned with loss issues (remember that we want a bandwidth 5-10 nm (chapter 4)). The following relation holds between the total length, the coupling length, L_c, and the coupling strength, κ.

$$L_{tot} = xL_c = x\frac{\pi}{2\kappa} = N\Lambda \tag{A.5}$$

x is an integer and odd multiples of the coupling length will result in full coupling. In order to have low side peaks of the filter function x should be chosen to be as small as possible, preferable 1. Then the desired κ will be directly given by the maximal L_{tot} (L_{tot} should be slightly adjusted to fit with an integer number of grating periods). As can be seen a low κ is desired for a narrow bandwidth. The actual coupling coefficient is of course given by the index difference in the grating and the geometrical mean of the confinement of the two modes in the grating. κ is directly proportional against the index difference (for a square grating) and thus grating depth for small depths [69, p. 278].

A.1.1 Numerical calculations

The simulated structure is composed of two Ridge Waveguides laterally displaced. Since the structure must be made without regrowth, the average index difference between the waveguides is achieved by altering the average width and height in one of the waveguides by etching. A grating in one of the waveguides is performed by modulating both the height and the width of that waveguide, also by etch.

A commercial mode-solver (Selene from OlympIOs) was used to calculate the modes of the compound waveguides consisting of our laser structure presented in chapter 4 (MMLLSOA3). The index difference obtained by this method is not very large since the material of the waveguides is the same. It's even worse for the group index since the dispersion difference comes from waveguide differences alone. Thus we expect that the criteria of a filter bandwidth of 4-10 nm will be hard to meet. Calculating the best case with a very long coupler of 2 mm (meaning that we can forget about making 40 GHz lasers, which are about 1 mm) and a filter bandwidth of 10 nm (which is probably twice as wide as we want) we get from equation A.4 that $\Delta n_g > 0.096$. If we want a filter twice as narrow then we need a group index difference of 0.19. The maximum group index difference obtained from the mode-solver was less than 0.01. This explains why GAC-filters in InP usually have been of a vertical model.

Table A.1: Numerical index calculations and resulting coupled-mode theory calculations for grating-assisted co-directional coupling with the structure in Fig. A.1.

Ridge 1 (μm^2)	Ridge 2 (μm^2)	Δn_{max}	Λ (um)	Δn_g	K (cm^{-1})	BW (nm)	L_c (um)
1.6x0.1	2.2x2.1	0.016	100	-0.01	7.85	96	2000

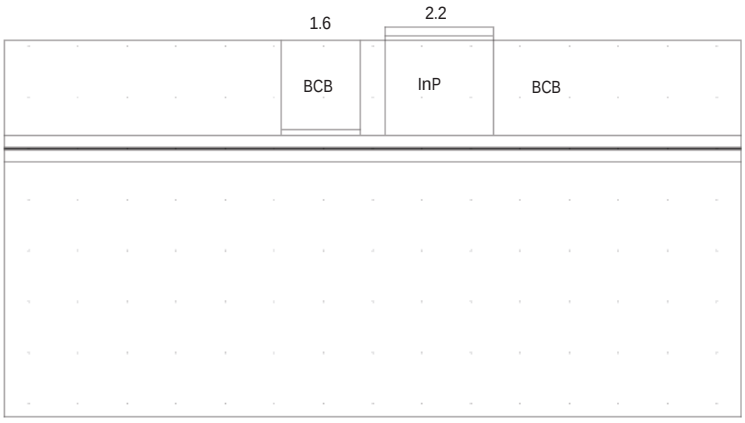

Figure A.1: The structure for a lateral GAC-filter made from InP ridge waveguide laser material.

A.2 Distributed Bragg Reflectors

A.2.1 Effective index calculations

The effective index difference between low and high index regions is the key design parameter for determining the peak reflectivity and filter width of a DBR grating, equations A.6-A.7. One common way of achieving this index difference is to grow a thin grating layer (50-100 nm) on top of the waveguide, and etch trenches in it [100]. The deeper the trenches the larger the index difference. In our case there is no grating layer, instead trenches are etched into the ridge and also in this case the trench depth decides the index difference. As figure A.3 indicates there is little index change when the etch is far from the mode (i.e. shallow etches), because of the small overlap of the mode with the index change. However, since the trenches are filled with a low-index material (BCB) there will be a large index contrast and the need for a large mode-overlap is relaxed in comparison with the grating layer approach, where a semiconductor layer has the role of index contrast. If the total peak reflectivity of the grating is small (<0.4), then the total power reflectivity from the grating can be approximated by [69]

$$|R| = 2mr\frac{\sin(\delta L_g)}{\delta L_g} \qquad ,(mr < 0.2) \tag{A.6}$$

Where m is the number of periods and r is the reflectivity from one interface (2 per period). δ is the deviation from the normalised Bragg frequency and L_g is the length of the grating. The reflectivity of each interface is directly proportional to the index difference of the interface

$$2mr = \frac{L_g}{\Lambda_k}\left(\frac{\Delta\overline{n}}{\bar{n}}\right) \tag{A.7}$$

Where Λ_k is the grating period of order k, $\Delta\overline{n}$ is the effective index difference and $\bar{n}$ is the average effective index. The period is proportional to the Bragg wavelength, λ_{DBR}

$$\Lambda_k = k\frac{\lambda_{DBR}}{2\overline{n}} \tag{A.8}$$

To calculate the effective index difference we make use of a commercially available 2D mode solving software, OlympIOs Selene. The index and mode profile is calculated using a Film Mode Matching method.

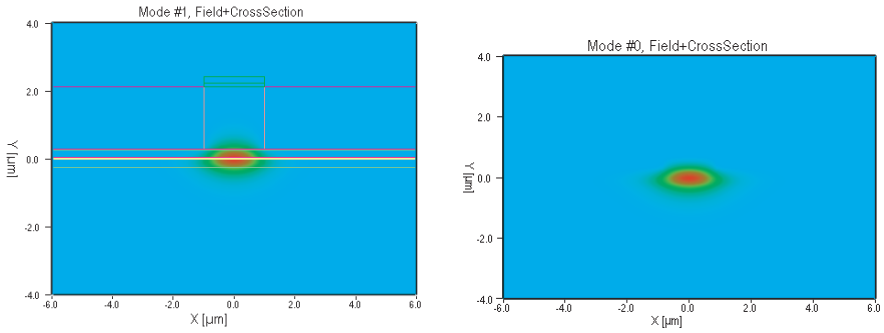

(a) Unetched (b) etched

Figure A.2: Mode fields from unetched and etched laser structures calculated with Selene.The unetched ridge has a width of 2.2 μm while the width of the etched ridge is 1.8 μm.

Since we do not know the desired etch depth yet, a range of index differences calculated with OlympIOs are put as input parameters into the Matlab program that performs the grating calculations. An approximate modulus of the reflectivity can be calculated once the index difference is calculated and can be seen in figure A.4.

The group index of the waveguide is also needed for the coming matrix calculation. It's used for calculating the effective index at wavelengths different than the Bragg wavelength. I have used the experimentally measured group index, $n_g = 3.462$ and assumed a linear dispersion. The next subsection will deal with the propagation of electromagnetic (light) waves in periodic dielectric structures, such as Distributed Bragg Reflectors (DBR).

A.2.2 Transmission matrix calculations

Reflection and transmission of lightwaves can be formalised with scattering (S) and transmission (T) matrices [69]. The S-matrix is intuitive and gives physical meaning to the matrix coefficients, while the T-matrix provides a powerful calculation tool. The first step is to calculate the transmission matrix for a single period. In our case the single period transmission matrix is a multiplication of two more basic matrices, T_{FP} and T_{trl}. T_{FP} is the transmission matrix for a Fabry-Pérot etalon with low index material, while T_{trl} is the matrix for a transmission line with high index material. Once calculated, the period matrix is multiplied with itself as many times as there are periods. The method assumes infinite planes of high and low index material and also plane light waves.

Assuming lossless interfaces, $t^2 = 1 - r^2$ and equal reflection from both interfaces, $r_1 = r_2 = r$, the FP-etalon matrix is given by [69]

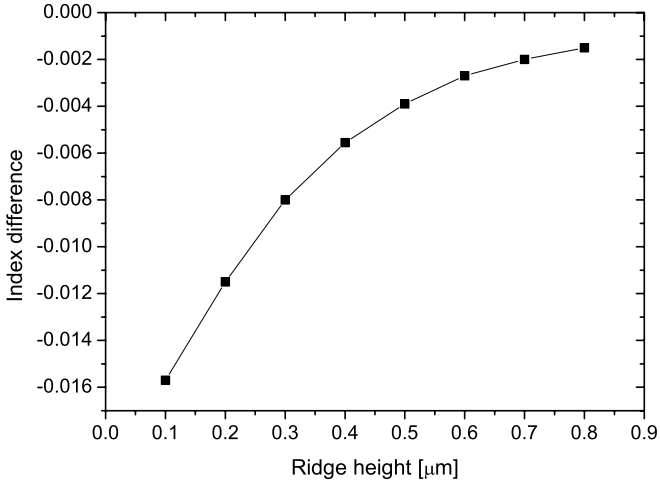

Figure A.3: Effective index difference vs. ridge height, compared to an unetched ridge for the used laser structure (MMLL-SOA3). The Effective Index method was used for the calculations.

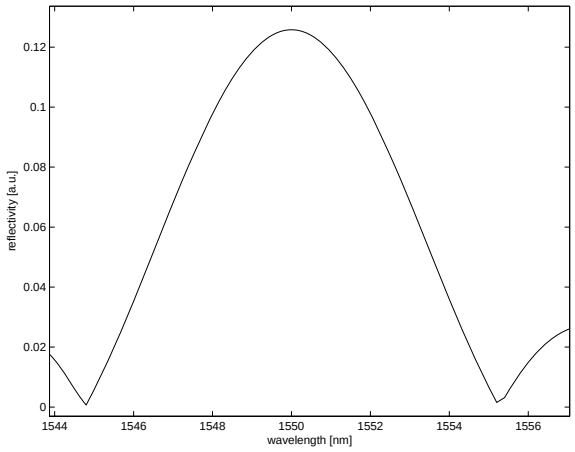

Figure A.4: Spectral response given by equation A.6. m = 100, $r = 4.2 \cdot 10^{-3}$ (Δn = 0.008), $\overline{n} = 3.19$, k=3 and centre wavelength 1550 nm.

$$T_{FP} = \frac{1}{1-r}\begin{bmatrix} e^{j\phi_1} - r^2 e^{-j\phi_1} & -(re^{-j\phi_1} - re^{j\phi_1}) \\ -(re^{j\phi_1} - re^{-j\phi_1}) & e^{-j\phi_1} - r^2 e^{j\phi_1} \end{bmatrix} \tag{A.9}$$

While the matrix for the transmission line is given by

$$T_{trl} = \begin{bmatrix} e^{j\phi_2} & 0 \\ 0 & e^{-j\phi_2} \end{bmatrix} \tag{A.10}$$

The phase is given by

$$\phi_k = b_k l = (2\pi f/c_0 \cdot n_k - i\alpha/2) \cdot l_k \qquad , k = 1, 2 \tag{A.11}$$

Where n_k is the effective index and $\alpha$is the average loss. The resulting transmission matrix for the entire grating is given by

$$M = M_1 \cdot M_2 \cdot ... \cdot M_n \tag{A.12}$$

But since all the periods are the same

$$M_1 = M_2 = M_n = T_{FP} \cdot T_{trl} \tag{A.13}$$

this can be simplified to

$$M_{tot} = M^n \tag{A.14}$$

The implementation of the multiplication is done with Matlab with the following inputs: the effective indexes n_k, the group indexes $n_{g,k}$, the order of the grating m, and the duty cycle.

The coupling factor of the grating (the strength) varies with the duty cycle and the order of the grating according to equation A.15, [100]. The function is plotted for the first 4 orders in figure A.5, and table A.2 shows the values of the duty cycle that optimises the strength for each order.

$$y = \frac{1}{k}\left|sin(\pi k \frac{\Lambda_{high}}{\Lambda})\right| \tag{A.15}$$

Where Λ_{high} is the length of the high index region and Λ_{high}/Λ is the duty cycle.

Table A.2: Optimal duty cycle and etch width as function of order of grating. Bragg wavelength is 1550 nm and effective index is 3.19

order	period (nm)	duty cycle (%)	etch width (nm)
1	243	50	121.5
2	486	25/75	121.5/364.5
3	729	17/50/83	121.5/364.5/607.5
4	972	12.5/37.5/62.5/87.5	121.5/364.5/607.5/850.5

Figure A.6 presents an example of the resulting reflection of several calculations based on first, second and third order designs. The plot illustrates the peak reflection and the FWHM width of the filters vs. the grating length. The same effective

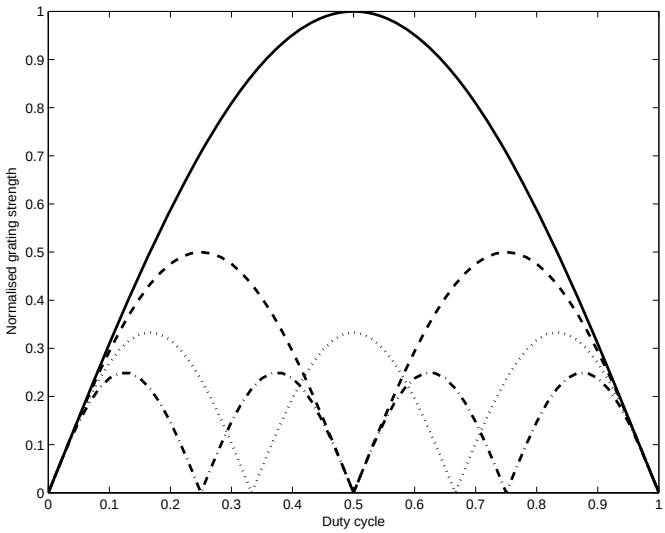

Figure A.5: Normalised grating strength vs. relative mark length (duty cycle) for the first four orders of a DBR-grating. Solid line: 1^{st} order. Dashed line: 2^{nd} order. Dotted line: 3^{rd} order. Dashed dotted line: 4^{th} order.

index difference is used for all orders, and corresponds to an etch depth of 1800 nm inside the grating and 2100 nm for the ridge. To achieve the same etch depth for all orders is however not possible with the current etch because of the increasing aspect ratio for lower orders and etch depth.

Issues The above calculations assumes a square grating. The fabricated grating was not a perfect square grating. In fact the lower, most important part, was more like a sinusoid. This can be accounted for by a lower coupling strength and will result in a lower reflection. This has not been implemented. Another issue is the loss of the grating, which is unknown. For higher order gratings energy will be coupled into radiation modes affecting the loss. Processing damage will also result in a higher loss. Another non-ideality which has not been simulated is proximity effects during the e-beam writing. The grating will be linearly chirped for the last 10 micrometers toward the two ends of the grating. The difference in etch length can more than 20 nanometers. This is not so critical when making long gratings of several hundred micrometers, but when making short, wide bandwidth gratings the proximity effect would seem to be more important. Finally the effective reflection from the grating can be affected by reflections from the facet. The effect of facet reflections has not been studied in detail during this process and has been assumed to be zero because of the AR-coating applied to the grating facet.

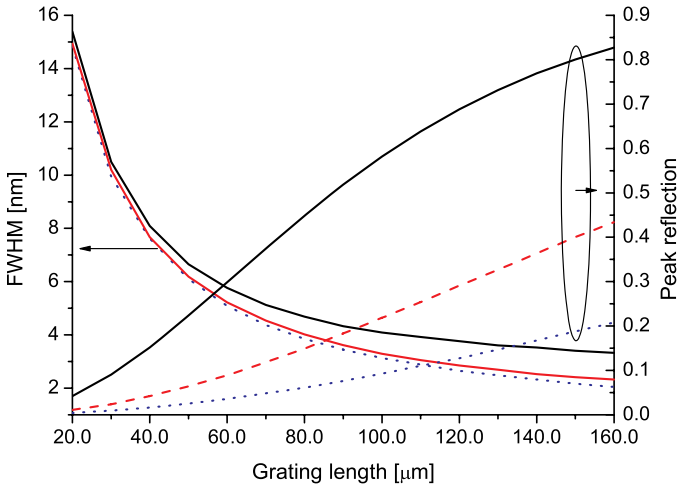

Figure A.6: Peak reflection and FWHM vs. grating length. 1st, 2nd & 3rd order. The effective index difference is 0.008 and the duty cycle of the grating is optimised for each order.

Appendix B

HDR residual phase-noise set-up details

Appendix B describes how to choose electronics for a wide-band high-dynamic range phase-noise measurement system, and how to calibrate it for accurate measurements. Calculation and measurement of the noise floor is also described in detail.

B.1 Microwave equipment

Figure B.1 is a schematic over the entire set-up for measuring the phase-noise (timing jitter) with high dynamic range of a ∼40-GHz synthesizer-driven (mode-locked) laser. The upper branch represents the optical part, while the lower branch represents the electrical reference part. The electronics in the upper branch should be as wide-band as possible around the mode-locking frequency (40 GHz in this case) to include the whole phase-noise spectrum of the laser. The mixer must be broadband on both input and output and the following electronics must also be broadband (DC and upward).

Table B.1: Electrical specifications of the used electrical components for the set-up. PD is PhotoDiode and LNA is Low Noise Amplifier. NF, noise figure, and G, gain.

Device	f-range, 3dB (GHz)	NF (dB)	G (dB)	Sat. power (dBm)
U2t PD	DC-50	-	-	-5 (output)
LNA1	33-50	5	24	18 (output)
Mixer	33-50, 0-17	7	-7-(-8)	13 (input), 5 (output)
Bias-T	0.000005-15	0.5	-0.5	33
LNA2	0.00003-15	6	26.6	23.5 (output)

Low-noise amplifiers should of course have a low noise figure (NF) and a large gain to achieve highest possible dynamic range (shot noise limited). As we will see later (equation B.11) the NF and gain of the first amplifier are the most important

to achieve a low NF for the entire system. The mixer and the components preceding it should have high saturation powers, since the shot noise limited dynamic range increases with 10dB/dec average photocurrent.

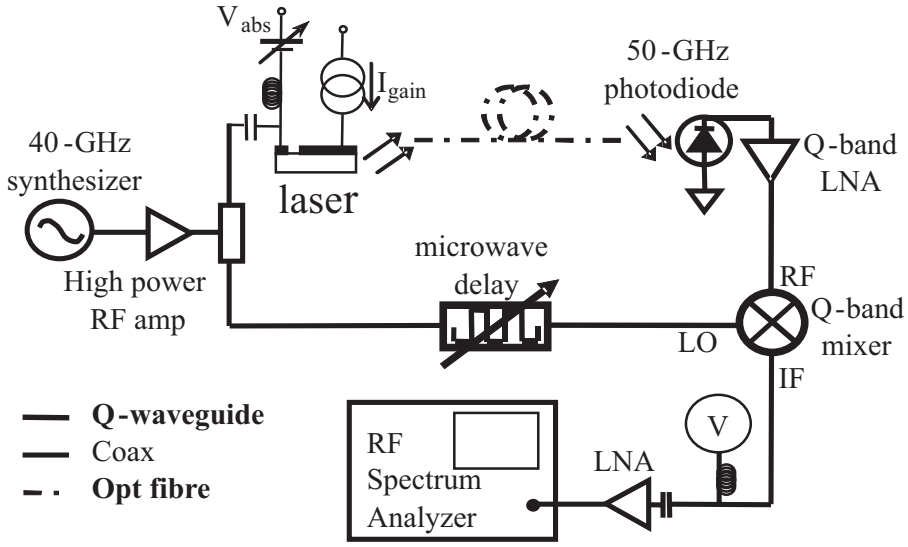

Figure B.1: Schematic of residual measurement set-up. V_{abs}, absorber DC voltage; I_{gain}, gain current; RF, radio frequency (signal); LO, local oscillator; IF, intermediate frequency; V, voltage meter.

B.2 Calibration

The calibration of a measurement system, whatever it might be, is probably always the most important step toward reliable data. In this case the calibration is especially delicate since we are measuring a signal that has been converted from the optical domain to the electrical, amplified, frequency shifted and attenuated and amplified again. Although specified to work over large bandwidth, most of the electronics are frequency dependent, and need to be calibrated out. Furthermore the mixer output depends on the Local Oscillator power, and finally photodetector, amplifiers and mixer can all be saturated with too high input signals. These uncertainties can be overcome by injecting a known narrowband signal, E_{cal}, into the system while measuring the output power for a given input power, for a certain LO-power. The LO-frequency is fixed, f_{LO}, while the offset of the signal from the LO-frequency is varied, $f_{\mathrm{LO}} \pm f$. The two signals will beat and the baseband signal from the output of the mixer, v_{IF} can be logged vs. the offset frequency, f:

$$v_{IF}(t) = \frac{\alpha}{2} V_{LO} V_{RF} \sin(2\pi f t) \tag{B.1}$$

The peak value measured is a direct measure of the so-called phase detector constant, $K_{\phi[BEAT]} = \alpha V_{LO} V_{RF}$.

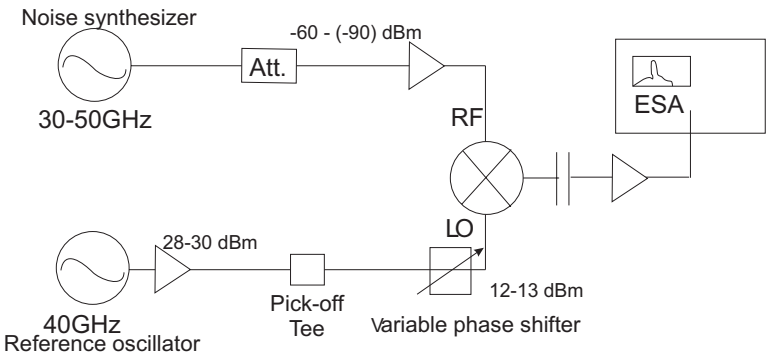

Figure B.2: Calibration set-up. Att.: attenuator, RF: radio frequency, LO: local oscillator, ESA: Electrical Spectrum Analyzer. The pick-off tee is included in the calibration set-up to make the calibration situation similar to the measurement set-up for the laser noise (figure B.1).

Since our system include a photodiode and a couple of amplifiers too, we prefer to speak of the total system transfer function, H_{system}, including the response of the spectrum analyzer, R_{ESA} (all spectrum analyzer errors should thus cancel when we subtract the transfer function), equation B.2. This method is described in [43] as the Beat Note Method. The relation between the input signal, S_{in} and the measured spectrum, S_{out} will then be

$$S_{out}(\omega) = S_{in}(\omega)(H_{phasedetector}(\omega) \cdot R_{ESA}(\omega)) = S_{in}(\omega) \cdot H_{system}(\omega) \qquad \text{(B.2)}$$

Before the calibration of the measurement system itself, the frequency dependence of the output power from the noise signal source (Agilent 83650A, 10MHz-50GHz) is measured with a calibrated HP microwave power meter, (figure B.3), such that it can be calibrated for.

In the next step the power to the LO-port of the mixer is logged vs. the power setting of the LO-synthesizer, figure B.4 (The working linear range of the mixer is 10-13 dBm of LO-power.). It is important that a subsequent noise measurement is compared with a calibration done with the same LO-power, since V_{LO} is included in the system response.

The signal source is then fed into the amplifier preceding the mixer and the entire response from the system is then logged from the ESA. This is repeated for offset frequencies ranging from 10 kHz to 10 GHz.

B.3 Calculating and measuring the noise-floor

If we assume that the path difference between the two arms is exactly zero, then the theoretical electrical noise floor is given by the sum of shot-noise in the photodiode and thermal noise from the electronics. The following section will be a short exercise in calculating this noise floor. The shot noise current, equation B.3, is proportional to the square root of the average photo current, which in turn is proportional to the average optical power, $i_0 = R \cdot P_0$ [43]. Calculating the dynamic range (DR), equation B.5, indicates an increase in DR with 10dB/dec average photocurrent.

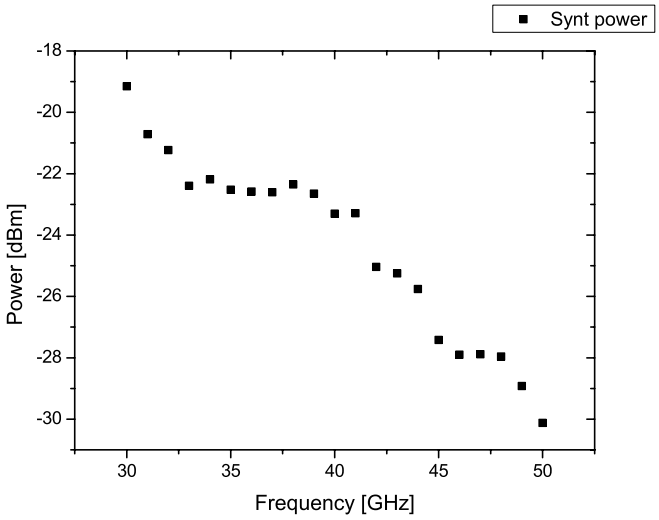

Figure B.3: Power from "noise" synthesizer, Agilent 83650A, as a function of frequency setting for a constant power setting.

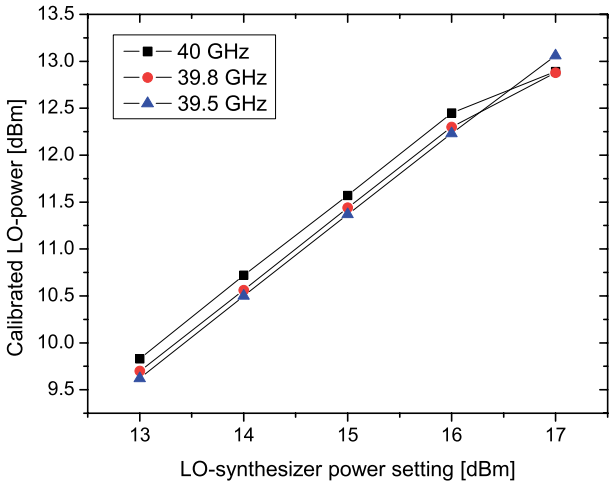

Figure B.4: LO-power vs. synthesizer power after 1 m Utiflex cable.

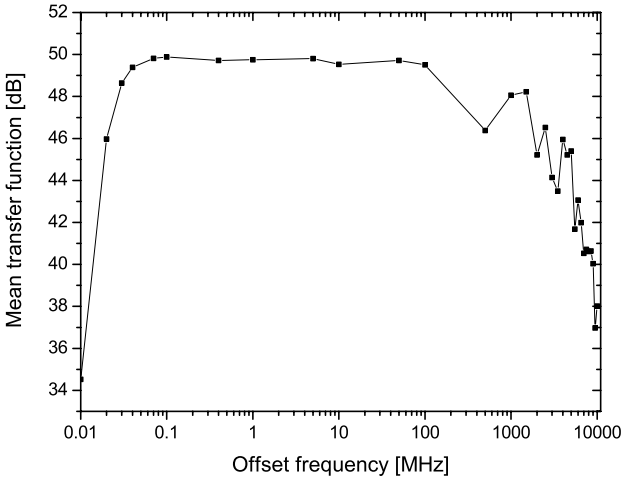

Figure B.5: Total system transfer function.

The thermal noise on the other hand is proportional to the temperature, equation B.7. All resistive elements in an electric circuit generate thermal noise. This phenomenon was first described by Johnson [102] and Nyquist [103] in 1928, but the derivation of the thermal noise power can be found in modern text books on electronics, such as [104]. At room-temperature this thermal noise power per bandwidth is -174dBm/Hz. To easily compare electrical devices, engineers use the term noise figure (NF), which tells us how many dB above the thermal noise a certain device is, equation B.10.

The shot noise, δi_{shot} and the shot noise power, $(di_{shot})^2 R$ are given by

$$\delta i_{shot} = \sqrt{2qi_o B} \tag{B.3}$$

$$(di_{shot})^2 R = 2qi_0 BR \tag{B.4}$$

and the dynamic range (DR) of signal to shot-noise power is

$$DR = (\frac{i_0}{\sqrt{2qi_0 B}})^2 = \frac{i_0}{2qB} \tag{B.5}$$

Normalised to 1 Hz and in dB the DR is

$$DR(dB) = 155 + 10log[i_0(mA)] \tag{B.6}$$

Typical values for our u2t-photodetector for a photocurrent of $i_0 = 2mA$ are an electrical carrier power, $P_c = -12dBm$ and a shot noise $P_{shot} = -12dBm - DR = -12dBm - (155 + 3)dB = -170dBm/Hz$

The total thermal mean square noise current, $\overline{i^2_{N,th}(v)}$ and noise power, P_N are given by

$$\overline{i^2_{N,th}(v)} = \frac{4hv\Delta v}{R(e^{hv/kT} - 1)} \cong \frac{4kT\Delta v}{R} \tag{B.7}$$

$$P_N = kTB \tag{B.8}$$

The thermal noise per bandwidth and the Noise Figure is

$$kT = -174dBm/Hz \qquad , T = 300K \tag{B.9}$$

$$NF = 10log[P_{N,actual}/kTB] \tag{B.10}$$

Table B.2: Noise figure and electrical gain for the components in the residual phase-noise set-up

Component	NF (dB)	Gain (dB)
LNA1	5	24
Mixer	7	-7
LNA2	5.75-6.5	25

The system noise figure is given by

$$F_{syst} = F_1 + \frac{F_1 F_2}{G_1} + ... + \frac{F_1 F_2 ... F_n}{G_1 G_2 ... G_{n-1}} \tag{B.11}$$

where F_1 is the noise figure of the first component in the electrical system and G_1 is it's gain. $F_n$is the noise figure of the last component (the ESA in this case). The noise figure of this particular system, calculated from the values in table B.2, is dominated by the first amplifier's NF (because of its large gain) and is calculated with equation B.11 to be 5.1 dB for the components in our set-up.

The total noise floor power is obtained by adding all the noise powers

$$P_{N,\,tot} = P_{shot} + P_{thermal} \tag{B.12}$$

In numbers we get -170 dBm/Hz+ (-174dBm/Hz+5.1dB) dBm/Hz = - 166.4 dBm/Hz. Or relative to the carrier and single-sided: -166.4dBm/Hz- (-12dBm)-3dB = -157.4 dBc/Hz.

Measuring the noise floor is done by replacing the laser probe, the laser carrier waveguide, the laser itself, the fibre and the photodetector by an equivalent microwave attenuator (in this case SHF 60 GHz, 40 dB). Fig. B.6 displays the measured noise floor with our best synthesizer (Agilent PSG 8247E). Since the synthesizer noise is not completely cancelled the noise floor is much above the calculated floor for frequencies slower than 2 GHz. Above this frequency the noise floor is set by the shot noise and thermal noise. If one would want to increase the dynamic range of the measurement, one can increase the mean power to the photodiode as long as the photodiode and the following electronics do not saturate. With the current electronics we are limited by the saturation of the mixer (+13dBm input power). The thermal noise could also be lowered by cooling of the electronics, but gaining 3 dB corresponds to working at 150 K, which might complicate things. An alternative could be to buy electronics with lower noise figures.

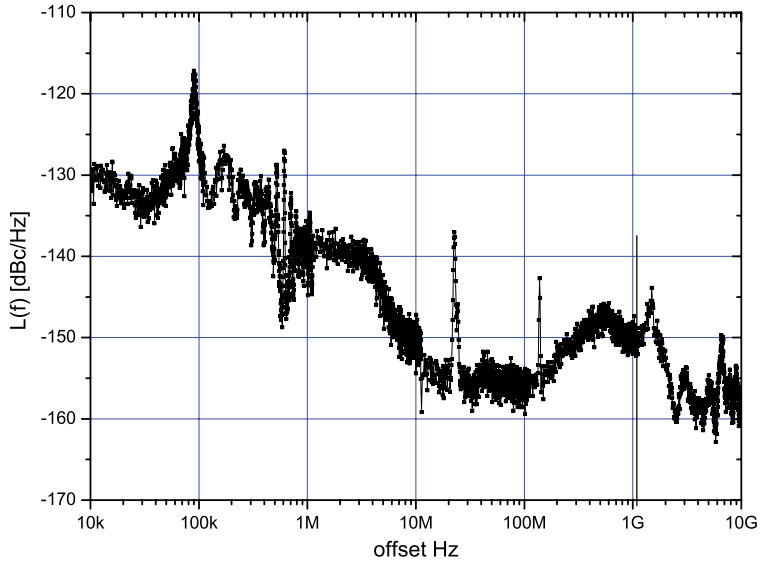

Figure B.6: Measured noise floor with Agilent PSG 8247E synthesizer in both RF- and LO-ports.

Appendix C

Fabrication process

The following is a step-by-step processing flow for the fabrication of ridge-waveguide monolithic mode-locked lasers with integrated deeply etched surface gratings.

C.1 SiO_2-deposition by PECVD for ridge and grating mask

SiO_2 is used as a masking material for the MORIE (InP dry etch) because it has a low etch rate in the InP-etch ($\leq$1 nm/min for our etch), because it is easy to pattern with a CHF_3-plasma and it is easy to remove the mask afterwards in BHF without affecting the semiconductor. Other masking materials suitable for MORIE is SiN_x [86], metals like Ti, Ni and Cr [53] and different combinations of SiO_2 with metals [82].

The SiO_2 is deposited with an STS (Semiconductor Technology Systems) Plasma Enhanced Chemical Vapour Deposition (PECVD) system at a rate of 58 nm/min. The choice of thickness for the deposited SiO_2 is a trade-off between greater etch depth in the InP and increased thickness of the resist used as a mask for the etching of SiO_2. Using a thicker UV-resist than the 600 nm used for the 2 μm ridge lithography is tolerable within this study, but grating definition with 120-360 nm patterns will not tolerate too high aspect ratios, and problems with charging can occur during e-beam writing. The electron beam resist will be treated in more detail in the next section and we will just conclude here that there is a limit for the maximum thickness of the e-beam resist, and that this means that it controls the maximum thickness of the SiO_2.

C.2 E-beam resist and its exposure

We use ZEP-520A (ZEONREX Electronic Chemicals), a positive tone e-beam resist. It is known for its high resolution, high stability and relatively good dry etch resistance. Technical information can be found in [105]. Resist thickness can be varied by varying the dilution of the resist in a solvent and by changing the spin speed and/or acceleration. E.g. with ZEP diluted to 11% in Anisole, an acceleration of 1000 rpm/s and a steady state spin speed of 2000 rpm will produce a resist layer 520-550 nm thick, while an acceleration of 4000 rpm/s and a steady state

spin speed of 6000 rpm will produce a resist layer 310 nm thick. After spinning the resist is pre-baked at 160 °C for 2 min.

The e-beam pattern is designed in L-edit, a graphical layout editor. The width of the grating is much wider than the ridge (40 my) in order to achieve sharp corners.

The wafers with e-beam resist are exposed in a JEOL-JBX9300FS with 100kV electrons (resolution better than 10 nm). The dose necessary to develop the resist mostly depends on the substrate and how densely separate lines are spaced (the actual pattern). I have used a dose of 220 μC. After exposure the resist is developed in ZED-N50 for 1 min 10 sec, stopped and rinsed in IPA, followed by a blow dry in nitrogen. The samples are post-baked at 110 °C for 2 min on a hotplate.

C.3 SiO_2-etching 1, CHF_3/O_2 RIE

This etch transfers the grating from the e-beam resist to the glass mask. The process development was described in section 4.2.2. The glass mask is etched at a pressure of 100 mT, a flow of 16 sccm CHF_3 and 2 sccm O_2, and a power of 60 W (and a temperature of 20 °C). This results in a bias of 320 V and an etch rate of approximately 27 nm/min in glass. The etch rate in the resist is a little higher but almost the same, while the etch rate of the underlying semiconductor is ten times smaller (2.5 nm/min for InP). The etch rate of the semiconductor is relevant since a certain amount of over etch is necessary because of microloading. The over etch was 3-4 min. After the grating etch, the electron beam resist is removed with a liquid resist stripper (Shipley Microposit Remover 1165) at 60 °C followed by a final removal in a plasma asher (Oxygen plasma) at 0.2 mbar and 100 W for 5 min.

C.4 UV-resist

Before applying the UV-resist the surface is prepared for better adhesion. This is done by baking the wafer at 150 °C and immersing it in HMDS vapour afterwards. AZ5206 (AZ5214 with thinner) is spun to a thickness of about 600 nm and is pre baked at 90 °C for 90 s. The resist is exposed through a quartz mask containing the ridge pattern for 5s and developed for 1 min in AZ351B:H_2O (1:5),. After development the resist is post baked at 90 °C to smooth the surface and this is followed by a short ash to remove any residues of resist in the developed areas. The width of the ridge is about 2.2 μm after the ashing.

C.5 SiO_2-etching 2, CHF_3/O_2 RIE

The ridge pattern is transferred from the UV-resist to the glass mask through a second glass RIE. The grating is protected only under the ridge and the rest of it disappears in this etch. However, since the open areas in the grating are heavily over etched because of this second etch, there will be a small and unwanted pattern transfer from the grating mask to the underlying semiconductor. After the etch, the resist is removed and the wafer is cleaned at the same time in acetone, ethanol and DI-water.

C.6 InP-etching, cyclic CH_4/H_2 and O_2

Before the MORIE, the chamber is primed with a precondition program running for 12 min. The ridge and ridge grating are etched simultaneously with the MORIE described in subsection 4.2.3. First the contact layers are etched and the depth is measured with a stylus profilometer (Dektak). The remaining etch time in the InP is estimated from calibration runs on pure InP-wafers. The etch is stopped right at the interface between the InP and the Q-material waveguide. Because of loading effects the etch depth will be approximately 100 nm less at the ridge than the measured depth with the dektak, which measures several microns away. Since the optical mode is mostly located under the ridge, the depth at the ridge is more important than a few microns away. After the dry etch, the surface is given a wet chemical treatment in order to remove damaged material. The wafer is dipped in concentrated H_2SO_4 for 1 min to remove approximately 15 nm of possibly damaged surface material.

C.7 Contact separation

After the ridge and grating etch, the wafers are prepared for the contact separation lithography by cleaning and adhesion promotion (baking and HMDS). UV-resist AZ5214 is spun to a thickness of 2 μm. The resist is exposed and developed to form 5 μm openings on the ridge, revealing the glass. The glass ($\sim$100 nm) is dry etched until it's all gone. After the glass etch, the contact layers are wet etched in a mixture of 10% H_2SO_4 and H_2O_2 (1:1). After 60 s the etch depth is $>$200 nm which is enough for a couple of kohms resistance. After the etch the resist is stripped and the wafers are cleaned.

C.8 BCB

Benzocyclobutene (BCB, Cyclotene 30 22-32 is the trademark) is a polymer which is very suitable for planarisation of the ridges (it also passivates and lowers the capacitance). First, 25 nm of glass is deposited to increase the adhesion of the BCB. An adhesion promoter (AP3000) is spun on the glass before the BCB is spun to a thickness of $\sim$2 μm, covering the wafer up to the level of the ridge top. The BCB is cured at 250 °C for 5 hours and the ridges are revealed after a mask less dry etch of the BCB. The dry etch contains oxygen and also a small amount of freon to etch the silicon in the BCB.

C.9 Metal lift-off for top metals

An adhesion promoter, AP3000, for the metals is first spun on the wafer. Then the wafer is spin coated with a bilayer of photoresists: 900 nm of LOR7B (prebaked for 5 min at 170 °C) and 600 nm AZ5206E (prebaked for 90 s at 90 °C). Exposure of the resist is done for 10 s at 5 mW/cm^2. The top resist is developed in AZ351B:H_2O (1:5) for 60s and post-baked for 2 min at 120 °C. Then the lower layer (LOR7B) develops isotropically in the resist developer (AZ351B) for 5 min, thereby giving undercut profiles, well-suited for lift-off.

The glass on the ridge is removed in a wet etch before the evaporation of the p-contact metals: Ti:500Å/Pt750Å/Au:5000Å. The pattern is transfered by lift-off.

C.10 Thinning

The wafers are bonded to a thick glass substrate with wax. The glass substrate with the wafer is then put into a thinning machine with Al_2O_3-particles and thinned down to a thickness of ∼110 nm.

C.11 Back metal

N-contact metal (Ni 80nm, Ge 100nm, Au 250nm) is evaporated and annealed at 420 °C for 5 s. Die soldering metal (Ti 50nm, Pt 75nm, Au 500nm) is the last process step that is performed in the cleanroom environment.